UNIVERSITY OF TRENTO

DEPARTMENT OF INFORMATION ENGINEERING AND COMPUTER SCIENCE
DEPARTMENT OF INDUSTRIAL ENGINEERING
FONDAZIONE BRUNO KESSLER
Doctorate Program in Industrial Innovation

Why ULM has not yet been integrated in clinical practice?

Giulia Tuccio

Advisors
Prof. Libertario Demi
University of Trento

Wim Van Hoeve
Solstice Pharmaceuticals

November 2025

Abstract

Ultrasound Localization Microscopy (ULM) has emerged as a promising ultrasound-based technique to characterize microvascular structures, due to its ability to overcome the ultrasound diffraction limit. The enhanced resolution capability is a consequence of precise localizations of microbubbles (MBs) injected in the circulatory system. These localizations can be used to track MBs over time to obtain not only geometrical, but also dynamic information of microvascular flow. ULM combines its ability to achieve a micrometric resolution with the advantages of ultrasound (i.e. low-cost, non-ionizing, portability). Thus, the technique might represent an indispensable clinical tool for understanding various diseases, such as cancer and stroke, which are known to be associated with changes in vascular structures. However, ULM clinical translation is hindered by various requirements, including high frame rates (FR), low MB concentrations, leading to prolonged acquisition times, and lack of validation methods. This thesis addresses these challenges by showing how to reduce the FRs of a factor 10 and reduce the acquisition times to 1/4 while maintaining similarity with original ULM-generated images. Furthermore, the thesis addresses the constraint of low concentrations by introducing a bi-disperse MB population. The uncoupling of this population, characterized by a couple of monodisperse MBs populations, allows to increase MB concentrations, and, potentially decreasing the acquisition times. Finally, we demonstrate the feasibility of 3D printing vascular phantoms for ULM image generation. With the goal of bridging the gap between various critical ULM trade-offs and clinical practice, this research is presented.

Keywords
Ultrasound Localization Microscopy, Ultrasound Contrast Agents, Monodisperse Microbubbles, Radial Basis Function Interpolators, Fundamental and Harmonic Imaging, Fast Fourier Transform, Point Spread Function, Orthogonal Frequency Division Multiplexing, Vascular Phantom, 3D printing

Acknowledgments

This thesis could not have been completed without expressing my gratitude to all who contributed and supported me during my PhD. First and foremost, I would like to thank my supervisor, Dr. Libertario Demi, who constantly guided and advised me throughout my doctoral studies, helping me grow not only professionally but also personally. Libertario's mentorship and perspective on research have been truly inspiring.

My deepest thanks go to my ULTRa journey companions: Sajjad Afraktheh, Luca Giaccone, Federico Mento, Hamed Jalilian, Mattia Pererpenti, Han Xi, and Chiara Zangrandi. The time spent together in the lab was filled with stimulating conversations, laughter, and joy, which helped me navigate the emotional rollercoaster of the PhD.

I would also like to thank Wim Van Hoeve, my supervisor at Solstice Pharmaceuticals in Enschede, the Netherlands, for his support during my research journey. I extend my gratitude to all collaborators at Solstice; my time in the Netherlands was invaluable in learning how to apply research in an industrial context.

A heartfelt thanks to Tommaso Di Ianni and the members of his lab—Valeria, Andrea, and Edi—who introduced me to the world of neuroimaging and in vivo data acquisition. My time at UCSF was enriched by your guidance, cheer, and the wonderful memories we created together. I would also like to thank all other collaborators who supported my research, including Ciro Malacarne and Matteo Perini from Prom (Rovereto), Fabio Barlocco (Director of Cardiology, Busto Arsizio-Gallarate), and Stefania Marconi and Valeria Mauri (ProtoLab, University of Pavia).

This acknowledgment would not be complete without thanking my friends, with whom I rediscovered my love for Trento and the mountains: Elia, Alessandro, Alberto, Margherita, Charlotte, and Yasaman. A special thanks to Alessandro, who supported me, listened to my endless stories, pushed me to keep improving, and even flew to San Francisco to be by my side.

Finally, I want to express my deepest gratitude to my family. To my grandparents, Carlo and Elda, who, despite often asking "How's school going?" and complaining about my absence, always supported me. To my parents, Barbara and Stefano, and my sister, Federica: without you, none of this would have been possible. You have been an endless source of love, guidance, and encouragement since my childhood, providing everything I needed for my mind and heart. I cannot thank you enough.

Contents

List of Tables

List of Figures

List of Abbreviations

ULM	Ultrasound Localization Microscopy
MB	Microbubble
FR	Frame rate
MRI	Magnetic Resonance Imaging
CT	Computed Tomography
US	Ultrasound
2D	Two-dimensional
3D	Three-dimensional
RF	Radiofrequency
MRA	Magnetic Resonance Angiography
CTA	Computed Tomography Angiography
PW	Power Doppler
CEUS	Contrast Enhanced Ultrasound
MIP	Maximum Intensity Persistence
FWHM	Full Width Half Maximum
MHz	Mega Hertz
UCA	Ultrasound Contrast Agents
PSF	Point Spread function
TIC	Time Intensity curve
ROI	Region of Interest
TEULM	Time Efficient Ultrasound Localization Microscopy
FRC	Fourier Ring Correlation
OFDM	Orthogonal Frequency Division Multiplexing
SR	Super-resolution
DAS	Delay and Sum
SVD	Singular Value Decomposition
IP	Interpolation
RMSE	Root Mean Squared Error
NLM	Non Local Mean Filtering
MQ	Multi Quadratic

List of Symbols

f	Center frequency
λ	Wavelength
c	Speed of sound
DS	Downsampling
ϕ	Multiquadratic RBF function
β	Interpolation Coefficient
r	Radius of RBF function
σ	Standard Deviation
res	Resolution
F_{rec}	Reconstructed Function
CR	Compression ratio
N_{pix}	Number of pixels
I_{DS}	Down-sampled image
I_1	Original ULM-generated image
CR	Compression Ratio
$DICE$	Dice score
UpS	Upsampling factor
2x2D RBF	Bi-directional 2D Radial Basis Function
T_x	Acquisition Time
TP	True Positive
FP	False Positive
FN	False Negatives
IP	Interpolation
I_{pix}	Pixel Intensity maps
ncc	Normalized Cross Correlation maps
$p_{5.5MHz}$	5.5 MHz MB population
$h_{5.5MHz}$	5.5 MHz MB population image
p_{3MHz}	3 MHz MB population
h_{3MHz}	3 MHz MB population image
h_1	First harmonic image
h_2	Second harmonic image

Chapter 1

Introduction

This chapter aims at walking the reader through the anatomy of the circulatory system and the commonly used clinical imaging modalities to visualize and characterize the vasculature. In addition, the standard Ultrasound Localization Microscopy (ULM) processing pipeline together with advanced ULM state-of-the-art methods are introduced. The shortcomings that delay clinical translation lead to the identification of several research problems. Finally, this introductory part discusses the novel contributions of the thesis in light of the pinpointed challenges.

1.1 Cardiovascular System

The cardiovascular system delivers hormones, nutrients and oxygen throughout the body and removes waste products and excessive heat. As shown in the schematic in figure 1.1, the cardiovascular system is composed by the heart, acting as a pump, and an intricate network of vessels in which the blood flows. Blood vessels include arteries, capillaries and veins. Arteries carry the blood from the heart to the organs and are divided into big and small depending on their diameter. Small arteries further branch into capillaries, which can reach down to 10 μm of diameter [1]. The thin wall at the capillary level allows the exchange of nutrients, gases, and waste between tissues and organs. Veins begin from capillaries and increase in diameter as they converge towards the heart [2, 3].

1.1.1 Vascular variations as pathological biomarker

To introduce the potential benefits of ULM clinical application, we present some pathologies and their correlation with vascular alterations. It is well known that variations of the circulatory system are a marker of a broad set of diseases. These (micro-)vascular alterations can be diverse, and include modifications such as angiogenesis and reduction of microvascular flow.

During angiogenesis, new vessels are formed. Since these vessels are more tortuous and have fewer branchings compared to normal vasculature [4], they could be used to detect an active angiogenic process. Angiogenesis may occur in malignant tumors [5], as well as in other inflammatory processes such as rheumatoid arthritis [6] and atherosclerosis [7]. Being able to detect and monitor microvascular alterations would provide a powerful tool

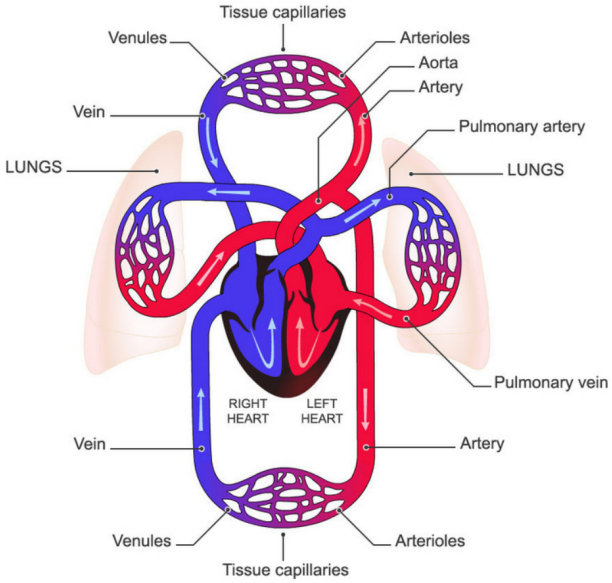

Figure 1.1: Schematic image of the cardiovascular system. Arteries and veins are color-coded by red and blue respectively.

to guide early diagnosis and tempestive clinical treatment [5, 8].
Angiogenesis is also observed in healing processes. For instance, differences in blood volume, flow velocities, and tortuosity are observed after acute spinal cord injuries [9]. Therefore, the characterization of vascular alterations could help to understand the severity of lesions and to predict the prognosis of treatment.
Another disease correlated to alterations of the vasculature is chronic kidney disease, which is associated with a dysfunction of the vasculature and reduction of capillary density [10]. In particular, in the transition from acute to chronic, changes in the vasculature might play an important role.
Pathologies of small vessels are also related to diabetes [11] and neurodegenerative diseases such as Parkinson's and Alzheimer's [12, 13]. In these pathologies, an increased tortuosity in the brain and decreased blood volume is observed.

The clinical benefit to characterize the microvasculature and its variations could be critical. Here, we described some correlations between diseases and vascular alterations. However, the number of these pathologies and the extent to which we understand microvascular alterations is limited by commonly used imaging modalities. A thorough understanding of the microvascular structures and their alterations would be groundbreaking if applied to the clinical context. Nevertheless, microvascular imaging is limited to bigger vessels due to a lack of imaging methods having microscopic resolution, low cost, and non-toxicity for patients [8, 14].

Table 1.1: Comparison of various vascular imaging modalities. To better compare the modalities, the diameter of the smaller vascular structures can reach down to 10 μm.

Modality	**Source**	**Resolution**	**Depth**
MRI	Radio Wave	1 mm	no limit
CT	X-Ray	50-200 μm	no limit
Optical Imaging	Light	0.3 μm	<1.5 cm
US	Ultrasonic wave	200-500 μm	<15 cm

1.2 Vascular Medical Imaging

There are various methods to visualize the vasculature which are currently applied in the clinical context. These include Magnetic Resonance Imaging (MRI), Computed Tomography (CT), Optics, and Ultrasound (US). These imaging modalities are compared based on the source allowing the imaging, the resolution (i.e. the smallest spatial distance for which two scatterers can be distinguished in the image) and tissue penetration depth. A summary of the different vascular imaging modalities is displayed in Table 1.1.

1.2.1 Magnetic Resonance Imaging

Magnetic Resonance Imaging (MRI) generates 2D and 3D images of inner body structures, including arteries and veins. MRI deploys a magnetic field and radio waves to image different body tissues. At first, the hydrogen ions, positively charged, are excited by the magnet embedded in MRI, which causes them to align along the direction of the magnetic field. Then, a radiofrequency (RF) pulse is used to disturb the alignments of the magnetically active nuclei, which start spinning in-phase along the perpendicular direction of the magnetic field. Once the RF pulse ends, the hydrogen nuclei would spin out of phase and realign with the direction of the magnetic field. The differences happening in different body tissues during RF pulse sequences are measured, producing the MRI image [15]. A specific type of MRI to visualize the vasculature is MRI Angiography (MRA). In MRA, repetitive RF pulses saturate the stationary structures (e.g. tissues and background), allowing to visualize non-stationary structures (e.g. blood) [16]. An example of 3D MRA cerebral vasculature is shown in figure 1.2. Based on the power of the magnetic field, MRI can reach a spatial resolution of 10-100 μm. However, the approved magnetic field strength allows for a resolution of only 1 mm for humans [17]. MRA can work with or without contrast agents, is non-invasive and does not require ionizing radiation. However, as for MRI, the resolution is limited to few millimeters, it is expensive and time consuming technique.

1.2.2 Computed Tomography

Computed Tomography (CT) is a 3D medical imaging modality that uses X-ray beams for the visualization of organs and tissues. In CT, X-rays at different angles are used to measure energy-mass attenuation and energy-mass absorption to differentiate and image tissues [17, 19]. In Computed Tomography Angiography (CTA), high-resolution images

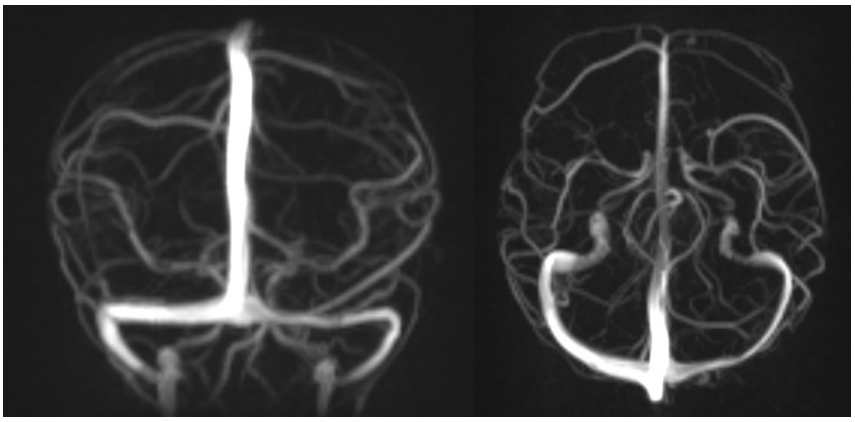

Figure 1.2: MRA coronal and axial 3D reconstruction of cerebral venous system, figure from [18].

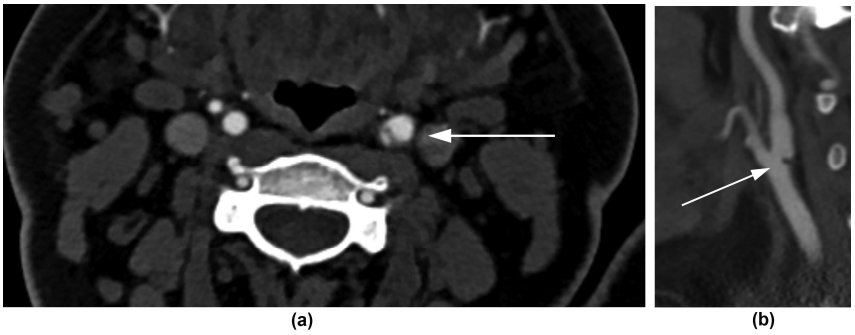

Figure 1.3: CTA of a thrombic carothid bulbs, axial (a) and sagittal (b) images (Image from [20]). The white arrow indicate the thrombotic bulb extending from the outer wall into the lumen.

of the vasculature are created using electron-dense contrast agents. Despite the high resolution of the CTA images (50 μm), CT X-ray exposure could be harmful, which avoids this technique from being employed for frequent exams. An example of CTA of a carotid thrombus is shown in figure 1.3, from [20].

1.2.3 Optical Imaging

In optical imaging, light properties are combined to obtain detailed images of tissues and microvascular structures. Vascular optical methods can be divided into two main subgroups: ballistic (e.g. single and two-photon fluorescence microscopy) and diffusive imaging (e.g. diffuse optical tomography). The first category provides better resolution, but low penetration depth (0.5 - 1.5 mm), whereas the second provides few centimeters as imaging depth but poorer resolution. Optical imaging has attracted interest due to being non-invasive and highly sensitive, providing a resolution down to nanometer scale [21]. The major limitation is small penetration depth ($<$ 1 mm) [17]. An example of one-photon fluorescence microscopy is shown in figure 1.4.

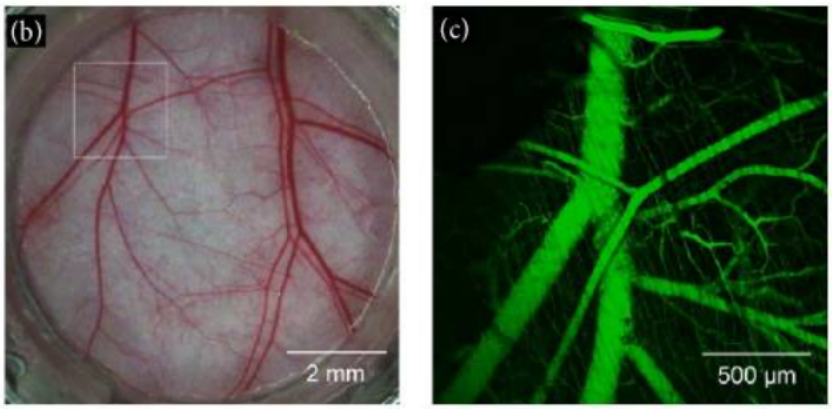

Figure 1.4: Images of the vasculature with white light image photograph (a) and single-photon fluorescence microscopy (b). Figure from [22].

1.2.4 Ultrasound

In Ultrasound (US) medical imaging, the backscattered echos produced at the interface between different media (e.g., between blood and muscle) insonified by the ultrasonic wave are combined to generate anatomical images of subcutaneous structures, such as organs and muscles [23, 24]. US can be used to visualize the vasculature with or without injecting contrast agents. Contrast agents enhances the back-scattered signal when insonified with the US wave. The benefits of US include high temporal and spatial resolution, compatible with real-time applications, low cost and non-toxicity. However, US is limited by low penetration depth (bigger than optical imaging), operator-dependent results, and diffraction-limited resolution, impeding its applicability for micro-vasculature imaging [24]. Vascular US methods are in depth discussed in the next section.

1.3 Ultrasound Medical Imaging

Ultrasound is one of the most popular medical imaging modalities and is used to image a broad variety of organs in diverse applications (e.g. gynecology, oncology, vascular imaging, etc.). The principle of ultrasound imaging, and ultrasound techniques to visualize the vasculature (Power Doppler, Color Doppler, Contrast Enhanced Ultrasound) and the microvasculature (Ultrasound Localization Microscopy) are discussed.

1.3.1 Introduction

In medical US, ultrasound waves generated by a transducer propagate in the body, generating backscattered waves at the edge between different tissues. These backscattered signals are combined to generate images of tissues, organs, and blood flow. The spatial resolution can be either perpendicular (lateral) or along (axial) the direction of propagation of the US wave. While lateral resolution depends on US beam shape and worsen with depth, axial resolution does not. The axial resolution depends on pulse length, which in

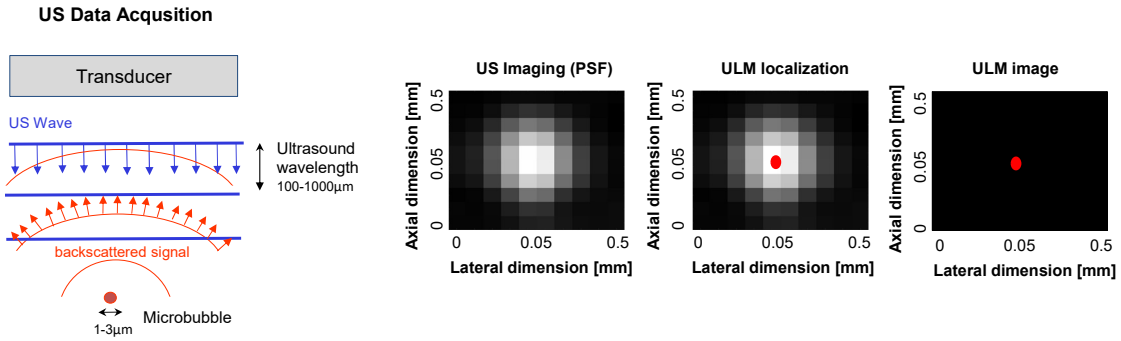

Figure 1.5: Principle of US data acquisition using a plane wave. The MB produces a backscatterd wave. The PSF images the MB as bigger than it really is because of the resolution limit. In ULM, the MB is precisely localized, increasing US imaging resolution. Image inspired by [30].

turn depends on the transducer bandwidth. A shorter pulse length improves axial resolution [25]. Spatial resolution ranges from 50 μm to 1 mm, making veins and capillaries undistinguishable to conventional US imaging [26, 27].
There are various ways to generate US images. In conventional US, the transducer emits a focused beam by applying delays to each element of the transducer in transmission and reception. Instead, in ultra-fast imaging, or plane wave imaging, an aperture (typically all the elements of the transducer) transmit one or few unfocused plane waves. A schematic view of US plane wave acquisition is shown in figure 1.5. The advantage of plane wave imaging lies in the high frame rate (FR) achievable since only one or few emissions are needed to produce an image. After the emission of the ultrasound beam, the backscattered signal is recorded by the same transducer. The signal is referred to as RF signal. The RF signals can be transformed to b-mode images by filtering, envelope detection, log-compression, digitalization, and converting to gray-scale.

1.3.2 Point Spread Function

The Point Spread Function (PSF) represents the spatial impulse response of the ultrasound system [28] and depends on various factors among which transmit and receive parameters, speed of sound in the medium and its variations, depth, and transducer characteristics [28, 29]. The quality of the US image can be determined by the PSF. In fact, the spatial resolution can be practically defined as the full width half maximum (FWHM) of the PSF along the axial and lateral axis. An example of PSF of a contrast agent (diameter 3 μm) acquired with plane wave imaging and transmission frequency of 3 MHz is shown in figure 1.5.

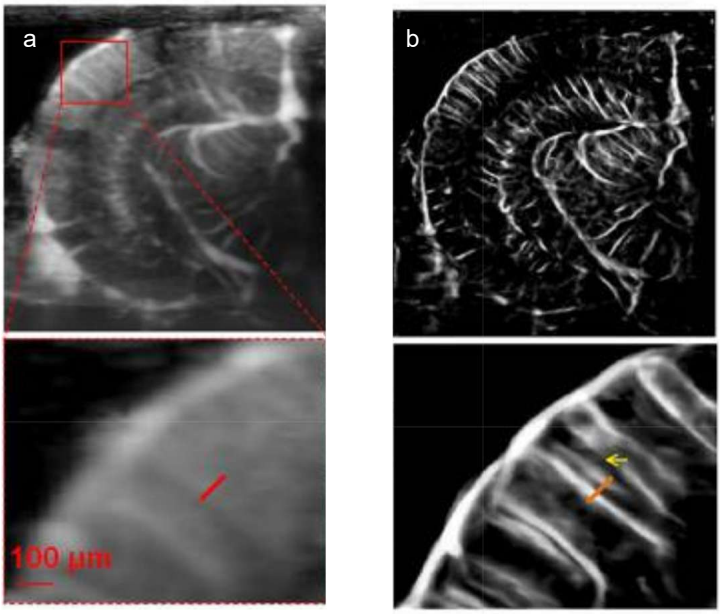

Figure 1.6: Imaging of the rat brain using Doppler (a) and ULM (b), with two highlighted ROIs. Image taken from [33].

1.3.3 Vascular Ultrasound Imaging

US-based vascular imaging modalities including Doppler and Contrast Enhanced Ultrasound are next described.

Doppler

The blood flow in large vessels can be characterized by Doppler. Doppler is a non-contrast ultrasound imaging method, which uses the shift in frequency between transmitted and received signals (Color Doppler) or the energy (Power Doppler) produced by red blood cells backscattered signal to estimate the velocity [31]. Plane wave imaging enhances Doppler capability to image smaller vessels, giving birth to ultrafast Doppler. The key behind ultrafast Doppler imaging is the use of plane wave imaging to achieve thousands of frames per second and capture smaller changes in blood flow [31, 32]. The major advantages of Doppler are portability, contrast-free and high temporal resolution. Limitations remain the need of high FR, high computational power and electronics demand [8]. An example of brain vascular imaging through Doppler is shown in image 1.6(a) with a magnified Region of Interest (ROI). The ROI highlights the low resolution of images obtained with Doppler.

Contrast Enhanced Ultrasound

In Contrast Enhanced Ultrasound (CEUS) the backscattered signals produced by injected MBs are used to gather information about underlying vascular structures [34, 35]. An

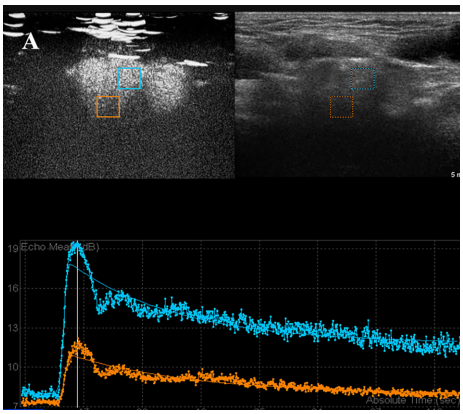

Figure 1.7: Image of a Carothid Body Tumor through CEUS, b-mode image and visualizing the TICS for two ROIs (in blue and red), image from [36].

example of CEUS intensity analysis is the time-intensity curve (TIC), where the maximum pixel intensity over time is evaluated (figure 1.7). The TIC curve allows to derive a number of clinically relevant indexes. Among these, perfusion parameters such as time-to-peak, peak enhancement and area-under-the-curve. One of CEUS main limitation is the high variability of the results, which depend on the scanner setting, patient and MBs injection, and dosage. Furthermore, CEUS does not allow to individually visualize microvessels and characterize their flow [14, 34].

1.3.4 Microvascular Ultrasound Imaging

Ultrasound Localization Microscopy

Ultrasound Localization Microscopy (ULM) fills an important gap in microvascular imaging, allowing to visualize vascular structures at a micrometric scale. The technique allows for bigger penetration depths with respect to optical imaging, while providing a better resolution with respect to non-optical methods such as MRI, CT and conventional US. As an example, the improvement in spatial resolution between ULM and Doppler images is highlighted by the ROI in figure 1.6.
Inspired by optical localization microscopy [37], the pioneering work by Couture et al. [38] and later by Errico et al. [39] demonstrated that ULM could achieve an impressive lateral resolution of 6.3 μm, which is significantly finer than the typical 200-300 micrometer resolution of standard ultrasound imaging [40]. The core of ULM lies in the localization of a point target (i.e. microbubbles) with a resolution far below the diffraction limit. For example, the PSF of a 3 μm diameter microbubble (MB) imaged by conventional US imaging appears in the order of several hundred of μm (Fig. 1.5), due to the normal spatio-temporal sampling in US. In ULM, a MB PSF can be localized with a microscopic precision, see figure 1.5. Repeating the localization process and accumulating the resulting MB centroids for multiple MBs flowing in the circulation, it is possible to obtain micro-resolved images of the vascular structures crossed by MBs. Besides the resolution, a key feature of ULM is the possibility to track MBs. Having the MB positions at different

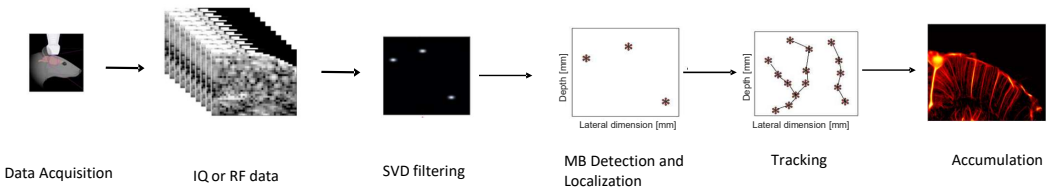

Figure 1.8: ULM framework.

time points, it is possible to track them and derive flow velocity quantification, such as flow direction and flow magnitude. In figure 1.6 is displayed an example of ULM imaging of the brain. ULM is particularly beneficial for visualizing microvascular structures, such as capillaries and small blood vessels, thereby improving diagnostic capabilities [41–44].

1.3.5 Monodysperse vs polydisperse Microbubbles

Thanks to the enhanced backscattered signal produced by MBs, CEUS and ULM improve vascular imaging [45, 46]. These techniques make use of polydisperse MBs, in which the radius of a MBs suspension varies in the range 1-10 μm [47]. Because MB signals depend on various factors, among which MB size, shell characteristics, ultrasound pressure and frequency [48, 49], there has been a tendency to replace the polydisperse with monodisperse MBs. Being characterized by a narrow size distribution, monodisperse MBs guarantee consistent behavior [50], improved acoustic performance, and reduced artifacts [51, 52]. Furthermore, monodisperse MBs could be useful for deeper vessels imaging, thanks to the possibility of optimally tuning the imaging frequency on MBs characteristics.

1.4 Ultrasound Localization Microscopy

1.4.1 How does it work

ULM relies on the precise localization and tracking of MBs injected in the circulation to characterize microvascular structures with sub-millimetric precision. As shown in Fig. 1.8, a traditional ULM framework consists of six basic steps: data acquisition, pre-processing and filtering, MB detection, MB localization and tracking, and track accumulation.

1. **Data acquisition**: Data are acquired after MB injection, which can be either performed through continuous or through bolus injections. US data are acquired as a set of 2D or 3D videos, at a conventional or ultrafast FR. Standard ULM demands data acquired at high FR (kHz range) [53]. The received data can be collected as pre-beamformed RF or IQ data, as well as beamformed images.

2. **Pre-processing**: US data is pre-processed to reduce clutter and tissue noise, and to suppress motion. Common technique to remove background and tissue signals

are background subtraction [54, 55] and singular value decomposition (SVD) spatio-temporal filtering. For instance, SVD allows to distinguish MBs signal from the surrounding tissue by decomposing the signal into its spatial and temporal components. Since background tissue signal is more spatio-temporally coherent with respect to the signal coming from moving MBs, by eliminating the first k singular values, the tissue signal is filtered out from the data [56, 57].

3. **Detection**: The goal of detection is to isolate candidate PSF patches containing MBs. MB signals are detected on either pre-beamformed RF data or on B-mode images. Detection on RF data can be performed by fitting a parabola to the spheric wave generated by a point scatterer [38, 58]. Instead, detection on US images can be performed based on the pixels intensity in each frame [57] or normalized cross correlation [59, 60].

4. **Localization**: Each MB is localized by evaluating the corresponding centroid from PSF patches obtained from the detection step. There are various methods to perform localization such as Gaussian fitting [39, 57, 61], weighted average [57, 62, 63], or radial symmetry [57]. Deep learning has also been applied for MBs localization [64–68].

5. **Tracking**: One key advantage of ULM is its ability to uncover flow dynamical features by tracking MBs, thus improving the final vascular image quality and estimate MBs velocities. Since generally tracking associates MBs over consecutive frames based on MBs distances, its performance depends on factors such as FR used to acquire data. High FR are preferred to track fast moving MBs. To improve tracking performance and eliminate spurious noise tracks, a threshold on track length can be defined. Tracking algorithms include the Hungarian algorithm, based on optimally matching MBs in subsequent frames based on distances [57, 69–71], Markov chain [63] and Kalman filtering [60, 72].

6. **Accumulation**: ULM intensity maps are obtained by accumulating the tracks, previously smoothed and interpolated to fill in the missing points. Velocity and velocity-direction map are generated by evaluating MB velocity and direction at each pixel corresponding to a MB localization.

1.5 Thesis Objective

ULM has bypassed the penetration-depth and resolution trade-off of conventional US imaging. By characterizing vascular structures at a sub-millimetric scale, ULM could represent a groundbreaking clinical tool for the diagnosis and treatment of various diseases. Although the method has been implemented in various preclinical [44, 73, 74] and clinical studies [61, 75–77], its clinical translation is slowed down by the following factors:

1. **Long acquisition times**. MBs signals need to be spatially isolated for localization. If MBs PSF overlap, precise MB localization becomes challenging [78]. Figure

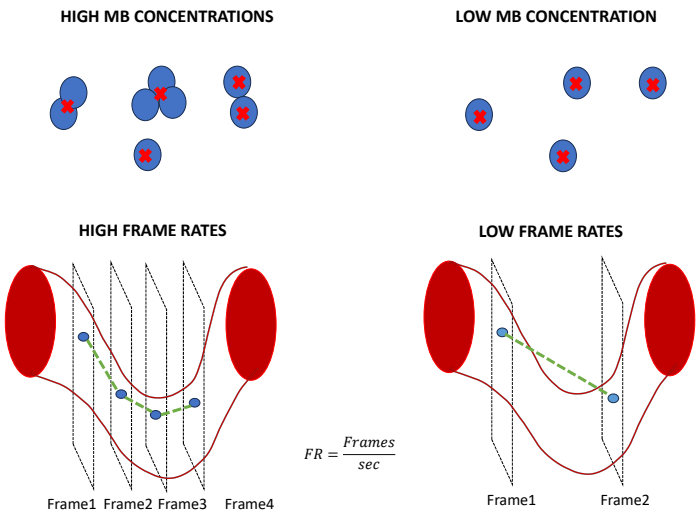

Figure 1.9: Schematic view representing scenarios with high MB concentrations (overlapping PSFs), where localization becomes more difficult, and low MB concentrations. On the lower side, high FR acquisition, where tracking MB is easier compared to low FR. The green dashed line shows the track of the MB flowing in the vessel.

1.9 shows an example of overlapping MBs signals, compared to a sparse scenario. This sparsity constraint practically translates in low MB concentrations, reducing the likelihood of signal overlap. However, such low concentrations require prolonged acquisition times to accumulate a sufficient number of MB events for reliable vascular characterization. Extended acquisition times are also essential for imaging smaller vessels with low perfusion rates [30]. In preclinical settings, ULM typically requires several minutes of continuous data acquisition. When translated to human imaging, this acquisition time would need to be further extended, presenting a significant challenge for integration into routine clinical practice. Furthermore, extended acquisitions also increase susceptibility to motion artifacts, which can introduce localization errors and degrade overall image quality [30, 61].

2. **High frame rate**. ULM requires high FR to coherently track MBs. In fact, many tracking algorithms match MBs based on minimizing their pair-wise distance in consecutive frames. Since the assignment depends on the frame-to-frame distance, high FR are fundamental to accurately pair MB signals [79, 80]. As shown in Fig. 1.9, if FR are high, tracking MBs flowing in a vessels is more representative of vascular geometry and less prone to erroneous matches. As a consequence, US data for ULM imaging are generally acquired at high FR (i.e. in the order of kHz). However, such high FR are generally beyond the capabilities of clinical US scanners, which typically operate up to 100 Hz FR [81].

3. **Lack of validation methods**. For ULM to be reliably adopted in clinical practice, particularly for image generation and quantitative vascular analysis, rigorous

validation of the results is essential. Validation can be achieved using ground truth data obtained either *in silico* or *in vitro*. *In silico* approaches simulate vascular flow, providing known ground truth for MB positions and velocities. However, such simulations are limited by their inability to fully capture the complex MB to MB and MB to vessel interactions. Additionally, these simulations are computationally intensive and often rely on simplified models [82, 83]. Conversely, *in vitro* experiments allow algorithms to be tested on physical systems, offering a more tangible evaluation framework. Nevertheless, these experiments also face constraints in reproducing the full physiological and anatomical complexity of *in vivo* environments.

1.6 Structure of the thesis

The key challenges presented in the previous section are addressed in this thesis, where novel algorithms are proposed and evaluated to help the clinical integration of ULM in clinical practice.

Chapter 2 presents a method to relax the constraint on high FR required by ULM. In particular, it proposes the use of Radial Basis Function (RBF) interpolators to up-sample US data from low to high FR based on spatio-temporal information. The results validate the use of this technique in a variety of preclinical *in vivo* data, successfully reconstructing ULM images with a FR as low as 100 Hz.

In Chapter 3 we take a further step by applying the RBFs interpolation technique along two directions and combine the interpolated results. The use of a bi-directional interpolation helps to improve recovery of data not only structurally, but also regrading the dynamics. This method is validated for two scenarios: to reduce either the FR or the acquisition time.

Chapter 4 focuses on ULM long acquisition times constraint by utilizing a bi-disperse MB population. The uncoupling of the bi-disperse population may allow for increased MBs concentration, reducing the acquisition times. The technique is tested on *in vitro* data acquired in a 3D printed phantom. In addition, this chapter also introduces the possibility of 3D printing vascular models for ULM validation.

Chapter 5 extends the use of the bi-disperse MB population, proposing the use of Orthogonal Frequency Division Multiplexing as uncoupling method. The proposed methodology is tested in a vascular phantom.

Chapter 6 draws the conclusion of the thesis, open issues and possible future works are also discussed.

Chapter 2

Time Efficient Ultrasound Localization Microscopy Based on A Novel Radial Basis Function 2D Interpolation

This Chapter[1] *relaxes the requirement of high frame rates (FRs) to obtain microvascular images using Ultrasound Localization Microscopy (ULM). To this end, we propose a new time-efficient ULM (TEULM) pipeline built on a cutting-edge interpolation method. More specifically, we suggest employing Radial Basis Functions (RBFs) as interpolators to estimate the missing values in the 2-dimensional (2D) spatio-temporal structures. To evaluate this strategy, we first mimic the data acquisition at a reduced FR by applying a down-sampling (DS = 2, 4, 8, and 10) factor to high FR ULM data. Then, we up-sample the data to the original FR using the suggested interpolation to reconstruct the missing frames. Finally, using both the original high FR data and the interpolated one, we reconstruct SR images using the ULM framework steps. We evaluate the proposed TEULM using four in vivo datasets, a Rat brain (dataset A), a Rat kidney (dataset B), a Rat tumor (dataset C) and a Rat brain bolus (dataset D), interpolating at the in-phase and quadrature (IQ) level. Results demonstrate the effectiveness of TEULM in recovering vascular structures, even at a DS rate of 10 (corresponding to a FR of sub-100Hz). In conclusion, the proposed technique is successful in reconstructing accurate SR images while requiring FRs of one order of magnitude lower than standard ULM.*

2.1 Introduction

Despite the advantages that ULM may bring in the clinical setting, its utilization is currently limited by high FR is necessary to coherently pair the MB signals from one frame to the successive one [79, 80, 84]. To date, this need for high FRs has hampered

[1]This Chapter appears in:
[J0] Tuccio G., Afrakhteh S., Iacca G., Demi L., "Time Efficient Ultrasound Localization Microscopy Based on A Novel Radial Basis Function 2D Interpolation" in IEEE Transactions on medical imaging, 2024

the ULM clinical translation.

Guo et al. [79] evaluated by a quantitative investigation the loss of ULM performance when decreasing the FR. The study demonstrates, by utilizing an in vivo dataset, that a decreased FR results in an unreliable microbubble detection and tracking, which in turn leads to a decreased spatial resolution (from 9.9 μm to 15 μm when going from 1kHz to 250Hz) as well as a decreased saturation (saturation drop above 50% from 1kHz to 100Hz). Furthermore, the FR has a significant impact on the precision of the velocity measurements.

To tackle the high FR requirement, Ackerman et al. [63] and Opacic et al. [61] implemented a modified Markov chain Monte Carlo data association to recover UCA tracks at a lower FR, which optimally associate MBs positions based on an underlying motion model. Another approach [60] uses a Kalman filter as a tracking backbone, and introduces MB image features on top. Although these approaches can recover UCAs tracks at a lower FR, their improved performance comes at a significant computational cost. Enabling lower FR acquisitions using TEULM would alleviate some of the data size constraints for ULM and would make the technology more pragmatic for clinical translation, where low FRs are standard. To be more precise, adopting lower FR acquisitions in ULM can bring about numerous advantages in the clinical context. These benefits encompass reduced data size, compatibility with standard equipment, and cost-effectiveness.

In this study, we aim at bridging the gap between the high FRs required by ULM (in the range of 1kHz) and the limited FR of the standard clinical scanners (in the sub-range of 100Hz).

To this end, we propose a new time-efficient ULM (TEULM) pipeline based on a novel 2-dimensional (2D) interpolation technique to relax the requirement on the high FR necessary to obtain super-resolved images. The article is structured as follows. Section 2.2 gives a detailed explanation of the interpolation technique used upstream the ULM pipeline. Next, we describe the key steps of ULM framework, as well as the TEULM pipeline. In the result section (Sec. 2.3), we quantify the quality of the reconstructed images using TEULM, and compare these images with the SR images obtained through standard ULM. Finally, we provide the discussion and conclusions of the proposed method.

2.2 Materials and Methods

2.2.1 RBF-based 2D interpolation

Radial Basis Functions (RBFs) have been frequently used in recent years to interpolate high-dimensional sparse data [85, 86]. The main advantage of this technique is that it delivers respectable numerical results without entailing complicated computations. This makes it simple to apply to complicated geometries in a variety of spaces. In the following, we provide the formulation of the 2D interpolation problem using RBFs.

Given the data $(\mathbf{X}_j, \mathbf{Y}_j)$, $j = 1, 2, \ldots, N$, where $\mathbf{X}_j$ and $\mathbf{Y}_j \in \mathbb{R}^d$ (in our problem $d = 2$), we aim to find a continuous function $S(\mathbf{X})$ so that $S(\mathbf{X}_j) = \mathbf{Y}_j \; \forall j \in \{1, 2, \ldots, N\}$. In addition, the interpolation bases are chosen as $\{\phi(\mathbf{X} - \mathbf{X}_1), \phi(\mathbf{X} - \mathbf{X}_2), \ldots, \phi(\mathbf{X} - \mathbf{X}_N)\}$, where $\mathbf{X}_1, \mathbf{X}_2, \ldots, \mathbf{X}_N$ are predetermined interpolation nodes. These assumptions lead to

the definition of RBFs as:

$$\phi(r_j) \equiv \phi(\|\mathbf{X} - \mathbf{X}_j\|) = \sqrt{\|\mathbf{X} - \mathbf{X}_j\|_2^2 + \tau^2} \tag{2.1}$$

where $\|\cdot\|_2$ indicates the ℓ^2 norm (i.e., the Euclidean distance) and τ represents the so-called shape parameter. Due to their radial dependence, these functions are referred to as RBFs. Some possible RBFs are listed in Table 2.1.

Table 2.1: RBF basis used in this study (ϵ is a constant, r is the radius of the RBF, and $Ln(.)$ indicates the natural logarithm).

Method	**Acronym**	**Formula**
Infinitely smooth		
Multiquadric	MQ	$\phi(r) = \sqrt{1 + (\epsilon r)^2}$
Inverse multiquadric	IMQ	$\phi(r) = \frac{1}{\sqrt{1+(\epsilon r)^2}}$
Gaussian	GA	$\phi(r) = e^{-\epsilon r^2}$
Piece-wise smooth		
Cubic	CU	$\phi(r) = \|r\|^3$
Thin plate spline	TPS	$\phi(r) = r^2 Ln\|r\|$

Following that, we develop a linear combination of RBFs $\phi(r)$ to move forward with the 2D interpolation:

$$S(\mathbf{X}) = \sum_{j=1}^{N} \beta_j \phi(\|\mathbf{X} - \mathbf{X}_j^c\|_2, \tau), \tag{2.2}$$

where $\mathbf{X} = (x_1, x_2, \ldots, x_d)$, τ is the shape parameter, β_j is the interpolation coefficient, and $r = \|\mathbf{X}\|_2$. If we intend to estimate $f : \mathbb{R}^d \to \mathbb{R}$ utilizing the interpolators determined by Eq. (2.2), we need to find the interpolation coefficients β_j. To do that, we use the following interpolation condition:

$$S(\mathbf{X}_j) = f(\mathbf{X}_j),\ j = 1, 2, \ldots, N. \tag{2.3}$$

By applying Eq. (2.3) at the central points of $\mathbf{X}_j^c$ for $j = 1, \ldots, N$, we obtain the linear system:

$$\mathbf{\Phi}_{N\times N}\mathbf{B}_{N\times 1} = \mathbf{F}_{N\times 1} \qquad \mathbf{B} = [\beta_1, \beta_2, \ldots, \beta_N]^T \tag{2.4}$$

which can be expanded as follows:

$$\underbrace{\begin{bmatrix} \phi(r_{1,1}) & \phi(r_{1,2}) & \ldots & \phi(r_{1,N}) \\ \phi(r_{2,1}) & \phi(r_{2,2}) & \ldots & \phi(r_{2,N}) \\ \vdots & \vdots & \ddots & \vdots \\ \phi(r_{N-1,1}) & \phi(r_{N-1,2}) & \ldots & \phi(r_{N-1,N}) \\ \phi(r_{N,1}) & \phi(r_{N,2}) & \ldots & \phi(r_{N,N}) \end{bmatrix}}_{\mathbf{\Phi}} \underbrace{\begin{bmatrix} \beta_1 \\ \beta_2 \\ \vdots \\ \beta_{N-1} \\ \beta_N \end{bmatrix}}_{\mathbf{B}} = \underbrace{\begin{bmatrix} f(\mathbf{X}_1) \\ f(\mathbf{X}_2) \\ \vdots \\ f(\mathbf{X}_{N-1}) \\ f(\mathbf{X}_N) \end{bmatrix}}_{\mathbf{F}} \tag{2.5}$$

where $\mathbf{X}_j$ indicates the imaging pixels, $f(X_j)$ refers to the pixel intensity of the imaging point X_j, $r_{i,j} = \|\mathbf{X}_i^c - \mathbf{X}_j^c\|$ is the Euclidean distance, and N is the number of points in the 2D grid (i.e., the imaging points in our problem).

Based on the system in Eq. (3.2), to solve the interpolation problem (i.e., finding the β values), we must invert the coefficient matrix $\mathbf{\Phi}$, as discussed in the next section. Now, using the coefficients calculated from the above system, if we seek to analyze the interpolator at M points $\mathbf{X}_i,\ i = 1, 2, \ldots, M$, the new coefficients matrix entries must be constructed as follows: $h_{ij} = \phi(\|\mathbf{X}_i - \mathbf{X}_j^c\|_2)\ \forall j \in \{1, \ldots, N\}$. Finally, the following matrix multiplication is used to evaluate the interpolant at the M points:

$$\mathbf{F}_{est} = \mathbf{HB} = \mathbf{H\Phi}^{-1}\mathbf{F}, \tag{2.6}$$

where $\mathbf{F}_{est}$ represents the estimated $\mathbf{F}$ (i.e., in our interpolation problem, $\mathbf{F_{est}}$ indicates the interpolated data).

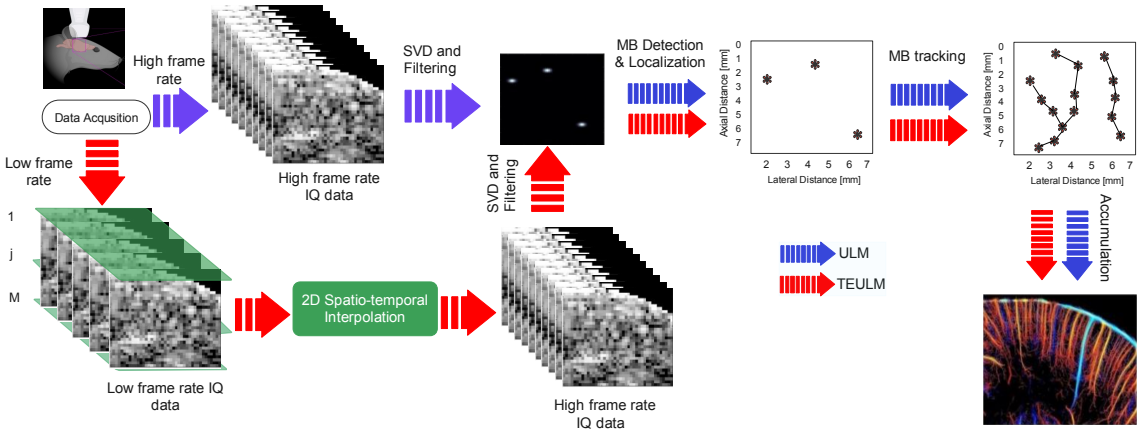

Figure 2.1: Main processing steps of Ultrasound Localization Microscopy (ULM) and Time Efficient Ultrasound Localization Microscopy (TEULM).

2.2.2 Proposed Approach

Standard ULM framework

As shown in Fig. 2.1, the traditional ULM framework consists of five basic steps: data acquisition, pre-processing and filtering, MB detection, MB localization and tracking, and accumulation. For the data acquisition step, the standard framework demands data acquired at high FRs. Following that, the high FR data is pre-processed to reduce clutter and tissue noise. In this study, we employ singular value decomposition (SVD) spatio-temporal filtering to distinguish the MBs signal from the surrounding tissue [56]. The SVD filter takes advantage of the fact that back-scatter tissue signals have a high spatio-temporal coherence compared to MB echoes. Therefore, by eliminating the initial k singular values, the tissue signal is filtered out from the data.

Next, MB signals are detected based on the pixels intensity in each frame. As in [57], an estimate of the number of MBs (i.e., n) in each frame is utilized instead of creating a threshold to identify the minimum pixel intensity value representative of the MB signals, which is non-trivial and may result in poor MB detection. In this paper, for

each frame, the n pixels characterized by the most intense values are selected. Individual MBs are then localized using the Gaussian fitting algorithm [57, 87, 88] , which fits a 2D multivariate Gaussian distribution. This approach assumes that the maximum intensity value (I) in a grid of $[N_z, N_x]$ pixels corresponds to the MB centroid. To recover the super-resolved location, the original image is up-sampled by a resolution factor res. Each pixel is interpolated into a $res \times res$ grid, allowing to localize the MBs with a precision res times higher than the pixel size. The final image is then obtained as a grid of size $[N_z \times res, N_x \times res]$. Here, we define res as the empirical limit found in [57], namely 10. The localization problem can then be mathematically described as an optimization problem. After centering the subspace in the maximum value of the sub-sampled grid, the super-resolved z and x coordinates, (c_z, c_x), of each MB is evaluated as the location of the Gaussian peak as follows:

$$\begin{aligned} \max I &= exp\left(-\left(\frac{(z-c_z)^2}{2\sigma_z^2}+\frac{(x-c_x)^2}{2\sigma_x^2}\right)\right), \\ (z,x) &\in \left(\left[-|\frac{f_z}{2}|,|\frac{f_z}{2}|\right],\left[-|\frac{f_x}{2}|,|\frac{f_x}{2}|\right]\right), \end{aligned} \tag{2.7}$$

where f_z and f_x respectively indicate the FWHM along z and x directions. The standard deviations σ_z and σ_x are empirically evaluated to be equal to 1, as in [57]. Then, the bipartite tracking algorithm matches each detected MB location in a frame-to-frame fashion. Thanks to their simplicity, the bipartite graph-based pairing methods are well established in the ULM context [57, 60, 69, 70, 79, 80, 84]. These algorithms solve the tracking problem through an optimal assignment, based on the MBS frame-to-frame distance. In particular, the relative distance between all the UCAs in two successive frames is evaluated. The MBs are then considered to be the same, or matched, in such a way that the total distance between all the MBs in the two frames is minimized. Since the assignment depends on the frame-to-frame distance, it is easy to understand the importance of a high FR to accurately pair MB signals [79, 80]. This paper implements a modified Khun-Munkres bipartite tracking algorithm, as in [71]. Generally, the method works on the assumption that each MB in one frame is paired with one MB in the subsequent frame. However, due to the uncertainty originated by the arbitrary estimation of the number of MBs in each frame in the localization step, the assumption may result in a sub-optimal solution. Furthermore, a sub-optimal solution might be caused by unpredictable UCAs events, such as MB appearance and/or disappearance. As such, the Khun-Munkres algorithm is modified to cope with partial assignment. In particular, a MB in a frame f which has depleted all the possible assignment options in the next frame $f+1$ is discarded [84]. Moreover, we establish a threshold for the minimum length of a track in order to further strengthen the robustness of the tracking performance, i.e., a track is discarded if it is lower than the threshold because it is considered as noise.

Finally, an SR intensity map is obtained by accumulating the tracks, previously smoothed and interpolated to fill in the missing points, over all frames. The velocity map, which defines a MB's velocity by its displacement over time, can also be retrieved and superimposed onto the SR intensity map.

TEULM framework

TEULM introduces, in the pre-processing stage, the RBF-based 2D interpolation technique to relax the FR required by standard ULM. The interpolation method aids in recovering the lost data, which is the result of adopting a reduced FR acquisition. More specifically, we propose sparse (low FR acquisition) combined with 2D interpolation to reconstruct the unknown information corresponding to the frames that are not recorded in the low FR acquisition (i.e., for a given down-sampling (DS) rate, interpolating DS - 1 middle frames to achieve high FR IQ data needed for high-quality SR imaging). Following that, we adopt the standard ULM framework, described in Section 2.2.2. We pre-process the interpolated data by applying SVD filer first, keeping the k-values used for filtering as the original ones, and successively a Butterworth filter. Then TEULM's framework comprises of detection, localization and tracking of the MBs. The final images are then obtained through accumulation (see Fig. 2.1). ULM and TEULM parameters are summarized in Table 2.3. In the case of using ULM at the original FR and TEULM, we use the same parameters used in [57]. However, for the ULM at down-sampling rates > 1 (non-interpolated data), we adapt the maximum linking distance and minimum track length by a factor that is proportionate to the level of down-sampling. For example, when down-sampling by a factor of 2 (DS=2), the maximum linking distance is adjusted to be twice the original linking distance, while the minimum track length is set to half of its original value. This adjustment is made for a fair comparison, which accounts for the fewer frames used yielding in larger gaps between microbubble positions in consecutive frames. Similarly, due to the reduced number of frames, a shorter minimum track length is necessary.

Table 2.2: Datasets summary in this study.

Dataset	**MB Dose**	**Tilted Angles**
Rat Brain Infusion (dataset A)	400 μl	(-3°; 0°; 3°)
Rat Kidney Bolus (dataset B)	500 μl	(-10°; -5°; 0°; 5°; 10°)
Rat Tumor Bolus (dataset C)	100 μl	(-10°; -5°; 0°; 5°; 10°)
Rat Brain Bolus (dataset D)	400 μl	(-5°; 0°; 5°)

2.2.3 Data

To assess the proposed strategy, we use four *in vivo* datasets. We denote the *in vivo* datasets as dataset A for the Rat Brain, dataset B for the Rat Kidney, dataset C for the Rat tumor and dataset D for the Rat Brain bolus.

The datasets, presented in [57] and summarized in Table 2.2, are recorded with a 15 MHz center frequency probe (Vermon, France). We opted for the use of *in vivo* datasets due to their capacity to encompass a wide range of hemodynamic structures across different organs (such as the brain and kidney) and various injection modalities.

Table 2.3: ULM and TEULM parameters used in this work. * and ** indicate the parameters which were adjusted for the non-interpolated data (ULM at $DS > 1$). In particular, * and ** respectively multiply and divide by a factor equal to the DS rate used.

Dataset	**Frame Rate** (Hz)	**k-value (SVD)**	**Max. Linking Distance***	**Min. Track length****	**Number of MB / Frame**
Dataset A	1000	5	2	15	70
Dataset B	1000	10	1.5	15	100
Dataset C	500	10	1	10	100
Dataset D	1000	10	2	10	100

2.2.4 In vivo evaluation metrics

We use the following metrics to evaluate the TEULM-generated SR image quality and compare it with that obtained by standard ULM.

Root Mean Square Error (RMSE)

The similarity between the original image, reconstructed at 1KHz (I_1), and the images interpolated at different DS rates (I_{DS}), with $DS = 2, \ldots, 10$, is assessed pixel-by-pixel using the root mean square error:

$$RMSE = \sqrt{\sum_{i=1}^{N_{pix}} \frac{(|I_{DS} - I_1|)^2}{N_{pix}}}, \tag{2.8}$$

where N_{pix} denotes the total number of pixels in the reconstructed image. Both density maps, which depict the vascular anatomy, and velocity maps are evaluated. The Root Mean Square Error ($RMSE$) is employed to gauge the resemblance in terms of vascular structure and intensity among the reconstructed images acquired through TEULM and ULM at various levels of DS rates. Indeed, the $RMSE$ conducts a pixel-level assessment of the error, taking into account the image reconstructed from the initial high frame-rate data (1KHz for datasets A, B, and D, and 500Hz for dataset C) as the reference standard.

DICE score

The $DICE$ score evaluates the similarity between two images by measuring the overlapping area of two images over the area of their union [89]:

$$DICE = \frac{2 \times |I_{DS} \cap I_1|}{|I_{DS}| \cup |I_1|}, \tag{2.9}$$

The $DICE$ score quantitatively assesses the resemblance of the reconstructed binary images generated by ULM and TEULM across various DS rates.

Percentage of preserved tracks

Since the number of detected tracks has a significant impact on the saturation and on the quality of the reconstructed images, we analyze the statistics related to the number of tracks at various DS rates. The ratio of the number of tracks found at the various DS rates ($DS = 2, \ldots, 10$) to those found at DS=1 is used to calculate the percentage of preserved tracks. The percentage of preserved tracks is evaluated for density maps only. In ULM, a density map refers to a spatial representation of vessel density within a region of interest.

Saturation

We further assess the TEULM performance at different DS rates through saturation (i.e., indicating the number of pixels crossed by MBs) [79, 80]. The evaluation of the saturation is meaningful since the reconstructed images are the result of the accumulation of the pixels crossed by the MBs. In this study, the saturation curve is calculated as the percentage of filled pixels over the total area of the image. The saturation is evaluated only for density maps.

Fourier Ring Correlation (FRC)

Fourier Ring Correlation is a commonly used method in the ULM context to estimate the spatial resolution of the super-resolved images [90]. The FRC evaluates the spatial frequency correlation along iso-spatial frequency rings (r_i) between two sub-images in the frequency domain, formed by random splitting the tracks:

$$FRC(r_i) = \frac{\sum_{r \in r_i} F_1(r) F_2(r)^*}{\sqrt{\sum_{r \in r_i} |F_1(r)|^2 \sum_{r \in r_i} |F_2(r)|^2}}. \tag{2.10}$$

The resolution is the inverse value of the FRC curve, when the FRC drops below the threshold value. In this study, we select the 1/2 bit as thresholding method, which corresponds to the highest spatial frequency necessary to collect the information to fill half a bit [91, 92]. To achieve an unbiased and objective quantification, we conduct global (i.e., whole image) FRC resolution estimates.

2.3 Results

In this section, we present the results obtained through TEULM using the *in vivo* datasets described in section 2.2.3.

We provide the *in vivo* results of standard ULM on the original high FR data (namely, 1kHz for dataset A, B and D and 500Hz for dataset C), see Fig. 2.2. These images are considered as a reference. Figures 2.3, 2.4, 2.5, and 2.6 depict the ULM and TEULM reconstructed density and velocity maps for datasets A, B, C, and D, respectively, across different DS rates. It's worth emphasizing that for dataset C, we provide the results until down-sampling 6 (which implies a FR of 83Hz) which demonstrates the capability

of our proposed TEULM approach to the FRs close to the current clinical system's FR. In addition, it should be noted that conventional ULM fails to reconstruct any tracks using a higher down-sampling ($DS \geq 7$). The results show that for $DS \geq 2$, TEULM performs better than standard ULM in recovering the local and global information (i.e., ULM even fails to recover the global information at higher DS rates). As expected, a decrease in the FR (from left to right) results in a proportional degradation in the image quality. Qualitatively, the vessel definition appears to be less continuous and more blurry at higher DS rates compared to the original images, see Fig. 2.2. We quantitatively assess this loss of definition in TEULM's generated density maps through the spatial resolution obtained using FRC on the entire image (Table 2.4), for all the *in vivo* datasets. The Fourier Ring Correlation evaluates the spatial resolution as the correlation between 2 sub-images formed by randomly splitting the tracks forming the density maps.

In addition, we evaluate the consistency of the density maps generated by TEULM and ULM with the ones obtained using the high FR data using the DICE score, see Table 2.5. For all the *in vivo* datasets, we further evaluate the efficiency of the proposed technique by means of two of the previously introduced metrics: the percentage of preserved tracks, and the saturation. The metrics are shown in Fig. 2.8 considering down-sampling 2, 4, 8 and 10. Fig. 2.8 clearly shows that TEULM preserves the majority of the tracks, as well as a constant saturation level compared to ULM, for which both the metrics decrease exponentially with increasing down-sampling.

Table 2.4: Spatial resolution (in μm) measured by the FRC curve and the 1/2 bit thresholding method for the high FR ULM (1KHz for datasets A, B and D and 500Hz for dataset C) and TEULM at different DS rates for the *in vivo* datasets.

	Original	$DS = 2$	$DS = 4$	DS 8	$DS = 10$
Dataset A	11.49	10.27	11.35	14.5	17.8
Dataset B	26.3	25.71	27.9	28.6	30.3
Dataset C	24.75	25.8	26.52	30.95	33.11
Dataset D	13.9	12.94	13.74	19.72	20.08

When under-sampling, we can generate multiple datasets from the high FR data. To assess the consistency across different datasets, we generate the permutation starting from frame 6 at down-sampling of 10 and compare the results with respect to the dataset generated starting from frame 1. The choice of the permutation allows us to evaluate the performance of the proposed approach for the most asynchronous couple of data that we could generate. Particularly, we assess the performance of TEULM through the statistical results (mean $\pm$ standard deviation) of the $DICE$ score, the saturation percentage, and the percentage of preserved tracks. The results of the DICE score are presented in Table 2.5. The percentage of preserved tracks for dataset A, B, C, and D is $0.98 \pm 7 \times 10^{-4}$, $0.77 \pm 4 \times 10^{-2}$, $0.37 \pm 1 \times 10^{-2}$, and $0.83 \pm 2 \times 10^{-2}$, respectively. In addition, the saturation percentage reaches the value of $0.96 \pm 2 \times 10^{-2}$, $0.68 \pm 1 \times 10^{-2}$, $0.77 \pm 3 \times 10^{-2}$, and $0.9 \pm 1 \times 10^{-2}$ for dataset A, B, C, and D, respectively. The results certify the consistency of TEULM across permutations.

In addition, we analyze the influence of the FR on the velocity maps obtained with

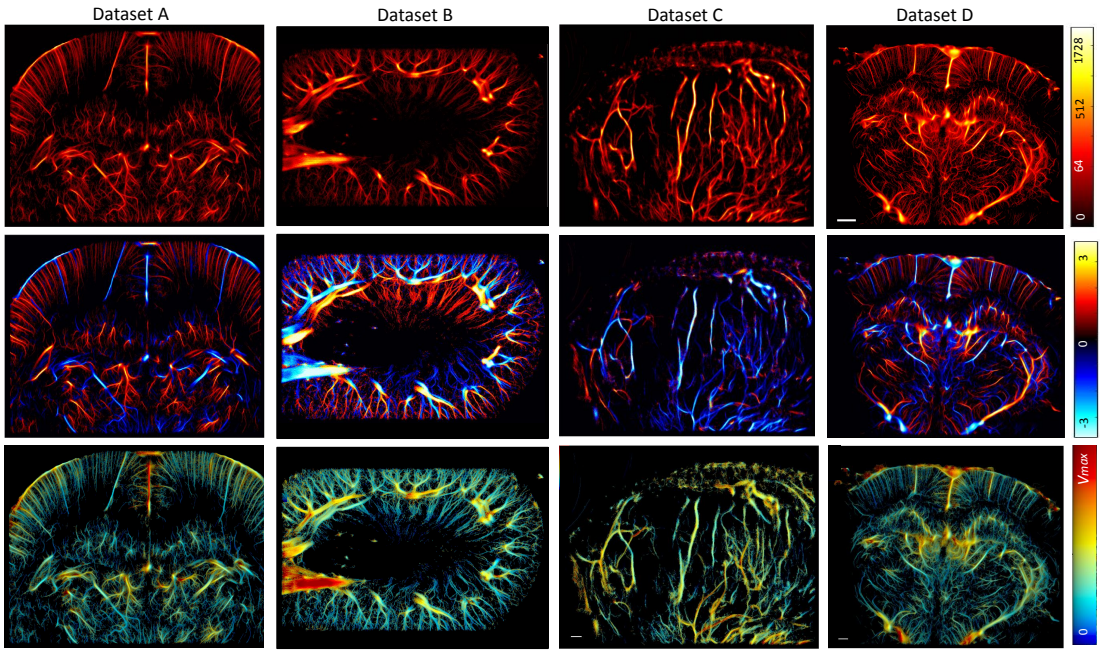

Figure 2.2: Reconstructed density maps (first row), flow direction map (second row) and velocity magnitude maps (third row) for the *in vivo* datasets using the original high FR data (1kHz for dataset A, B and D and 500Hz for dataset C). The colorbar of the density maps shows the number of counts of MBs centroids found in each pixel of the image. The colorbar of the Flow direction map indicates values in $MBs/(pix.sec)$. The Velocity magnitude color-map encodes different mean velocities. Red corresponds to the maximum velocity (V_{max}) of 70 mm/s, 40 mm/s, 48 mm/s and 63 mm/s for dataset A, B, C and D, respectively).

TEULM and ULM. To this end, we calculate the flow direction and the velocity magnitude maps for the *in vivo* datasets. For the rendering of the flow direction of the blood flow, we use the red and blue colors to encode the different directions (see second row of Figs. 2.3, 2.4, 2.5, and 2.6, for dataset A, B, C and D respectively). About the mean velocity magnitude encoding (see the third row of Figs. 2.3, 2.4, 2.5, and 2.6, for dataset A, B, C and D respectively), the slowest velocities are encoded in blue, whereas the high velocities are encoded in red. The results of the velocity profiles, provided in row two and three of the Figures 2.3 (dataset A), 2.4 (dataset B), 2.5 (dataset C), and 2.6 (dataset D), clearly show that there is a lower limit to the FR reduction under which it is not possible to recover the global and local velocity information of the vascular structure.

Moreover, we quantify the error for both the intensity and velocity maps of the sparse ULM and TEULM with respect to the original ULM (i.e., obtained with a FR equal to 1kHz for dataset A, B and D and FR equal to 500Hz for dataset C) utilizing the $RMSE$ metric (Figure 2.7). The results allow us to evaluate the trend of these two metrics with respect to different DS rates, up to 50Hz [1].

Finally, we have conducted an evaluation of the mean velocity profiles for all the in vivo datasets (see Fig. 2.9). These profiles represent the mean velocity values (in mm/s)

[1]Intensity maps available in the link.

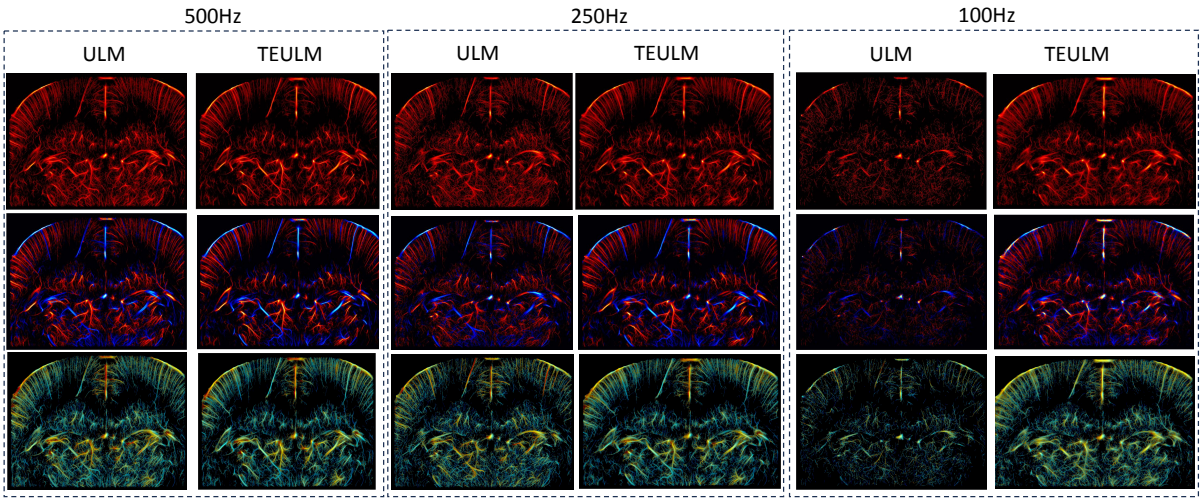

Figure 2.3: ULM- and TEULM-generated density maps (first row), flow direction map (second row), and velocity magnitude map (third row) for Dataset A at different FRs of 500Hz (DS=2), 250Hz (DS=4) and 100Hz (DS=10). The color bar of the figure is the same as original ones in Fig. 2.2.

Table 2.5: $DICE$ score for all the *in vivo* datasets of ULM and TEULM density maps. $\star$ indicates that for TEULM at DS=10, we present the mean and the standard deviation of the $DICE$ score with respect to two permuted datasets.

Dataset	**Method**	DS **rates**			
		2	4	8	$10^{\star}$
Dataset A	TEULM	0.90	0.87	0.8	$0.79 \pm 5 \times 10^{-4}$
	ULM	0.78	0.60	0.29	0.19
Dataset B	TEULM	0.87	0.85	0.82	$0.81 \pm 1 \times 10^{-4}$
	ULM	0.76	0.49	0.20	0.14
Dataset C	TEULM	0.72	0.72	0.69	$0.68 \pm 7 \times 10^{-5}$
	ULM	0.43	0.21	-	-
Dataset D	TEULM	0.91	0.89	0.84	$0.82 \pm 2 \times 10^{-4}$
	ULM	0.82	0.73	0.58	0.52

against the number of tracks associated with each mean velocity across all the tracks within their respective datasets. Fig. 2.9 shows that the mean velocities are misestimated at higher down-sampling, confirming that recovering the dynamic profile is a challenging task for the RBFs interpolators.

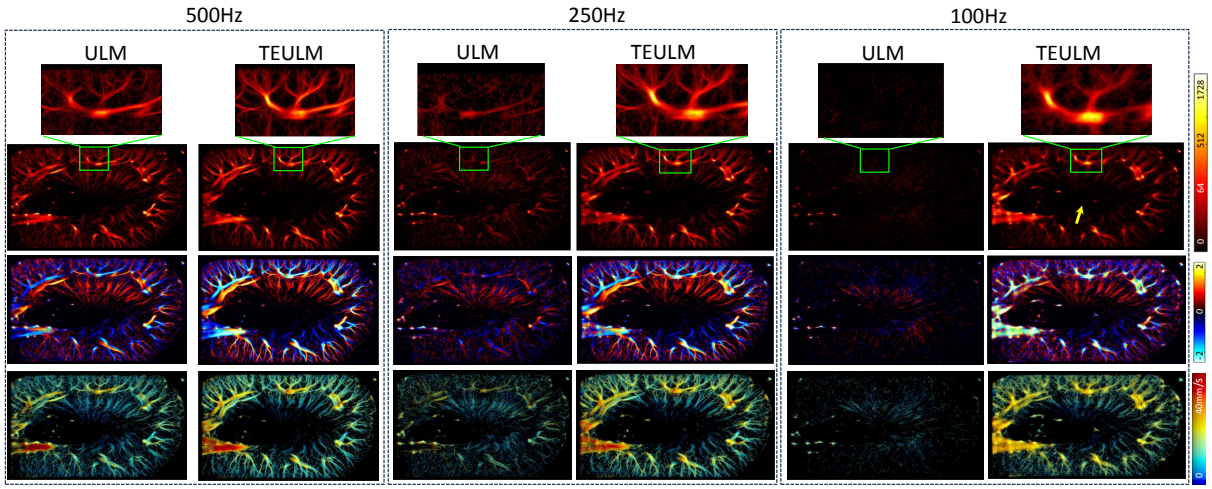

Figure 2.4: ULM- and TEULM-generated density maps (first row), flow direction map (second row), and velocity magnitude map (third row) for Dataset B at different FRs of 500Hz ($DS = 2$), 250Hz ($DS = 4$) and 100Hz ($DS = 10$). The color bar of the figure is the same as original ones in Fig. 2.2.

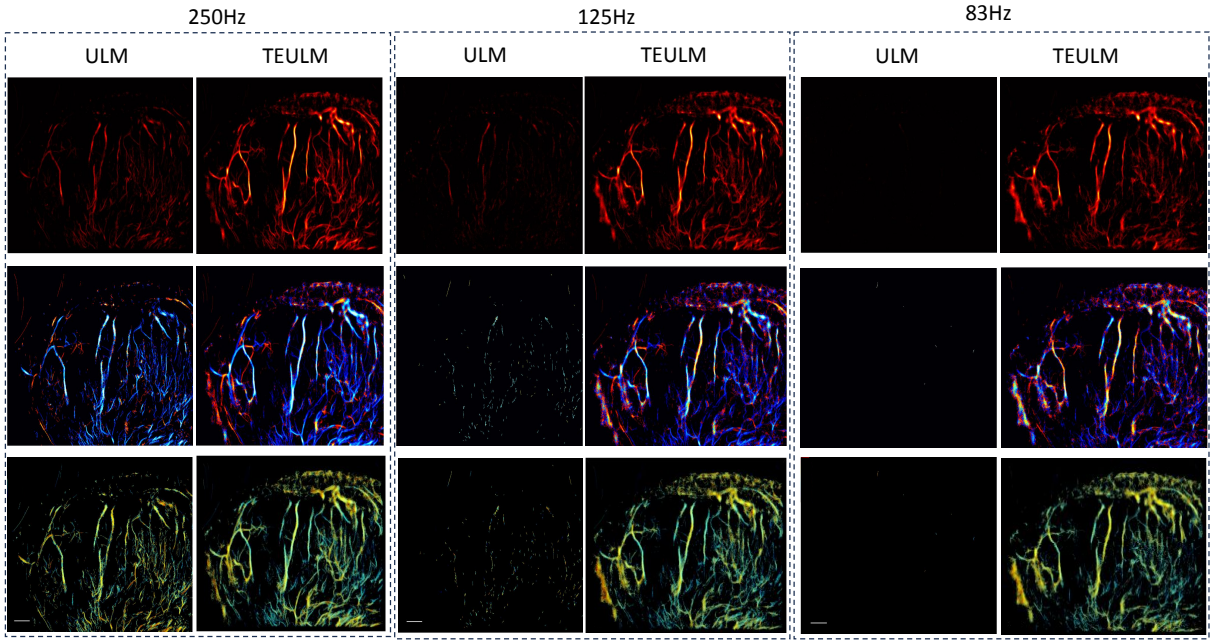

Figure 2.5: ULM- and TEULM-generated density maps (first row), flow direction map (second row), and velocity magnitude map (third row) for Dataset C at different FRs of 250Hz ($DS = 2$), 125Hz ($DS = 4$) and 83Hz ($DS = 6$). We have presented images up to a DS rate of 6 because, at higher DS rates, ULM is unable to recover any tracks. The color bar of the figure is the same as original ones in Fig. 2.2.

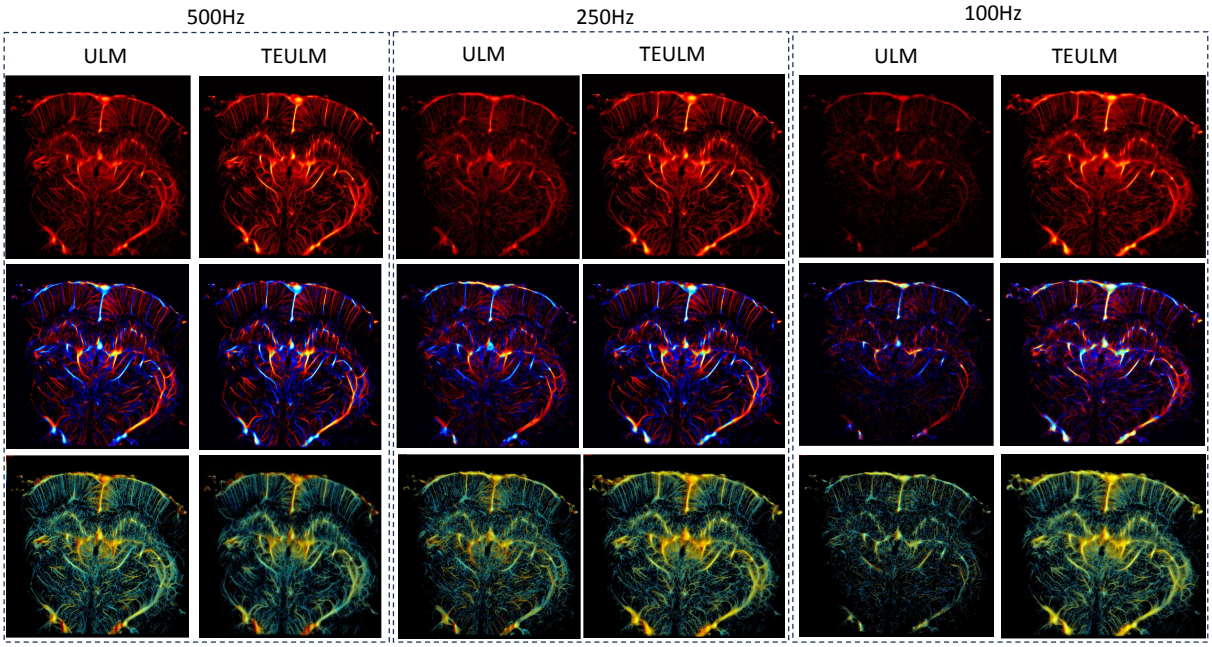

Figure 2.6: ULM- and TEULM-generated density maps (first row), flow direction map (second row), and velocity magnitude map (third row) for Dataset D at different FRs of 500Hz (DS=2), 250Hz (DS=4) and 100Hz (DS=10). The color bar of the figure is the same as original ones in Fig. 2.2.

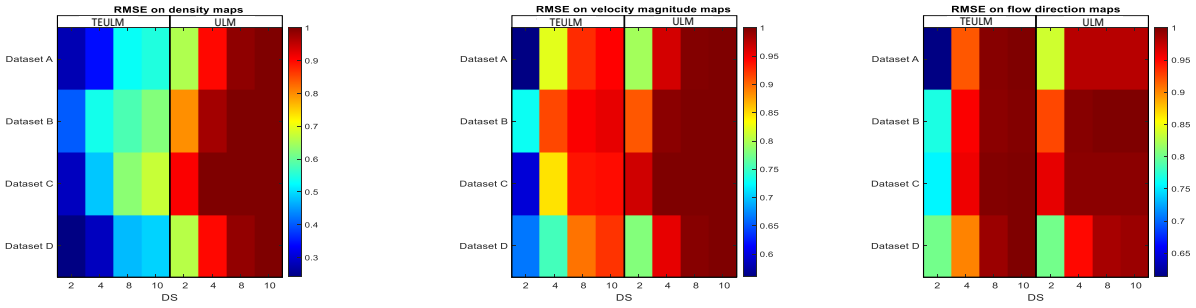

Figure 2.7: Heatmaps representing the normalized Root Mean Square Error ($RMSE$) of the reconstructed density and velocity maps at DS=2, 4, 8, 10 for TEULM and ULM for the *in vivo* datasets (A, B, C and D). The $RMSE$ is normalized with respect to the maximum value for each dataset.

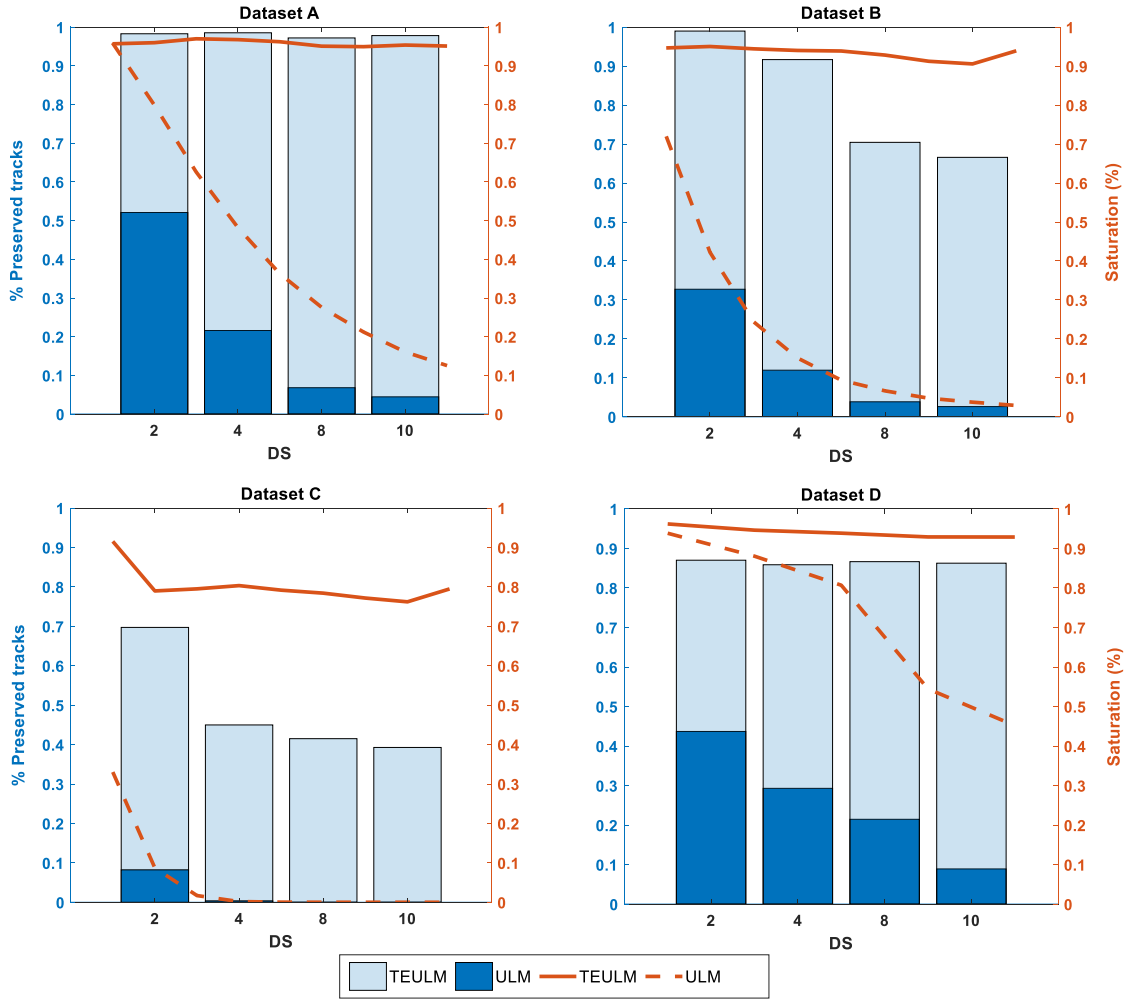

Figure 2.8: Variation of the percentage of preserved tracks (shown as bar plots) and the percentage of saturation (shown as line plot) versus the changes in DS rate (for the *in vivo* datasets). The results are normalized with respect to the tracks and the saturation of the reconstructed images using the high FR datasets, corresponding to 1KHz for Dataset A, B and D, and 500Hz for Dataset C. For dataset C, since ULM fails to recover any track for DS >7, the saturation and the number of preserved tracks in equal to 0.

2.4 Discussion

The primary goal of this study is to present an innovative approach to enable ULM at low FRs, which will facilitate ULM clinical translation. In this regard, we propose a modified ULM framework, called TEULM, that can cope with low FR data by employing the suggested 2D interpolation technique.

The proposed technique has been tested on four pre-clinical *in vivo* data (dataset A, B, C and D). For the *in vivo* datasets, we demonstrate the high efficiency of TEULM in recovering the information lost when using a low FR (Figures 2.3, 2.4, 2.5 and 2.6, for datasets A, B, C and D respectively). More specifically, while both TEULM and ULM face an image quality loss at lower FRs, as we can see in Figures 2.3, 2.4, 2.5 and 2.6, the extent of the loss varies significantly between the two techniques. In other words, the vessel's appearance for ULM degrades quickly. For instance, at a FR lower than 250Hz, the vascular structure is almost unrecognizable for all the datasets, which shows the ULM's low performance at lower FRs. In contrast, when using TEULM, the overall vascular structure remains unchanged. Besides, an increase in the DS rate results in a loss of vascular definition, manifested by more blurry areas, mostly in the fine vasculature (See an example shown in the magnified Region of Interest (ROI) in Fig. 2.4 and highlighted by the green box. This loss of definition is quantitatively assessed by the spatial resolution estimates using the FRC (Table 2.4). Despite the loss in spatial resolution, the saturation and the percentage of preserved tracks are invariant in the reconstructed images using the suggested TEULM method (see Fig. 2.8). Further, for dataset B, we observe the appearance of vascular structures in TEULM at $DS = 10$, i.e., 100Hz, (Fig. 2.4 highlighted by the yellow arrow) that are absent in the original FR, i.e., $1KHz$ (see Fig 2.2). It should be noted that, in the absence of the ground truth, it is difficult to judge whether the appearing vascular structures are artifacts or real vessels. Nevertheless, we observe that for the dataset B the global bloodstream structure in the proposed TEULM is not substantially impacted by either the loss of definition or the emergence of vascular artifacts, resulting in a $DICE$ score of 0.81 at $DS = 10$. In Table 2.5 we provided the $DICE$ score values for the *in vivo* datasets, which allows to quantitatively evaluate TEULM's performance in recovering the vessel's structure at a lower FR. The minimum $DICE$ score values (at $DS = 10$) obtained using TEULM are 79%, 81%, 68% and 82% for dataset A,B,C and D, respectively. TEULM's high $DICE$ scores show the effectiveness of the suggested technique in reconstructing the missing information. On the other hand, ULM demonstrates poor $DICE$ similarity indices (19%, 14% and 52% for dataset A, B and D respectively), which could be justified by the failure of the tracking algorithm at lower FRs. Thus, for ULM, in regions characterized by complex structures (e.g. crossing vessels or junctions) the algorithm falsely pairs MBs, resulting in unreliable vessel depiction. This assumption would also explain why dataset B and C has a much lower similarity compared to dataset A and D. It seems in fact that the vasculature of the kidney and tumor (dataset B and C) is much more tortuous and characterized by short vessels, which are easily lost at lower FRs.

The reason behind ULM's poor performance at low FRs can be attributed to the tracking algorithm, which significantly relies on the FR as it employs a frame-by-frame matching approach. In other words, with a decrease in the FR, MBs may be discarded

due to the inability to find the correct match in successive frames. Consequently, several tracks are not found or rejected because of an insufficient amount of known information, leading to a decrease in saturation and vessel definition. In fact, the number of preserved tracks in ULM for both datasets decreases exponentially as we increase the DS rate. As can be seen in Figs. 2.8, which presents the saturation curve and the percentage of recovered tracks at different FRs for datasets A, B, C and D, in comparison to the original image. Additionally, at the lower FRs, the saturation curves clearly show a decline in the ULM's capability to reconstruct the vasculature (i.e., at a DS rate of 5, the saturation on all the *in vivo* datasets decreases by more than the 50%).

TEULM, on the other hand, maintains a high percentage of recovered tracks. The value remains consistently around 1 for dataset A and approximately 0.85 for dataset D across all DS rates. However, we do notice a reduction in the percentage of preserved tracks at DS=6 for dataset B and DS=4 for dataset C. Nevertheless, TEULM's ability to preserve the number of tracks is reflected by the saturation of the density maps. The saturation levels for datasets A, B, and D remain consistently near 95%, while dataset C exhibits a saturation level of around 80%, when compared to the SR image generated using the original high FR data. The number of preserved tracks and saturation percentage indicate that datasets B and C are more challenging for TEULM. There might be a physiological reason for this. In fact, dataset B relative to the Rat Kidney and dataset C representative of the Rat Tumor are characterized by shorter and broken tracks, which are more difficult to recover when using a higher DS rates.

TEULM and ULM super-resolution density and velocity maps are further evaluated through the $RMSE$ at different $DS = 2, 4, 8, 10$ rates (shown as a heatmap in Fig. 2.7). In both TEULM and ULM, the error, which is color-coded, exhibits an upward trend as the down-sampling rate increases. When examining TEULM's density maps $RMSE$ across all the in vivo datasets, it is noteworthy that the error gradient gradually rises. Remarkably, it appears that this gradient has not yet reached a plateau. Specifically, the $RMSE$ remains below 50% for all datasets when employing TEULM, whereas it surpasses 80% when using ULM. This observation implies the potential for further increasing the DS value. In contrast, the error gradient for ULM stabilizes rapidly, particularly for dataset C (it's important to mention that ULM cannot recover any tracks with a DS greater than 6). This phenomenon underscores ULM's challenge in accurately reconstructing the morphology of vessels in a clinical setting marked by limited FR acquisition capabilities.

We investigated the efficacy of TEULM in reconstructing flow dynamics in terms of axial velocity and its magnitude. The maps of the axial velocity and velocity magnitude for the *in vivo* datasets are given in rows two and three of Figs. 2.3 (dataset A), 2.4 (dataset B), 2.5 (dataset C) and 2.6 (dataset D). The results confirm that recovering the flow dynamics is a more challenging task even when using TEULM, due to the loss of spatio-temporal information at lower FRs. At DS rates greater than 4 we observe high deviations in the flow direction information even in larger vessels. TEULM's poor performance in recovering the velocity information is further highlighted by the $RMSE$ evaluated on the velocity magnitude and flow direction maps for the *in vivo* datasets presented in Fig. 2.7. In particular, the error reaches above the 80% already at DS=4 for all the datasets when using TEULM, and above 95% when using ULM.

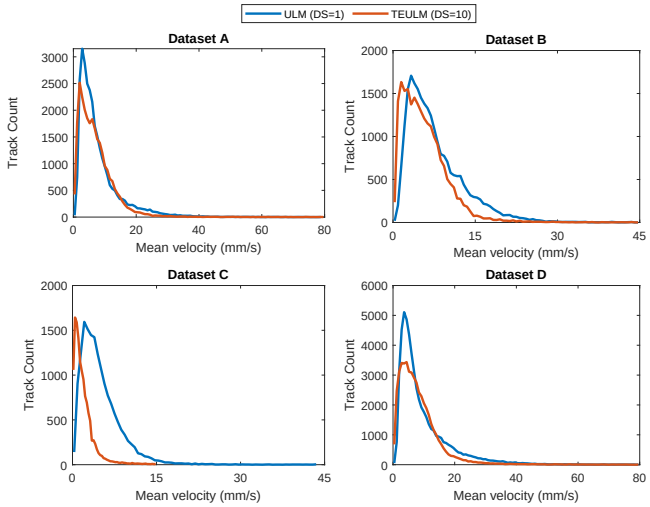

Figure 2.9: Mean velocities (mm/s) evaluated for ULM at the original FR and TEULM at down-sampling rate 10, for all the in vivo datasets.

Furthermore, TEULM misestimates the velocity magnitude, which tends to become more homogeneous as the DS rate increases for all the datasets, as seen in Figs. 2.3, 2.4, 2.5 and 2.6, for datasets A, B, C and D respectively. The loss of the magnitude information may be explained by the reduced amount of information available at lower FRs, which yields to a loss of short micro-vessels, as well as a loss of longer tracks, which become shorter. To further analyze the velocity misestimation phenomena, we evaluate the mean velocity across all the tracks within their respective datasets in Fig. 2.9). As can be seen from the figure, there is a noticeable decrease in mean velocities for the down-sampling rate of 10 for all the in vivo datasets. The results clearly indicate that accurately estimating velocities becomes a formidable challenge at lower FRs, particularly when the microbubbles are moving at high speeds. Consequently, this leads to inaccuracies in velocity estimation. Moreover, the tracking algorithms heavily rely on both spatial and temporal information to match microbubbles across frames. In our current approach, the interpolation technique utilizes spatial and temporal information along a 2D plane to reconstruct the missing frames, see Fig. 2.1. Hence, we believe that implementing a 3D interpolation technique has the potential to enhance the accuracy of velocity estimation. This approach may better capture the intricate dynamics of microbubble movement and improve the overall performance of the tracking process.

Another consideration concerns the clinical utility of TEULM. The proposed TEULM represents a step towards transitioning ULM into clinical practice, addressing the current constraint of high FR requirements. However, despite the striking similarity in global information between the SR images reconstructed at DS=10 using TEULM and those obtained through high FR ULM, we observe a substantial loss in the definition of vessels, particularly in the intricate microvascular structure. This loss may adversely affect both the quantity and quality of clinical information within the SR images. Furthermore, we note a marked decline in the retrieval of dynamic information at DS values exceeding

4, which imposes a limitation on TEULM's applicability in clinical scenarios. Therefore, if these SR images are to be used in a clinical context, we assert the need for further enhancements in the representation of vessels within the microvasculature and in the recovery of dynamic information at sub-100Hz FRs before considering the extension of utilization with higher DS factors.

There are some limitations that are not explored in the study. First, in this paper, we only tested TEULM on 2D datasets. As future work, we envision extending the proposed approach to a 3D dataset, since 3D TEULM would represent an additional and fundamental step towards facilitating the clinical translation of this technology.

Second, the impact of motion on TEULM performance has not been explored in this paper. However, motion may lead to errors in reconstructing the signal path and target localization when using higher DS rates. Therefore, addressing motion effects through the implementation of motion compensation techniques could be explored as a potential avenue for future research. In addition, we aim at implementing a 3D interpolation technique. We anticipate that this approach will enhance the performance of TEULM in capturing dynamic profiles, even at lower FRs.

2.5 Conclusion

This study presents TEULM, a technique to alleviate the high FR data acquisition (in the range of 1kHz), generally necessary to frame-to-frame pair the microbubbles in the ULM framework. Relaxing such constraint would promote the ULM clinical transition, as the US systems used in hospital can reach a FR of a magnitude lower. Results show that TEULM allows the generation of SR density maps with data acquired at FRs as low as 50 Hz (an order of magnitude lower than the standard ULM). On the other hand, even if still capable to relax the FR by factor 4, TEULM required slightly higher FRs (250 Hz) for the generation of consistent velocity maps with respect to the high FR's generated maps.

Chapter 3

A Novel 2x2D Radial Basis Functions-based Interpolation for Short Acquisition Time and Relaxed FR Ultrasound Localization Microscopy

This Chapter[2] *addresses one major challenge is the high frame rates (FR) and lengthy acquisition time needed to produce Ultrasound Localization Microscopy (ULM) images. To overcome this, our goal is to relax the FR and shorten this acquisition time while preserving ULM image quality, thereby enhancing ULM's clinical applicability. To this end, we propose two distinct strategies: first, we suggest acquiring the data at lower FR followed by applying the reconstruction technique to compensate the lost information due to the low FR imaging. Secondly, to tackle the prolonged acquisition time, we propose compressing acquisition time by a compression ratio (CR), which can degrade ULM image quality due to reduced temporal information. To mitigate this, we temporally upsample the in-phase-quadrature (IQ) data by a factor equal to the CR after the compressed acquisition. Additionally, we introduce a novel 2x2D interpolation using radial basis function (RBF)-based reconstruction to estimate unknown values in the 3D IQ data (x-z-t), thereby enhancing temporal resolution. This bi-directional approach improves the reconstruction of microbubbles' dynamics by interpolating along both x and z directions. The method was tested on rat brain and ratkidney datasets recorded at 1kHz, demonstrating relaxing the FR to 100 Hz (using the first strategy) and a reduction in acquisition time by a factor of 3 to 4 (using the second strategy) while maintaining ULM image quality comparable to the original uncompressed data, including density and velocity maps.*

[2]This Chapter appears in:
[J1] Afrakhteh S., Tuccio G., Demi L., "A Novel 2x2D Radial Basis Functions-based Interpolation for Short Acquisition Time and Relaxed FR Ultrasound Localization Microscopy" In IEEE transactions on ultrasonics ferroelectric and frequency control, 2024

3.1 Introduction

The adoption of ULM in clinical practice faces several challenges that require ongoing research and innovation. The key challenges lie in prolonged data acquisition times, low FR scanners, restricted clinical doses of contrast microbubbles, and difficulties in accurately localizing and tracking microbubbles due to ultrasound noise and phase aberrations.

Over the past decade, the ULM framework has seen significant growth, with numerous signal processing and machine learning technologies developed to enhance its performance. The fundamental principle of ULM involves pinpointing the center positions of microbubbles and tracking their movement to determine blood flow properties. When the signal-to-noise ratio (SNR) of the microbubble signal is low, distinguishing the isolated microbubble signal from ultrasound noise becomes difficult due to high levels of noise from factors like ultrasound attenuation, thermal noise, and residual tissue clutter, which results in error in tracking and consequently unreliable localization. Song et al. [93] introduced non-local mean (NLM) filtering to maintain microbubble tracks created by microbubble movement while reducing random background noise. They then employed bipartite graph-based pairing for tracking. When applied to a rabbit's kidney, their technique effectively suppressed background noise, leading to improved localization of microbubbles. In [94], the authors proposed a technique utilizing randomized SVD (rSVD) to efficiently reject tissue clutter with low computational complexity. They implemented a noise suppression version on a Verasonics ultrasound scanner, demonstrating its effectiveness at FRs exceeding 25 Hz. Additionally, techniques based on sparse image reconstruction combined with compressed sensing have been proposed for localization and super-resolution, leveraging the assumption that microbubbles are sparsely distributed in each imaging frame [95, 96]. However, the effectiveness of these approaches is limited to areas with high microbubble concentrations.

Differently, in [97], the authors proposed an approach for reducing the acquisition time based on separating spatially overlapping microbubble events into sub-populations utilizing the spatiotemporal differences in flow speeds and directions. Microbubble localization and tracking were then conducted for each sub-population individually, allowing for more robust ULM imaging even with high-concentration microbubble injections. In [98, 99], we proposed acquiring data at lower FRs and then applying temporal interpolation to achieve high-performance microbubble localization. The interpolation approach used in the study involved interpolating 2D spatiotemporal information along the depth. The results demonstrated that the FR could be relaxed by a factor of 10 based on density maps. However, when considering dynamic maps (velocity magnitude and direction), the feasible relaxation rate was determined to be 4.

In this study, we introduce an advanced ULM framework utilizing a bi-directional interpolation technique based on RBF. The performance of the RBF interpolator relies on the distance between data points; therefore, by integrating spatiotemporal information along both the x-t and z-t directions, this technique effectively compensates for information loss encountered when using a clinical scanner to acquire ultrasound data. Moreover, we propose utilizing the approach to address two distinct challenges in ULM including the high FR and prolonged acquisition time needed for precise localization. Therefore, the main contributions of the papers lies in the following:

- We present the new development of the previously designed 2D-RBF interpolation technique in [98], which is called bi-directional 2D RBF Interpolation (i.e., 2x2D RBF Interpolation). In ULM, accurately tracking microbubble positions over time is critical for super-resolution imaging. Microbubbles move within the vasculature, creating complex spatio-temporal signals that can be difficult to capture with single-plane interpolation due to anisotropies and non-uniformities in their motion and distribution. The main hypothesis behind the 2x2D bi-directional interpolation strategy is that integrating interpolation results from two orthogonal spatio-temporal planes (x-t and z-t) provides a more accurate and robust reconstruction of microbubble trajectories.

- Moreover, we design two different sparse coding strategies to test the proposed 2x2D bi-directional interpolation strategy. Firstly, for relaxing the need for a very high FR (in kHz range) and successively, for decreasing the prolonged acquisition time.

The rest of the paper is structured as follows: In Section 3.2, we outline the proposed technique designed to reduce the FR and acquisition time requirements for ULM. Section 3.3 presents the results and discussion of applying this technique to ULM followed by discussing and analysing the results in Section 3.4. Finally, the paper's conclusions are provided in Section 3.5.

3.2 Materials and Methods

3.2.1 Proposed RBF-based 2x2D Interpolation

2D RBF-based Interpolation

Radial basis function (RBF) interpolation is a powerful technique for interpolating multi-dimensional sparse data. The interpolation function $f(\mathbf{x})$ is expressed as a weighted sum of radial basis functions centered at the known data points:

$$f(\mathbf{x}) = \sum_{i=1}^{N} \lambda_i \phi(r_i) = \sum_{i=1}^{N} \lambda_i \phi\left(\|\mathbf{x} - \mathbf{x}_i\|\right), \tag{3.1}$$

where $f(\mathbf{x})$ is the interpolated function at unknown value point $\mathbf{x}$, $\mathbf{x}_i$ are the known value points, λ_i are the coefficients to be determined, ϕ is the radial basis function, M is the number of all points in the 2D grid, and $r_i = \|\mathbf{x} - \mathbf{x}_i\|$ denotes the Euclidean distance between $\mathbf{x}$ and $\mathbf{x}_i$. It should be noted that we use the Multiquadric (MQ) function (i.e., $\phi(r) = \sqrt{1 + (\epsilon r)^2}$) as the RBF basis because of its better smoothness property and the convergence speed, which makes the interpolation faster. In this function, ϵ is a constant and r is the radius of the RBF [86, 100]. The RBF-based interpolation process involves two essential steps. First, a model is constructed by evaluating the RBF function at known data points (determining the $\mathbf{\Lambda}$). Therefore, the interpolation task is to determine the λ_i for each data point, i.e., solving the linear system $\mathbf{\Phi}_{N\times N}\mathbf{\Lambda}_{N\times 1} = \mathbf{F}_{N\times 1}$, which can

be expanded as follows:

$$\underbrace{\begin{bmatrix} \phi(r_{1,1}) & \phi(r_{1,2}) & \dots & \phi(r_{1,N}) \\ \phi(r_{2,1}) & \phi(r_{2,2}) & \dots & \phi(r_{2,N}) \\ \vdots & \vdots & \ddots & \vdots \\ \phi(r_{N-1,1}) & \phi(r_{N-1,2}) & \dots & \phi(r_{N-1,N}) \\ \phi(r_{N,1}) & \phi(r_{N,2}) & \dots & \phi(r_{N,N}) \end{bmatrix}}_{\mathbf{\Phi}} \underbrace{\begin{bmatrix} \lambda_1 \\ \lambda_2 \\ \vdots \\ \lambda_{N-1} \\ \lambda_N \end{bmatrix}}_{\mathbf{\Lambda}} = \underbrace{\begin{bmatrix} f(\mathbf{X}_1) \\ f(\mathbf{X}_2) \\ \vdots \\ f(\mathbf{X}_{N-1}) \\ f(\mathbf{X}_N) \end{bmatrix}}_{\mathbf{F}}, \tag{3.2}$$

In the second step, this model is used to reconstruct the missing values in the incomplete dataset. Since for the known data points the values ($\mathbf{F}$) and their distances (r) are known, we can simply use $\mathbf{\Lambda} = \mathbf{\Phi}^{-1}\mathbf{F}$ to determine the $\mathbf{\Lambda}$ at N data points. Now, the interpolation model is created and it can be used in the utilization step to reconstruct the unknown values. To estimate the unknown values at M data points, where their values are not available, a new evaluation matrix, Φ_{new}, needs to be constructed. This matrix is formed based on the distances between these M points and the known N points. Using this newly constructed evaluation matrix and the weight vector derived from the known data points (as described in Eq. (3.2)), the missing values at the M points (i.e., $[\mathbf{F_{rec}}]_{\mathbf{M\times 1}}$) can be estimated according to Eq. (3.3)):

$$\mathbf{F_{rec_{M\times 1}}} = \mathbf{\Phi_{newM\times N}}\mathbf{\Lambda}_{N\times 1}, \tag{3.3}$$

which can be expanded as follows:

$$\underbrace{\begin{bmatrix} f_{rec}(\mathbf{X}_1) \\ f_{rec}(\mathbf{X}_2) \\ \vdots \\ f_{rec}(\mathbf{X}_{M-1}) \\ f_{rec}(\mathbf{X}_M) \end{bmatrix}}_{\mathbf{F_{rec}}} = \underbrace{\begin{bmatrix} \phi(r_{1,1}) & \phi(r_{1,2}) & \dots & \phi(r_{1,N}) \\ \phi(r_{2,1}) & \phi(r_{2,2}) & \dots & \phi(r_{2,N}) \\ \vdots & \vdots & \ddots & \vdots \\ \phi(r_{M-1,1}) & \phi(r_{M-1,2}) & \dots & \phi(r_{M-1,N}) \\ \phi(r_{M,1}) & \phi(r_{M,2}) & \dots & \phi(r_{M,N}) \end{bmatrix}}_{\mathbf{\Phi_{new}}} \underbrace{\begin{bmatrix} w_1 \\ w_2 \\ \vdots \\ w_{N-1} \\ w_N \end{bmatrix}}_{\mathbf{\Lambda}}, \tag{3.4}$$

where $\mathbf{F_{rec}}$ includes the reconstructed values at M ($M > N$) data points in the 2D grid.

RBF interpolation presents scalability and numerical instability issues, especially with large datasets. The MQ function has a shape parameter that can be adjusted for different datasets. Specifically, instability issues arise when the shape parameter is set to small values (as indicated by the condition number). By selecting a sufficiently large shape parameter (i.e., in this study $\epsilon > 10^4$), we were able to reduce the instability issue in RBF interpolation, resulting in a well-posed problem.

bi-directional Interpolation Strategy (2x2D)

The 2x2D strategy uses RBF interpolation in two separate planes, $x - t$ and $z - t$, and then combines the results. The main hypothesis behind the 2x2D bi-directional interpolation strategy is that combining interpolation results from two orthogonal spatio-temporal planes ($x - t$ and $z - t$) enhances the accuracy and robustness of reconstructing a 2D spatio-temporal structure. By leveraging information from both directions, this method can capture complex dependencies and variations in the data that might be missed when using a single interpolation plane. This bi-directional approach aims to reduce interpolation errors and improve the overall quality of the reconstructed data by integrating complementary perspectives from the $x - t$ and $z - t$ planes. After performing the RBF

interpolation in both the $x-t$ and $z-t$ planes, the next step is to combine these results to obtain the final interpolated data:

$$\mathbf{F_{rec}} = w_{x-t} \times \mathbf{F_{rec}}^{<x-t>} + w_{z-t} \times \mathbf{F_{rec}}^{<z-t>}, \tag{3.5}$$

where w_{x-t} and w_{z-t} are the weights assigned to each direction's interpolation. In this study, to ensure a balanced combination, we set $w_{x-t} = w_{z-t}$, as we did not have any prior knowledge about the relative importance of the two directions.

To minimize errors and biases in combining the results of the RBF interpolation across two planes, several precautions are essential. In particular, the size of the kernel along the time domain should be the same for each block in the same dataset to prevent any bias. Matrix conditioning is also important for numerical stability, particularly in large systems of equations related to 3D data. An appropriate shape parameter for the RBF basis function helps maintain stability and reduce numerical instability, facilitating a reliable integration of results from both planes. This linear combination of orthogonal planes enhances data representation by effectively integrating complementary information. For example, estimating velocities in two orthogonal planes is equivalent to evaluating two velocity components of the velocity vector in two orthogonal planes. Thus, the final velocity map consists of the sum of the results of the interpolations along the two orthogonal planes. Without prior knowledge of the flow information, the density map is the average of the results of the interpolations along the two orthogonal planes to reduce the unnecessary errors.

3.2.2 Proposed strategies for relaxing the requirements for ULM

Strategy 1 (Relaxing the Requirement for FR)

One of the main parameters that limit the real-time application of ULM in clinical settings is the FR. The FR in ULM is crucial for accurately tracking microbubbles and measuring flow velocity. Higher FRs capture fast-moving particles more effectively, providing detailed images of the microvasculature and reducing motion artifacts and blurring. This improves the precision of microbubble localization, leading to more accurate reconstructions of vascular structures and flow patterns. Consequently, an optimal FR is essential for high-quality imaging and reliable data acquisition in both clinical and research applications. For high-precision ULM, the feasible FR is typically in the range of kHz, achievable with ultrafast ultrasound imaging [32, 100, 101]. However, this FR is often beyond the capability of clinical scanners. To address this issue and mitigate the trade-off between super-resolved image quality and FR, we propose acquiring data at a lower FR followed by applying the suggested 2x2D interpolation (see Section 3.2.1). This approach compensates for the temporal connectivity, reconstructing the temporal information to enhance microbubble tracking. More specifically, our first strategy to relax the high FR requirement in ULM involves the following steps:

Step 1: Acquire data at a lower FR (FR'), which is closer to the FR typically available in clinical settings.

Step 2: Beamform the low FR data using the delay and sum (DAS) technique. At this step, we obtain the beamformed in-phase and quadrature (IQ) or radio frequency

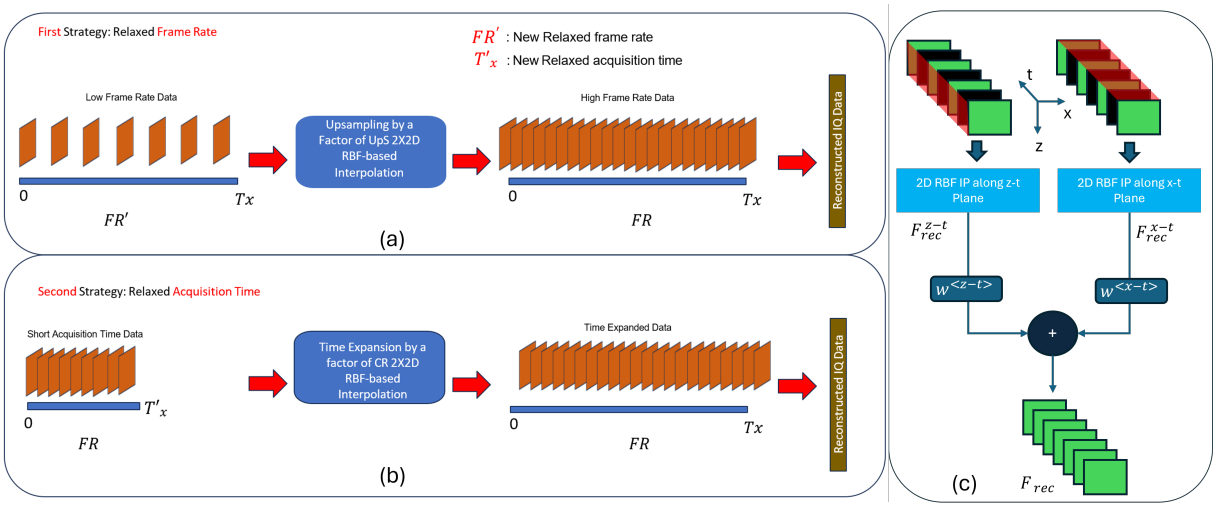

Figure 3.1: The block diagram of the proposed approach for applying the 2x2D RBF-based interpolation to reduce FR requirements and acquisition time. (a) The first strategy focuses on relaxing the high FR demands by recording data at lower FR (FR') followed by applying the interpolation to compensate for low FR data, i.e., the FR will be synthetically increased from FR' to FR depending on the upsampling factor UpS ($FR = FR' \times UpS$). (b) The second strategy targets shortening the acquisition time from T_x to T'_x with a compression ratio (CR), where $T'_x = T_x/CR$. In both strategies, the 2x2D RBF-based interpolation technique, depicted in (c), is employed to reconstruct IQ data, enhancing FRs in the first strategy and extending acquisition times in the second. In (c), the black image frames represent frames are missing, while the green image frames indicate frames where data is available.

(RF) data necessary for ULM. However, the number of frames available for each recording might be insufficient for high-performance tracking due to the loss of temporal information from low FR acquisition.

Step 3: Upsample the recorded video by a factor of UpS (i.e., insert $UpS - 1$ frames with NaN values between the successive frames in the 3D beamformed IQ or RF data).

Step 4: Reconstruct the missing values marked with NaN in the 3D structured beamformed data using the suggested 2x2D RBF interpolation.

The proposed technique improves information retrieval in the temporal direction (resulting in # of frames $= UpS \times FR'$), while acquiring data at a low FR (FR').
The strategy is also summarized in the first row of Fig. 3.1. To test this approach, we simulate a low FR data acquisition by down-sampling of a factor $DS = \frac{1}{UpS}$ data acquired at high FRs.

Strategy 2 (Relaxing the Requirement for Acquisition Time)

In ULM, the sufficient length of acquisition time (T_x) is crucial for achieving high spatial resolution and precise localization of microbubbles within the bloodstream, which

enhances the overall image quality and accuracy of the microvasculature maps. Long acquisition times are needed to ensure sparse microbubbles signals for precise localization, as well as the transit of the microbubbles in the region of interest. However, the prolonged acquisition times must be balanced against potential motion artifacts, increased computational load, and patient comfort in clinical settings. Thus, shortening acquisition time is essential to ensure detailed and reliable imaging while maintaining practical and comfortable procedures for patients. In this paper, we propose compressing the acquisition time by a factor of a compression ratio (CR), i.e., $T'_x = \frac{T_x}{CR}$, followed by applying the proposed 2x2D RBF interpolation to compensate for the spatial resolution and quality of microvasculature maps. The strategy is also summarized in the second row of Fig. 3.1.

3.2.3 Standard ULM

After modifying the FR or acquisition time of the recorded data using the proposed strategies 1 and 2, respectively, we proceed with the standard ULM framework to obtain super-resolved images. The steps in the ULM framework include k-SVD filtering, microbubble detection and localization, tracking, and finally accumulating the tracks to generate the vasculature map:

k-SVD Filtering

The k-SVD leverages the fact that backscattered signals from tissue exhibit higher spatio-temporal coherence compared to microbubble echoes. By removing the first k singular values, the tissue signal is effectively filtered out from the data [102].

Microbubble Detection and Localization

At this stage, pixels with maximum intensity values are identified as microbubbles, and their localization is achieved using a Gaussian fitting algorithm [103].

Microbubble Tracking

For tracking, we employ the modified Kuhn-Munkres bipartite algorithm [103]. The core assumption of this method is that each MB in one frame should be paired with an MB in the subsequent frame based on their relative distance. In the standard approach, the algorithm requires all MBs to be paired, but this can be suboptimal due to the unpredictable behavior of contrast agents, such as the disappearance of MBs. To address this, as outlined in [93], we adopted a modified version of the Hungarian algorithm. This approach allows for partial assignments, meaning that MB pairing occurs only when the pairing distance is mutually minimal. If an MB cannot find a valid match after exploring all potential assignment options, it is discarded in the next frame. Moreover, to improve the robustness of the tracking algorithm, we set a threshold for the maximum linking distance to pair MBs, i.e., MBs further than the threshold can not be paired and a threshold for the minimum track length, i.e., tracks with lengths less than the threshold are considered noise.

Table 3.1: ULM Parameters used in this work.

Dataset	Frame Rate (Hz)	k-value (SVD)	Max. Linking Distance (pixel)	Min. Track Length	Number of MB/frame
In silico	500	-	3	10	40
Rat Brain	1000	5	2	15	70
Rat Kidney	1000	10	1.5	15	100

Accumulating the tracks

Finally, a vasculature intensity map is generated by accumulating the microbubble tracks, which have been previously smoothed and interpolated to fill in any missing points, across all frames. Finally, from the positions it is possible to derive the functional information (velocity magnitude and flow direction). The functional maps are color-coded. In particular, the colorbar of the flow direction maps encodes the flow towards (blue) and against (red) the probe, whereas the colorbar of the velocity magnitude encodes the flow velocity in mm/s.

3.2.4 Datasets

To evaluate the proposed strategy, we utilized three datasets benchmarked in [103]. In particular, we selected one in silico dataset and two in vivo datasets: rat brain and rat kidney data. The in vivo datasets were recorded with a 15 MHz center frequency probe (Vermon, France). While the in silico dataset provides a ground truth and consequently, the opportunity to evaluate the performance of the proposed technique, the in vivo datasets cover a broad spectrum of hemodynamic structures across different organs (such as the brain and kidney) and various injection methods. Table 3.1, presents the ULM parameters, which are dataset-dependent. Although clutter filtering can be significantly affected by the FR, we set the k-value of the SVD filter to the same value used with high FR data [30]. The choice comes after performing a study on the impact of the k-value of the SVD filter on the performance of the interpolation technique at different FRs on two publicly available datasets [30], rat brain and rat kidney. In particular, we performed a parametrisation study, in which we varied the k-value from its original value at the original high FRs (5 for the Rat Brain and 10 for the Rat Kidney dataset) by -50%, +50%, 100% and 150%. Finally, the density maps are rebuilt for each of these variations. Rat brain and the rat kidney datasets were used for these analysis. Then, results considering resolution (FRC) and Dice Score at 100 Hz are presented in Table 3.2. The results show that at 100 Hz the k-value does not impact the Dice Score for both datasets. Furthermore, while the resolution for the Rat Brain dataset remains the same when varying the k-value, the resolution sensibly worsens for the Rat Kidney dataset. In particular, the resolution in μm increases with increasing k-value. Although optimizing the k-value of the clutter filter might improve some of the metrics (e.g. FRC), it does not impact others (e.g. Dice Score). While parameter optimization might be useful to improve the selection of the k-value, we have decided to keep its value constant in this comparative study among different interpolation techniques.

Table 3.2: Resolution and Dice Score for the Rat Brain and Kidney datasets while varying the k-value of the SVD filter after applying the interpolation to data acquired at 100 Hz. Original value of FRC is shown in brackets for comparison.

	Rat Brain	**Rat Kidney**
FRC (μm)	17.9 ± 3.6 (11.49)	52.7 ± 21.2 (26.3)
Dice Score	78.9 ± 0.02	80 ± 0.05

3.2.5 Evaluation Metrics

Tracking Precision and Recall

To evaluate the validity of the tracks generated after applying the proposed technique, we assess the tracking performance utilizing an *in silico* dataset [103]. By providing the tracks' ground truth, the dataset allows computing the True Positives (TP), False Positives (FP) and False Negatives (FN). In particular, a MB assigned to the same track ID is considered as a true positive (TP); a MB assigned to a different ID is a false negative (FN) and two MBs assigned to the same track ID are false positives (FP). Then, the tracking performance is evaluated through precision and recall as follows:

$$Precision = \frac{TP}{FP + TP}, Recall = \frac{TP}{FN + TP}. \tag{3.6}$$

We only keep the true positive detections to evaluate the tracking performance independently from the detection's performance. The *Precision* represents the validity of the generated tracks, whereas the *Recall* represents the fraction of tracks recovered by the technique among all the tracks in the original dataset. We evaluate the tracking performance for both strategies.

Fourier Ring Correlation (FRC)

A frequently utilized metric for evaluating the quality of super-resolved images is the frequency ring correlation (FRC) [104]. This metric assesses the correlation of spatial frequencies along spatial frequency rings (r_i) between two sub-images in the frequency domain with the frequency band $[F_1, F_2]$, which are created by randomly dividing the tracks in two subsets. In particular, the FRC is computed as follows. First, we split the tracks forming the micro-resolved ULM image in two subsets. For each of the two subsets, we generate the density maps and then compute the Fourier transform for each of the two images F_1 and F_2.Next, we compute the norm of the wave vector for all the points in the Fourier domain, which represents the frequency distribution (r). The size of the frequency domain corresponds to the super-resolution image size. Here, it is equivalent to ten times the ultrasound image size. Finally, we compute the correlation between the images along iso-frequency rings $r_i = 1/L, 2/L, ...$, where L is the pixel size in Fourier space. Thus, the FRC is calculated as follows:

$$FRC(r_i) = \frac{\sum_{r \in r_i} F_1(r) F_2(r)^*}{\sqrt{\sum_{r \in r_i} |F_1(r)|^2 \sum_{r \in r_i} |F_2(r)|^2}}. \tag{3.7}$$

The resolution value is determined by the inverse value of the FRC curve at the point where the FRC falls below a specific threshold. In our study, we use the 1/2 bit thresholding method, which corresponds to the highest spatial frequency required to gather sufficient information to fill half a bit.

DICE Similarity Index

The $DICE$ score assesses the similarity between two images by quantifying the intersection area of the two images relative to the total area of their combined regions.

$$DICE = \frac{2 \times |I_{DS} \cap I_1|}{|I_{DS}| \cup |I_1|}, \tag{3.8}$$

where, in the relaxed FR strategy, I_{DS} denotes the reconstructed image at a reduced FR, and in the relaxed acquisition time strategy, it represents the image reconstructed with a decreased acquisition time. Similarly, I_1 refers to the reconstructed image at the original FR (in the relaxed FR strategy) or the total acquisition time (in the relaxed acquisition time strategy). The Dice score is without units.

Root Mean Square Error (RMSE)

Another parameter employed to assess the quality of the reconstructed image (I_{DS}) under conditions of either reduced FR or short acquisition time involves comparing it with the reference image (I_1) at either the original FR or the original acquisition time. The formulation for $RMSE$ can be expressed as follows:

$$RMSE = \sqrt{\sum_{i=1}^{N_{pix}} \frac{\left(|I_{DS} - I_1|\right)^2}{N_{pix}}}, \tag{3.9}$$

with N_{pix} total number of pixels in the reconstructed density map. The RMSE unit of measure is the pixels' intensity.

3.3 Results

The paper introduces a novel technique based on two strategies aimed at reducing the high FR and high acquisition time requirements in ULM imaging. To achieve this, we implemented two different sparse coding approaches to lower FR and acquisition time needs, followed by a novel 2x2D RBF-based interpolation to compensate for the temporal information. In the following, we present the results of applying the proposed technique to datasets from a rat's brain and kidney.

To evaluate the performance of our proposed technique under the relaxed FR strategy, we follow this procedure: the original FR serves as the reference for high FR imaging, with super-resolved images at 1 KHz considered the reference images. To model the proposed low FR strategy, we temporally down-sample the acquired frames and apply the ULM framework to obtain the results, referred to as low FR ULM. In this study, a

down-sampling factor of 10 is used to remove temporal frames, resulting in a FR of 100 Hz, which is closer to clinical settings. Finally, we apply the proposed 2x2D interpolation technique to the IQ data acquired at the lower FR to reconstruct the missing temporal information. Density maps are shown for the relaxed FR strategy in Fig. 3.2 and 3.3 for the in-silico and rat brain datasets respectively. For the in-vivo dataset, this strategy represents an advancement of our previous approach detailed in [98] and it is used as a reference for comparison.

Given that some microvascular structures exhibit pronounced directional blood flow, such as predominantly vertical flow (i.e. in the cerebral cortex), we conduct comparative studies on interpolation methods based on individual planes (x-t, z-t) and their combination (2x2D interpolation). Furthermore, to justify the use of RBF-interpolators over a standard interpolation technique, we compare it with standard linear interpolation (LinIP) and provide quantitative and qualitative results. Results are provided for the rat brain dataset at 100 Hz in Figure 3.3 and Table 3.3.

To evaluate the performance of the proposed technique in a short acquisition time scenario, we considered the first K frames based on the compression ratio (CR), where $K = \frac{Num_{frames}}{CR}$. We then interpolated $CR-1$ middle frames between the successive frames to enhance the reconstruction quality of the super-resolved image. Here, the original long acquisition time ($T'_x = T_x$) serves as the reference for comparison and reference-based evaluation metrics calculations. This strategy was applied to the in-silico dataset, rat's brain and kidney datasets. The results are presented in Fig. 3.2, Fig. 3.4 and Fig. 3.5 for the in-silico, rat's brain and kidney datasets, respectively.

To obtain quantitative results, we extracted the evaluation metrics discussed in Section 3.2.5. These metrics provide insight into the improvement level achieved by using the proposed low FR and short acquisition times techniques, enhanced by the 2x2D interpolation technique. In particular, the in-silico dataset offers the opportunity to evaluate the precision and recall after tracking the MBs. Tracking precision and recall are presented for both strategies in Table 3.4. Furthermore, for the in-vivo datasets, we evaluate the performance of the interpolation considering FRC, RMSE, and DICE similarity score. The results are presented in Table 3.3 for the Relaxed FR strategy, and are reported in Table 3.5 and Table 3.6 for the reduced acquisition times for the rat's brain and kidney datasets, respectively.

Finally, we evaluate the performance of the bi-directional interpolation in recovering velocity information for the relaxed FR strategy (Fig 3.7).
In particular, we compute the mean velocity profiles for the Rat Brain dataset at 100 Hz when using the bi-directional interpolation to up-sample the data, and provide the comparison with the velocity distribution of the original high FR data and TEULM at 100 Hz.

Results are produced for FRs 100 Hz for the relaxed FR strategy and at 1/4 acquisition time for the relaxed acquisition time strategy.
These results confirm the improvement in the tracking with respect to not applying the interpolation technique for both strategies. While the quality of the detected tracks is above 70% for both strategies, the percentage of tracks is low, especially for the relaxed FR strategy at down-sampling 10.

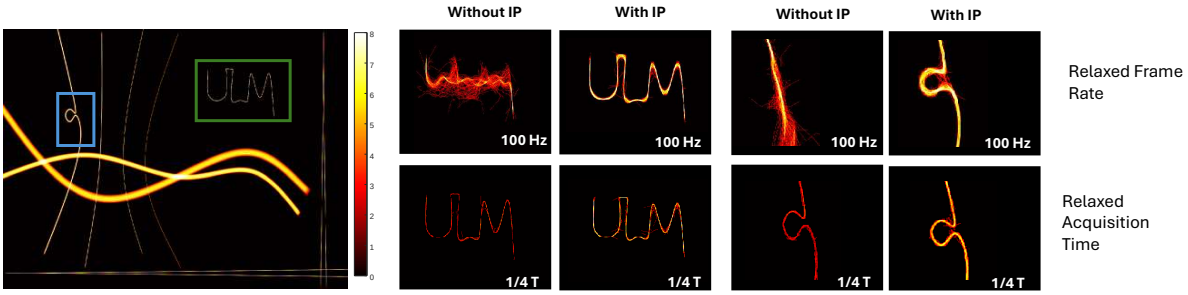

Figure 3.2: Density maps of the in-silico dataset when applying the proposed techniques: Relaxed FR at 100 Hz and Relaxed Acquisition Time at 1/4 of the original acquisition time. Density maps are presented for two regions of interest (ROIs) without the interpolation (Without IP) and when applying the interpolation technique (With IP).

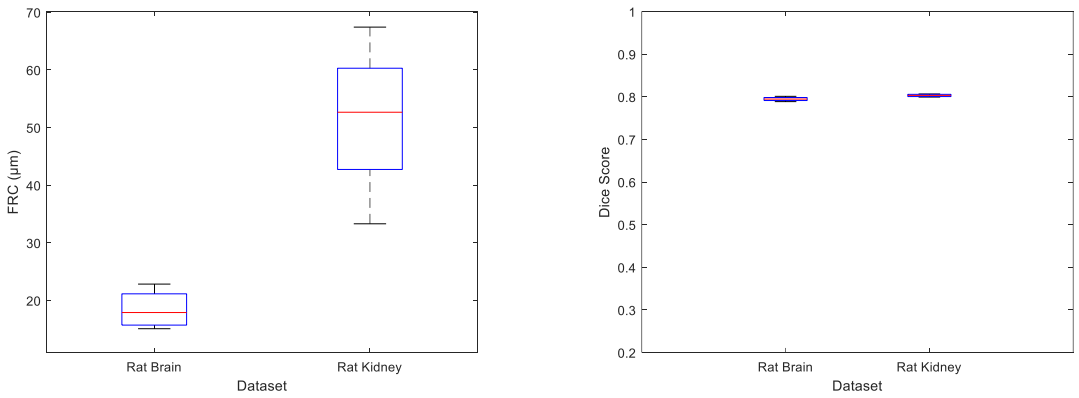

Figure 3.3: Results of the proposed technique (last column) when applying the interpolation technique to rat brain dataset at 100Hz in comparison to the original FR ULM at 1 KHz (first column). The second column show the super-resolved images derived at 100 Hz FR without applying interpolation. The third, fourth, and fifth columns show the super-resolved images after applying interpolation using RBF along z-t, RBF along x-t (noted as TEULM), and LinIP, respectively. The first, second, and third rows represent the density, flow direction, and velocity magnitude maps for each case, respectively.

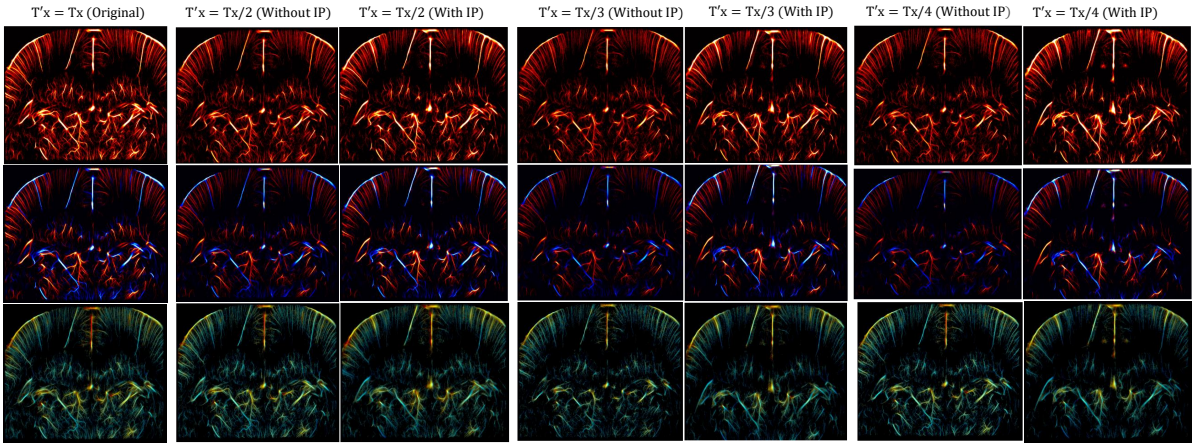

Figure 3.4: The results of the suggested technique for the relaxed acquisition time strategy when applying to the rat brain data. The first column displays the results for the scenario where the total acquisition time is used ($T'_x = T_x$). The second and third columns show the outcomes when using half of the original total acquisition time, with and without applying the suggested 2x2D interpolation (IP) based on the relaxed acquisition time strategy ($T'_x = T_x/2$), respectively. Similarly, the fourth and fifth columns show the results for $T'_x = T_x/3$ with and without applying the proposed 2x2D IP, respectively. Differently, the first, second, and third columns represent the density, flow direction, and velocity magnitude maps for each case, respectively.

Table 3.3: The quantitative results without the interpolation and with interpolation along different planes and utilizing a linear interpolation to the rat brain data.

Methods	FRC (μm)	RMSE	DICE
ULM (1 KHz)	11.5	-	-
ULM (100 Hz)	22	0.9	0.19
z-t (100 Hz)	18.9	0.87	0.55
TEULM (x-t [98]) (100 Hz)	17.8	0.85	0.79
Linear Interpolation (100 Hz)	20.7	0.71	0.62
Proposed (x-t and z-t) (100 Hz)	19	0.67	0.82

3.4 Discussion

Fig. 3.3 shows the results of the evaluation of the relaxed FR strategy when applied to the Rat's brain data. The figure depicts a comparative analysis of various imaging techniques across different levels: density maps (first row), velocity direction (second row), and velocity magnitude (third row). The ULM at 1 kHz FR consistently displays the highest detail and clarity due to its superior spatial resolution. Conversely, the ULM at 100 Hz FR exhibits significant loss in detail, with blurred and less defined structures. This is because of the loss of the information along the temporal dimension due to the down-sampling. The TEULM at 100 Hz, which combines ULM with interpolation in the $x-t$ plane, improves clarity, resolution, and detail over the standard ULM at the same frequency. Remarkably, the proposed method at 100 Hz, which employs 2x2D interpolation in both $x-t$ and $z-t$

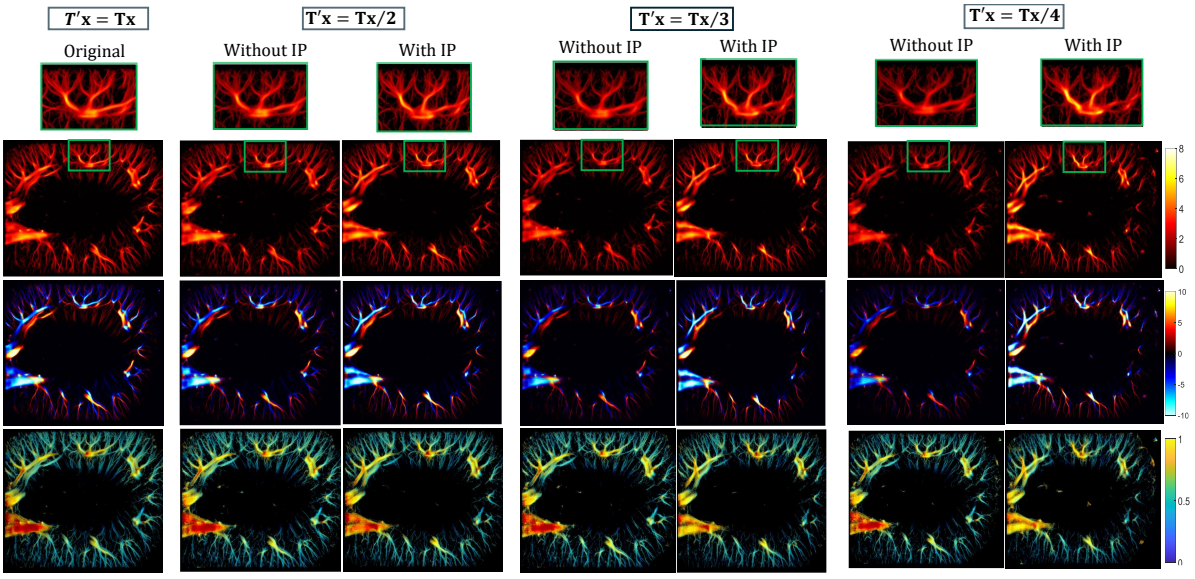

Figure 3.5: The results of applying the proposed technique (relaxed acquisition time strategy) to the rat kidney data. The first column displays the results for the scenario where the total acquisition time is used ($T'_x = T_x$). The second and third columns show the outcomes when using half of the original total acquisition time, with and without applying the suggested 2x2D interpolation (IP) based on the relaxed acquisition time strategy ($T'_x = T_x/2$), respectively. Similarly, the fourth and fifth columns show the results for $T'_x = T_x/3$ with and without applying the proposed 2x2D IP, respectively. Differently, the first, second, and third columns represent the density, velocity direction, and velocity magnitude maps for each case, respectively.

Table 3.4: Tracking precision and recall on in-silico dataset with and without the 2x2D RBF interpolators for the Relaxed FR strategy (100 Hz) and Relaxed Acquisition Times strategy (1/4 T).

	Precision	*Recall*
100 Hz (with IP)	0.72	0.34
100 Hz (without IP)	0.39	0.07
1/4 T (with IP)	0.81	0.48
1/4 T (without IP)	0.64	0.28

planes, demonstrates the best performance, delivering detail and clarity nearly comparable to the 1 kHz ULM across all dimensions. The qualitative analysis also are confirmed by the quantitative results in Table 3.3, where the results demonstrate the promising improvement in RMSE, and DICE similarity compared to ULM (100 Hz). This superiority of the performance of the proposed method in terms of similarity compared to the TEULM can be attributed to the combination of information in both orthogonal directions to

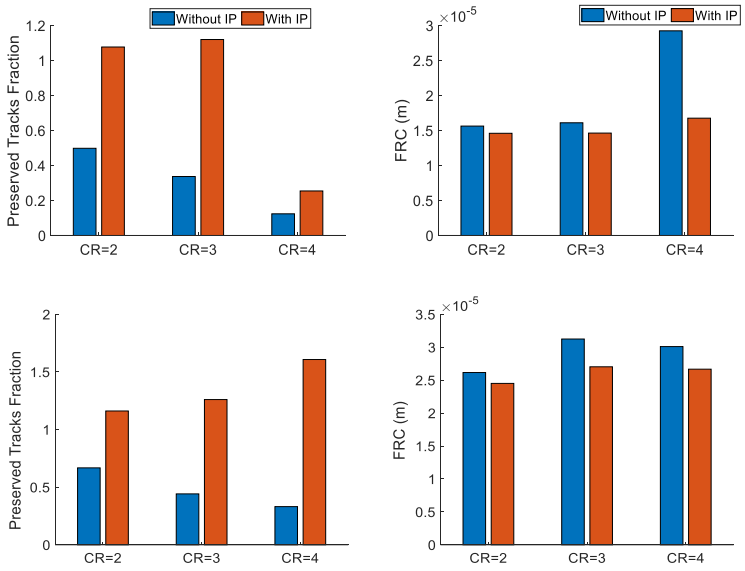

Figure 3.6: The preserved tracks fraction and FRC(m) evaluation without and with applying the proposed 2x2D interpolation technique for the relaxed acquisition time strategy. The first and the second rows respectively indicate the Rat's brain and kidney results (CR: compression ratio, i.e., $T'x = Tx/CR$).

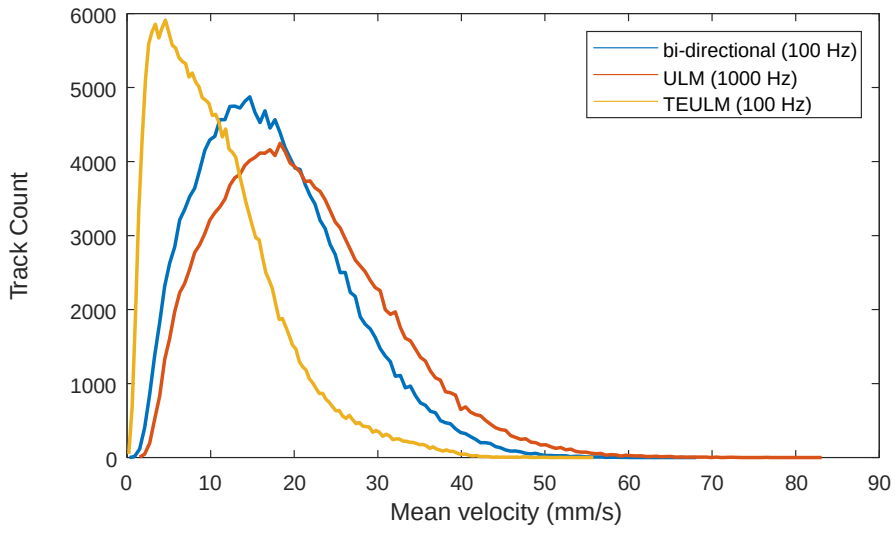

Figure 3.7: Mean velocity distribution for the Rat Brain dataset. The performance of the proposed technique at 100 Hz (blue line) is compared to ULM at 1 kHz (red line) and TEULM at 100 Hz (yellow).

Table 3.5: The quantitative analysis of the proposed technique (relaxed acquisition time) when applied to the rat brain data.

	Method	FRC (μm)	RMSE	DICE
$T'x = Tx$	Original	11.50	-	-
$T'x = Tx/2$	Without IP	15.63	39.80	0.70
	With IP	14.60	41.69	0.72
$T'x = Tx/3$	Without IP	16.10	41.90	0.69
	With IP	14.63	42.70	0.69
$T'x = Tx/4$	Without IP	29.24	49.68	0.39
	With IP	16.76	43.55	0.68

Table 3.6: The quantitative analysis of the proposed technique (relaxed acquisition time strategy) when applied to the rat kidney data.

	Method	FRC (μm)	RMSE	DICE
$T'x = Tx$	Original	24.75	-	-
$T'x = Tx/2$	Before IP	26.16	**5.4**	**0.84**
	After IP	**24.51**	9.0	0.83
$T'x = Tx/3$	Before IP	31.25	9.2	0.81
	After IP	27.03	11.3	0.78
$T'x = Tx/4$	Before IP	30.1	11.4	0.79
	After IP	26.67	16.3	0.78

compensate for the missing temporal information. By performing interpolation along both x and z directions, the method integrates data from multiple spatial dimensions more effectively, leading to a more comprehensive and accurate reconstruction of fine structures.

To show the effectiveness of the proposed 2x2D interpolation technique compared to using a single plane (either x-t or z-t), we provided the results for each plane separately in Fig. 3.3 and Table 3.3 (in the third (z-t) and fourth (x-t) columns) and standard LinIP. Additionally, we presented quantitative evaluations, including RMSE, resolution in μm (measured by FRC), and Dice score. Both qualitative and quantitative analysis of the z-t and x-t planes separately confirm that interpolation along the x-t direction carries more impactful information. While the z-t plane interpolation yields higher RMSE and lower Dice scores than even LinIP, its combination with the x-t plane as 2x2D enhanced the results. More specifically, the quantitative results indicate a higher structural similarity between the density maps produced by the proposed 2x2D RBF interpolation (82%) compared to the single-plane RBF interpolation (55% for the z-t plane and 79% for the x-t plane) and the LinIP method (62%).

Having demonstrated the effectiveness of the proposed 2x2D interpolation technique for the relaxed FR strategy, we applied this technique to the relaxed acquisition time strategy focusing on short acquisition times. The technique was deployed on datasets from the rat's brain and kidney, with results presented in Fig. 3.4 and Fig. 3.5, respectively. Evaluation metrics are detailed in Table 3.5 and Table 3.6.

In both datasets, when employing $T'_x = T_x/2$, the ULM technique without the interpolation also showed promising results, indicating that extremely long acquisition times are not always necessary. However, our suggested technique, when used to enhance resolution in combination with ULM, consistently produced higher quality super-resolved images. This improvement is quantitatively evident from the FRC values.

Increasing compression ratios lead to a loss of temporal information, which reduces the ability to resolve vasculature. The incorporation of our proposed technique becomes more significant as it notably enhances the depiction of vasculature. This enhancement is quantitatively supported by the resolution evaluation in terms of the FRC. It should be noted that the improvement in the resolution of the super-resolved images has been achieved without significant compromise in the $RMSE$ and $DICE$ similarity scores in the relaxed acquisition time strategy, which further reveals the efficacy of the suggested technique. The qualitative and quantitative results show that we are allowed to shorten the acquisition time in both datasets by a factor of 3 to 4, while still we can reach a comparable resolution and vasculator depiction compared to the case of considering the whole acquisition time. It should be noted that increasing the compression ratios larger than 4 ($CR > 4$) leads to the appearance of some vascular artifacts and loss of the vasculature in the final super-resolved images.

Given that the number of detected tracks significantly affects the quality of the reconstructed images, we analyzed the statistics related to the number of tracks at various compression ratios ($T'_x = T_x/CR$, where $CR = 2, 3, 4$) relative to the number of tracks at $CR = 1$ (i.e., $T'_x = T_x$). A higher fraction of preserved tracks signifies more accurate tracking of microbubbles, leading to better representation of blood flow dynamics, higher resolution, and improved image quality. To further investigate the veridicity of the tracks recovered utilising the proposed RBF interpolators, we have computed the precision and recall of the tracks for both strategies in an in-silico dataset (Table 3.4) and produced the density maps (Fig. 3.2). Results show the improvement in the depiction of complex vascular structures (magnified in the two ROIs in Fig. 3.2) for both strategies. In particular, when applying the 2x2D interpolation (With IP), the precision is above 70% for both strategies. The high precision value confirms the quality of the detected tracks after utilising the proposed interpolation technique. On the other hand, the percentage of recovered tracks (e.g. recall) is low, especially for the relaxed acquisition time strategy at 100 Hz. The analysis demonstrates the ability of the RBF interpolators in recovering tracks even at reduced FRs and decreased acquisition times. However, it also shows that relaxing the FR is more challenging. In fact, while the interpolation technique helps in correctly tracking MBs (high precision), it does not recover all the tracks present in the original dataset (low recall).

Furthermore, we assess the performance of the proposed technique through the resolution (FRC) trend at different compression ratios (Fig. 3.6). The figure illustrates the impact of 2x2D IP on preserved track fraction and FRC across different compression ratios. The left graphs show that using 2x2D IP significantly enhances the preserved tracks fraction for all tested compression ratios ($CR = 2, 3, 4$), indicating a substantial improvement in tracking quality. In contrast, the right graph shows that FRC values are generally lower with IP, particularly at $CR = 2$ and $CR = 4$, suggesting that IP not only

improves the fraction of preserved tracks but also enhances the resolution as measured by FRC. The improvement in FRC can be attributed to the increased preserved tracks fraction, as higher track numbers contribute to more precise localization. These findings highlight the dual benefits of using 2x2D IP, enhancing both tracking robustness and precision, and making it a favorable approach in ultrasound localization microscopy with the short-time acquisition process.

Considering the dynamic profiles in both the relaxed FR and acquisition time strategies, as demonstrated in TEULM [98], it is evident that increasing either the DS (downsampling) or CR (compression ratio) rates leads to a rise in the error of the reconstructed velocity profiles compared to the original ones. This increase in error is attributable to reconstruction inaccuracies in motion, highlighting the need to integrate a motion compensation technique into the proposed 2x2D interpolation method. Nevertheless, it's worth noting that although there is an underestimation of the velocity magnitudes in the relaxed acquisition time strategy, as evident in Fig. 3.4 and Fig. 3.5 (second rows), the proposed 2x2D interpolation technique successfully improves the reconstruction of flow directions compared to the results without applying interpolation.

Furthermore, by utilizing a bi-directional interpolation technique the velocity's magnitude estimate improves with respect to TEULM, which consists in applying the interpolation along one plane (x-t). In fact, Figure 3.7 shows that the proposed approach better recover velocity information when compared to TEULM at 100 Hz. Although there is an underestimation of the mean velocities, the bi-directional RBF-interpolators better capture the dynamics of MBs.

As a limitation of this study, we can mention that in the suggested 2x2D approach, we need 2 times interpolation in the $x-t$ and $z-t$ planes, therefore the improvement in the performance of the ULM imaging via 2x2D is achieved by increased computational complexity in the post-processing stage. Nevertheless, it is important to highlight that the total processing time is the sum of the beamforming time and the interpolation time. In addition, the proposed interpolation technique is applied after the beamforming stage, which also has the benefit of reducing the beamforming time. For instance, in the original scenario with a 1000 Hz FR, 1000 frames would need to be beamformed, leading to significant beamforming time even when using a simple delay-and-sum (DAS) beamformer. In contrast, with the proposed technique and a DS of 10, the total beamforming time is reduced by 90% per block. However, the total processing time is offset by interpolation time, which takes less than one minute (47 sec) for both planes with a regular computer (i.e., a system with Intel® CoreTM i7-8700 K CPU @ 3.70 GHz and 32 GB RAM) for each data block in dataset A when using the DS rate of 10 (i.e., reconstructing a data block of 800 temporal frames from 80 recorded frames at 100Hz).

3.5 Conclusion

In this paper, we applied a novel 2x2D RBF-based interpolation to ultrasound localization microscopy with two key objectives: to relax the requirement for very high FRs and to reduce acquisition time. We designed two strategies to achieve these goals. Additionally, we introduced a novel 2x2D interpolation technique that uses 2D RBF interpolation along

two orthogonal planes, integrating them for more accurate reconstruction. We applied the 2x2D technique to rat brain data, demonstrating that the FR can be reduced from 1 KHz to 100 Hz. Next, we applied the proposed technique, following the relaxed acquisition time strategy, to the rat's brain and kidney datasets. The results show that our technique can shorten the acquisition time by a factor of 3 to 4, while still achieving a super-resolved image quality close to the original case ($T'_x = T_x$) in terms of resolution, as measured by the FRC metric.Therefore, the proposed technique presents a promising strategy to relax acquisition requirements during preprocessing and instead design an efficient post-processing technique to compensate for the loss of temporal information, thereby producing high-quality super-resolved images. Finally, as highlighted in the discussion section, we plan to design a motion correction approach integrated with the suggested interpolation in future studies to further improve flow information in ULM imaging. It is confirmed that the low FR acquisition brings significant tracking errors, leading to low resolution, an underestimate of the velocity measurement, and a decrease in saturation for ULM reconstruction [105]. To tackle the issue, in future studies, we will focus on further improving the tracking stage utilizing the tracking with velocity constraints in the state-of-the-art [105] to be well adopted to the proposed technique.

Chapter 4

Towards reduced ULM acquisition times by uncoupling a bi-disperse microbubble population

This Chapter[3] proposes a solution to relax Ultrasound Localization Microscopy (ULM) constraint on low MB concentrations. ULM relies on precise localization and tracking of individual MBs. High MB concentrations yield to increased localization errors and, ultimately, ULM failure. ULM constraint on low MB concentrations results in long acquisition times, posing challenges in clinical settings. Here, we show the feasibility of uncoupling a bi-disperse MB population, composed of two monodisperse MB populations, in a 3D-printed vascular phantom. The uncoupling is performed through a signal processing pipeline that exploits the strong nonlinear response of MBs having resonance frequency tuned with the transmission frequency. After uncoupling, super-resolved density and velocity flow maps are generated for each MB population. The results demonstrate the capability of uncoupling the selected bi-disperse MB population, potentially permitting increased MB concentrations. This, in turn, could reduce acquisition times for microvascular ultrasound imaging, potentially facilitating ULM clinical translation.

4.1 Introduction

MB localization precision is crucial for the quality of the reconstructed images. However, ULM requires isolated MB signals for accurate localization. Failing to ensure MB sparsity would cause overlapping MB PSF in ultrasound images. Because localization errors related to such situations are high, these MBs are usually excluded from the analysis. As a result, ULM often operates with low MB concentrations, leading to long acquisition times to accumulate an adequate number of MBs to cover the micro-vasculature in the region of interest. To improve MB localization despite high concentrations, different flavors of deep neural network architectures have been proposed [106–109]. Furthermore, in [110],

[3]This Chapter appears in:
[J2] Tuccio, G., Te Winkel, Bruggeman C, Van Hoeve W, Demi L., "Towards reduced ULM acquisition times by uncoupling a bi-disperse microbubble population", In review, 2025

Table 4.1: Populations $p_{5.5MHz}$ and p_{3MHz} dimensions in micro-meter and resonance frequency in MHz.

	$p_{5.5MHz}$	p_{3MHz}
Diameter	2.5 μm	4.0 μm
Resonance Frequency	5.5 MHz	3 MHz

Huang et al. alleviated the localization problem for high-density injections by dividing the MBs into subpopulations based on flow dynamics.
Unlike the polydisperse MBs commonly used in ultrasound localization microscopy (ULM), monodisperse MBs exhibit a narrow size distribution. This small size variability enables optimal tuning of the imaging frequency to match the MBs specific characteristics (e.g. MB resonance frequency), thereby enhancing acoustic performance and improving ultrasound contrast imaging. This has been demonstrated by studies showing that monodisperse MBs reduce imaging artifacts and enable the visualization of deeper blood vessels [50–52]. In this study, we leverage the advantages of monodisperse MBs to overcome the trade-off between MB concentration and acquisition time. Specifically, we introduce a bi-disperse MB population composed of two distinct monodisperse MB types. We propose an uncoupling pipeline to separate these two populations based on their different frequency response. As a proof of concept, we apply this technique to ultrasound data acquired from a 3D-printed vascular phantom.

4.2 Methods

4.2.1 Bi-disperse MB population

By localizing and tracking the echoes produced by individual MBs flowing in the circulation, ULM generates micro-resolved density maps [111–114].

In this study, we uncouple a bi-disperse MB population. The bi-disperse population is composed of two monodisperse MB populations, each having a different frequency response. In particular, we select one population ($p_{5.5MHz}$) generating mainly the fundamental response, having the resonance frequency not tuned with the transmission frequency and one population (p_{3MHz}) producing a strong nonlinear signal, having the resonance frequency matching the transmission frequency. Thus, the non-linear signal intensity allows for the uncoupling of the two populations. $p_{5.5MHz}$ and p_{3MHz} diameter and resonance frequency are presented in Table 4.1. Figure 4.1 shows the Point Spread Function (PSF) and frequency response of $p_{5.5MHz}$ (in Fig. 4.1a) and p_{3MHz} (in Fig. 4.1b) obtained when acquiring the data at 3 MHz in water. The frequency response is evaluated as the Fourier transform along the fast time at the maximum-intensity line, shown in Figure 4.1 with the red dashed line. Being p_{3MHz} the population whose resonance frequency matches the transmission frequency, its frequency response is strongly nonlinear (in Figure 4.1b). Oppositely, $p_{5.5MHz}$'s frequency response exhibits a linear behavior.

The bi-disperse MB population used in this study is produced by Solstice Pharmaceuticals. Each monodisperse MB population is created using a microfluidic chip device

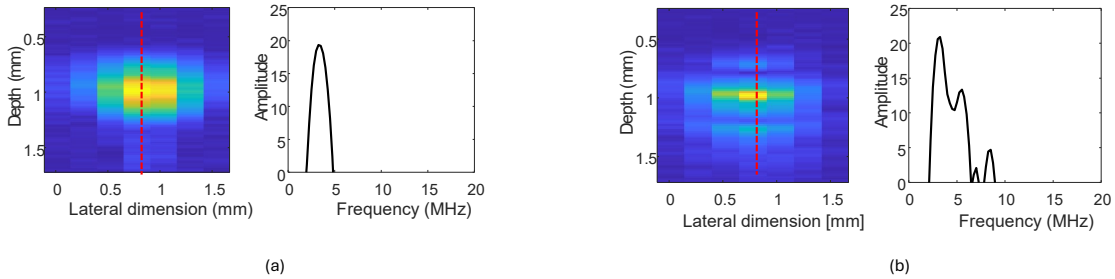

Figure 4.1: Full field Point Spread Function (PSF) and frequency response in dB for $p_{5.5MHz}$ (a) and p_{3MHz} (b). The frequency response is evaluated as the Fourier transform along the fast time at the maximum-intensity line, highlighted by the red dashed line.

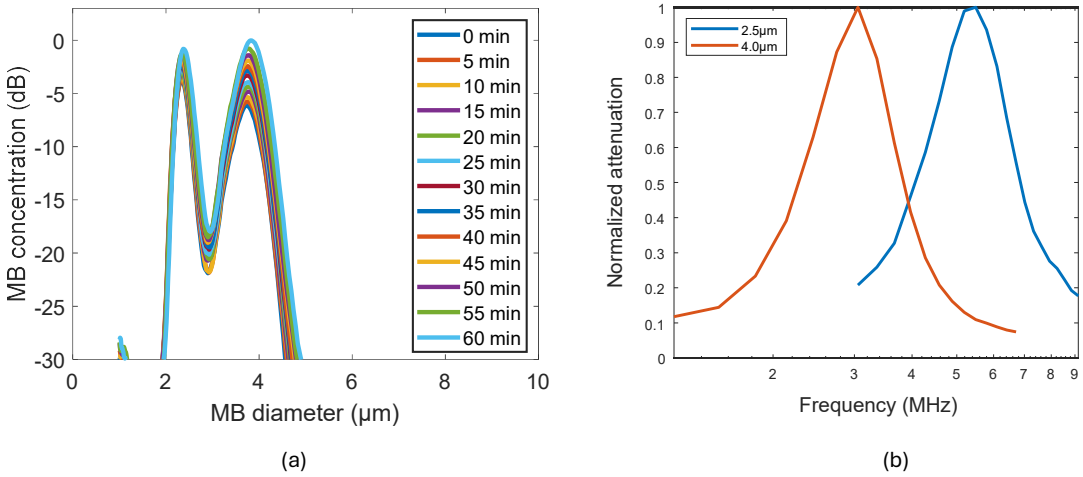

Figure 4.2: Size distribution (a) and resonance frequency (b) measurements for $p_{5.5MHz}$ (2.5 μm) and p_{3MHz} (4.0 μm), evaluated after MB production.

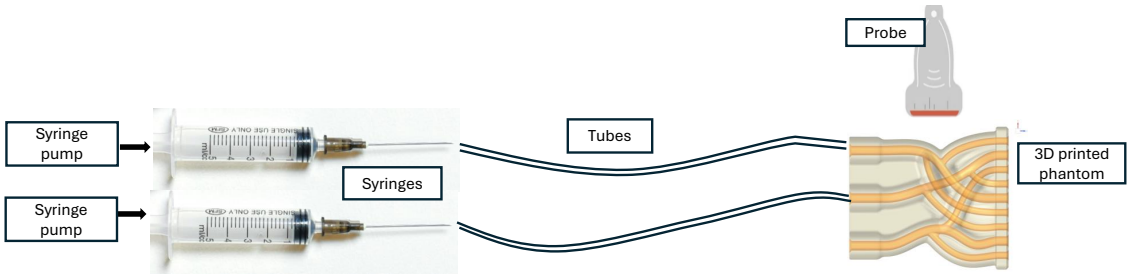

Figure 4.3: Experimental set up. The phantom has three injection points, two of which are connected through tubes to a pair of syringes, each containing a specific MB population. Continuous injections are performed using a syringe pump. Data acquisitions are performed using the ULAOP and and a linear array.

(MicroSphere Creator, Solstice Pharmaceuticals, Enschede, the Netherlands) [115]. The microfluidic chip allows for control of the dimension, and consequently, the resonance frequency of the MBs, ensuring monodispersity [116]. During the production phase, the chip mixes the gas and liquid with a flow rate tailored to the desired MB size. Following production, the MB size distribution and resonance frequency are measured. Figure **??** shows the size distribution of the bi-disperse population when mixed over an hour. The size distribution is measured every 5 minutes using a Coulter Counter (MultiSizer 4e, Beckman Coulter, Brea, CA). Figure **??**a demonstrates that the MBs remain bi-disperse in a time window typical of ULM. Figure **??**b displays the resonance frequency of $p_{5.5MHz}$ and p_{3MHz}. As in [117], the resonance frequency is estimated through attenuation for individual populations. Briefly, a 7.5 MHz (for $p_{5.5MHz}$) and 5 MHz (for p_{3MHz}) transducer (V309-SU and V320-SU, Olympus, Waltham, Massachusetts, USA) generate an acoustic beam, which after traversing a bubble screen, is reflected and received by the same transducer. The pulser (DPR300 Ultrasonic Pulser Receiver JSR Ultrasonic NY, USA) synchronises the transmitting and receiving phases [117]. In transmission, a broadbandwidth pulse is sent to the bubble screen. Then, the attenuation is measured as the difference between the received power spectrum crossing the MB screen and a reference spectrum measured without MBs. Finally, the resonance frequency is estimated to be the frequency showing the highest attenuation. The high control of the MB dimensions and their stability over time offers the possibility to select two distinguishable MB populations.

4.2.2 Data Acquisition

Ultrasound data were acquired with MBs flowing through a custom 3D printed flow phantom running at a constant flow rate with MBs varying concentrations (dilution of 10000x-20000x in de-gassed water). The phantom is printed in collaboration with PROM Facility, Rovereto, Italy, using the Selective Sintering Laser technique, which fuses polymer powders material via laser [118]. The laser thermal source allows heating of the polymer at a specific location, thus building the 3D solid structure layer-by-layer at a sub-millimetre scale. The material used to print the 3D vascular phantom (Flexa TPU, elastic module 76 MPa, and, density 1.04 g/cm^2) permitted ultrasound imaging. The 3D model design

is visible in Figure 4.3. The model has three injection points, and channels with varying dimensions ranging from a diameter of 2 mm to 1.5 mm.

The experimental data acquisition is performed with the phantom positioned vertically in a tissue-mimicking gel to avoid any movement during the acquisition process, as shown in Figure 4.3. In the study, we utilize two injection points, each connected to a syringe pump flowing at a constant rate of 2 ml/min. Each syringe contains a different MB population. MB populations are diluted in de-gassed water and kept in suspension with a steering plate. Injections of 20 ml are performed continuously. Ultrasound data are acquired for each MB population singularly and simultaneously. For individual injections, we inject MBs into the first channel and water in the second channel for $p_{5.5MHz}$, while for p_{3MHz}, the injections are reversed.

To acquire the radio-frequency data, we employ a programmable ultrasound platform (ULAOP), and a linear array probe (Esaote LA533, Florence, Italy [119]), placed horizontally to the 3D printed channels, as shown in Figure 4.3. Line-by-line was implemented acquiring 64 lines for each image. A pulse with a center frequency of 3 MHz and bandwidth of 1 MHz was used in transmission. For each record, 250 frames are acquired with a frame rate of 187 Hz. The sampling frequency is 50 MHz.

4.2.3 Ultrasound Data Processing for ULM

To generate the density and dynamic maps of the MB populations, we implement a common ULM framework, summarized in Figure 4.4. After data acquisition, filtering is applied to the ultrasound RF data. Specifically, filtering is implemented by a Butterworth band-pass filter, with 2 MHz and 20 MHz as lower and upper cut-off frequencies. A spatio-temporal SVD filter is then applied. The SVD filter removes the first k-value of the decomposition, assuming that these represent the coherent spatio-temporal background signal [111, 114]. In this study, the k-value is experimentally selected to 5, consistent with the range discussed in other studies [111, 120]. Next, the MBs uncoupling is deployed to generate two subsets of ultrasound images, each of which represents one of the uncoupled populations ($h_{p_{3MHz}}$ for population p_{3MHz} and $h_{p_{5.5MHz}}$ for population $p_{5.5MHz}$). Finally, the ULM framework comprising detection, localization, tracking, and accumulation is applied. The detection step is performed using two different methods (I_{pix} and ncc):

1. Localization using Pixel Intensity (I_{pix}). The technique, presented by Couture et. al. [120], assumes that an MB echo is represented by the brightest pixels in the ultrasound image. The technique requires estimating m (the number of MBs) present in each frame. Here, m is optimally selected to 30-50 MBs/frame based on the dilution. Next, the m brightest pixels, isolated at least by the dimensions of a MB PSF are considered MB detections.

2. Localization through correlation (ncc). Similar to [121, 122], this technique utilizes a mean PSF obtained by acquiring the ultrasound data of $p_{5.5MHz}$ and p_{3MHz} in water. The PSF is specific to each population and is obtained by averaging the PSF of 20 MBs in different acquisitions. The PSF for the two populations can be seen on the right side of Figure 4.4b. For each frame, a 2D normalized cross-correlation

between the filtered images and the MB PSF is evaluated. This results in a cross-correlation map, where the peaks correspond to MB detections. To further improve the detection performance, a threshold of 0.5 is selected as the minimum correlation to consider the pixels as MB signals. This threshold value was empirically selected based on the data of this study. If the correlation is lower than the threshold value the pixels are considered background noise and excluded.

The comparison between two detection algorithms provides a proof of the robustness of the proposed uncoupling pipeline. In this way, we confirm the uncoupling capability when using a standard algorithm (brightest pixel), while demonstrating the possibility of improving the performance using a model-based algorithm (normalized-cross-correlation). To ensure a fair comparison between the two methods, the parameter values were determined empirically through a parameter search optimization.

After detection, a Gaussian fitting [111, 112, 120] is performed to further refine the localization estimate. For each detection, a Gaussian distribution is fitted by sub-sampling the pixels by a factor of 10, as described in [120].

Next, MB centroids for each population are tracked through a bipartite matching algorithm. The algorithm finds the optimal frame-to-frame pair for all the MB signals, matching them in such a way that the total distances of all the MBs are minimized [120, 123]. Repeating the process for all the frames in a record generates MB tracks. To improve tracking precision, MBs with persistence shorter than 7 frames are discarded. Finally, density and dynamic maps are obtained through the accumulation of these tracks.

4.2.4 Microbubble Uncoupling

The uncoupling is performed as a pre-processing stage (see Fig. 4.4). First, we apply a Butterworth filter to separate the first and second harmonic components. The filter has a center frequency of 3 MHz and 6 MHz for the first and second harmonic respectively, and 1 MHz of bandwidth. Next, we apply a Hilbert transform to generate the ultrasound images associated with the first (h_1) and second (h_2) harmonic signal. As shown by Fig. 4.4b, the uncoupling is performed as follows:

- $p_{5.5MHz}$ is the population characterized by a resonance frequency (5.5 MHz) not matching the transmission frequency (3 MHz) and, as a consequence, by a linear response. $p_{5.5MHz}$ images ($h_{p_{5.5MHz}}$) are obtained by subtracting the first (h_1) and second (h_2) harmonic images:

$$h_{p_{5.5MHz}} = h_1 - h_2. \tag{4.1}$$

  An example of PSF for h_1, h_2 and $h_{p_{5.5MHz}}$ is shown in Figure 4.5b.

- p_{3MHz} is the population whose resonance frequency matches the transmission frequency (3 MHz) and thus has a strong nonlinear response. p_{3MHz} is isolated by imaging the second harmonic:

$$h_{p_{3MHz}} = h_2. \tag{4.2}$$

  The first (h_1) and second (h_2) harmonic PSFs of a MB belonging to population p_{3MHz} are shown in Figure 4.5b.

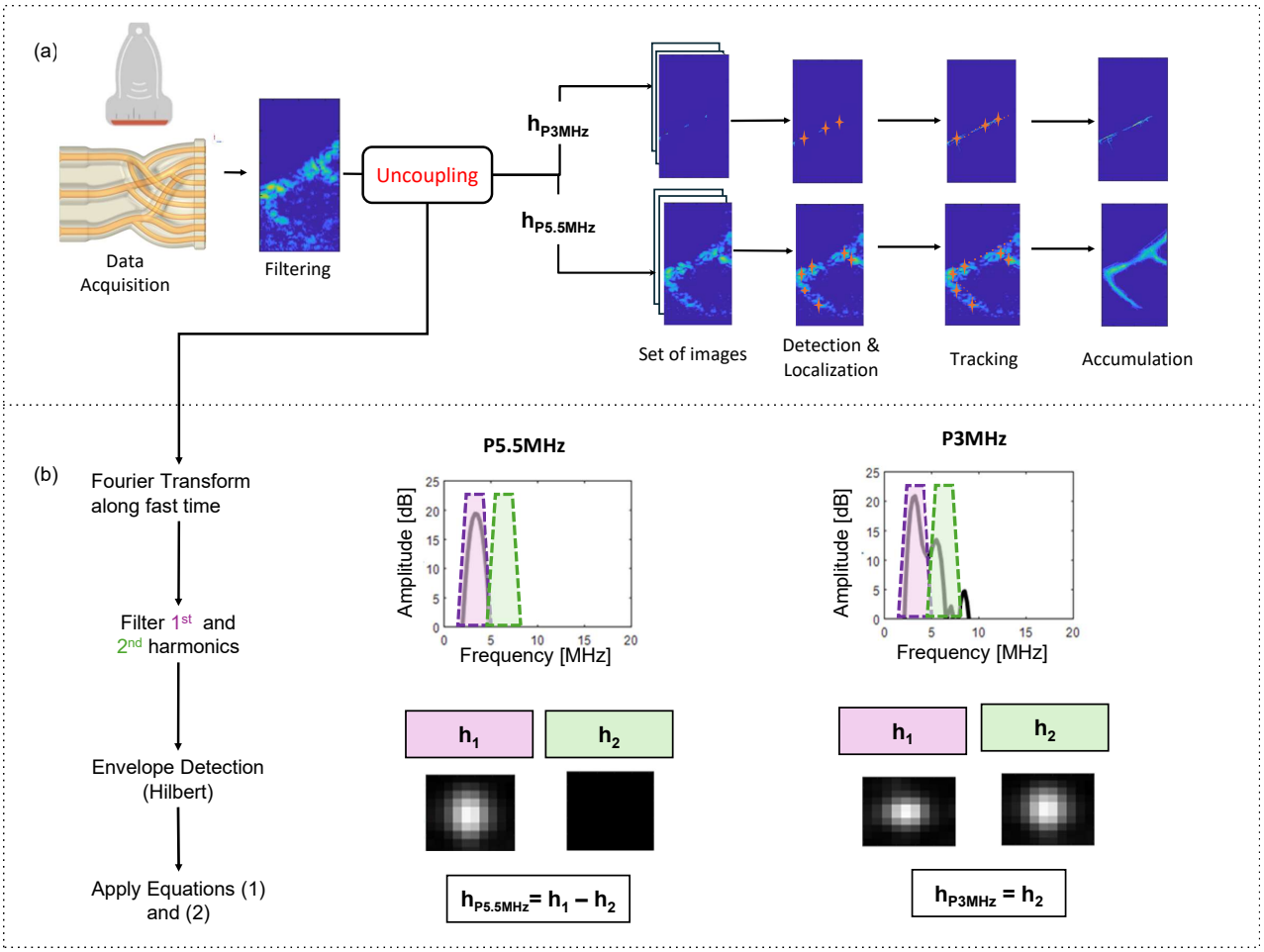

Figure 4.4: At the top (a) uncoupling pipeline for the bi-disperse MB population. Uncoupling is performed after data acquisition and filtering. As a result of the uncoupling, a set of images for each population ($h_{p_{5.5MHz}}$ for $p_{5.5MHz}$ and $h_{p_{3MHz}}$ for p_{3MHz}) are obtained. Next, a ULM framework comprising of detection, localization, tracking and accumulation, is applied. At the bottom (b) detail of the uncoupling procedure of $p_{5.5MHz}$ and p_{3MHz}. First, the first and second harmonics are filtered employing a Butterworth filter in the frequency domain. Successively, the envelope detection is used to generate the images of the first (h_1) and second harmonics (h_2). Images of the two populations $h_{p_{5.5MHz}}$ and $h_{p_{3MHz}}$ are evaluated as $h_1 - h_2$ and h_2 respectively.

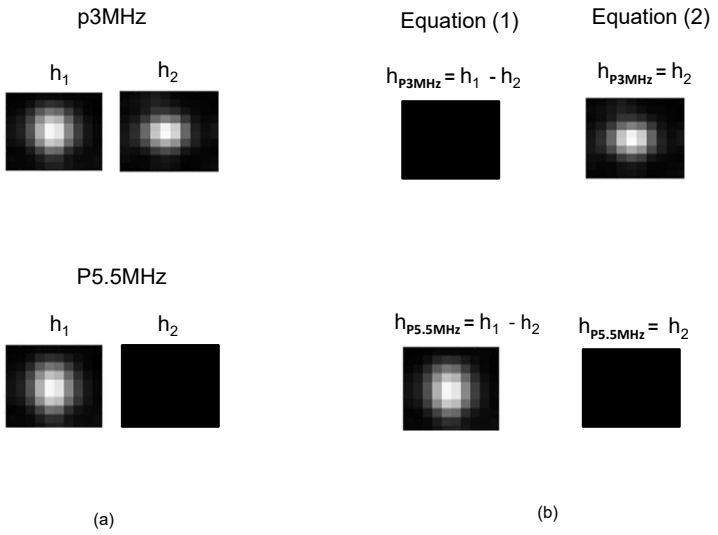

Figure 4.5: Example of h_1 and h_2 for population p_{3MHz} and $p_{5.5MHz}$ (a). Results of applying Equations 4.1 and 4.2 to both populations (b).

Note that, by applying 4.1 to population p_{3MHz} would cancel out this MB population signal. Similarly, using equation 4.2 to image $p_{5.5MHz}$ would cancel out its contribution. As such, the equations allow to selectively image each MB population, thus allowing the uncoupling. To verify this, we perform the experiments having only one population injected in one channel, meanwhile flushing water in the other. This choice would allow us to understand the potential cross-talk between the two MB populations. Next, we apply the proposed pipeline when injecting the two MBs populations at the same time.

4.3 Results

This work demonstrates the feasibility of uncoupling the bi-disperse MB population based on the intensity of each MB's population nonlinear response. In fact, we are able to reconstruct density and flow dynamics maps in a 3D printed phantom using the proposed uncoupling pipeline (Fig. 4.4).

Figures 4.6a and 4.6b show respectively the density and flow direction maps for the detection method based on the brightest pixels (I_{pix}) and normalized cross-correlation method (ncc). After data acquisition for separate injections of each population, the uncoupling generates images of population $p_{5.5MHz}$ and p_{3MHz}, marked as $h_{p_{5.5MHz}}$ and h_{p_3MHz}. Figure 4.6b shows the flow direction images which are color-coded, with red marking the flow away from the probe, and blue the flow towards the probe. Individual injections serves as an initial validation for the uncoupling pipeline while having a ground truth. During single injections and in case of perfect uncoupling, the residual images, obtained

by attempting to image the non-injected population, should be empty. For instance, in 4.6a first column, only p_{3MHz} has been injected. After injection, the uncoupling and ULM pipeline produce images of both populations h_{p3MHz} and $h_{p5.5MHz}$, using Equations 4.1 and 4.2, respectively. As such, h_{p3MHz} displays tracks of the MB population, since p_{3MHz} is the population injected. On the other hand, $h_{5.5MHz}$ is empty, as it attempts to image the population which is not present. We mark the residual images with a red background for both the density and flow direction maps (Fig 4.6).

Intensity profiles of two cross-sections for both detection methods (I_{pix} and ncc) are displayed in Figure 4.7a and 4.7b, for p_{3MHz} and $p_{5.5MHz}$ respectively. Additionally, the full width half maximum (FWHM) values further highlight the ability of the proposed pipeline to depict the geometry of the vascular structures (see arrows in Fig. 4.7).

Table 4.2 shows the quantitative metrics for the density maps generated for the two populations utilizing I_{pix} and ncc as detection methods. The table presents the results in terms of saturation, evaluated as the number of pixels covered by MBs tracks, mean detections per frame and mean tracks per record. The mean track/record is the average value of the total tracks found after applying the bi-partite tracking algorithm. The mean detections/frame and mean tracks/frame metrics are particularly relevant in discussing the performance of the uncoupling pipeline. In fact, knowing which MB population is present in each channel, the number of residual detections and tracks is a direct evaluation of false positives. Finally, we evaluate the percentage of mean accepted track per record, which represents the percentage of the total number of tracks after filtering out short tracks. This metric reflects tracks quality, since short tracks are likely the results of poor detections and noise, and, as such, are unreliable for micro-vascular reconstruction [124, 125].

Figure 4.8 shows the ncc generated tracks for both populations superimposed with the 3D printed phantom design.

Figure 4.9 and Table 4.3 show the density maps and the evaluation metrics generated when injecting the two populations simultaneously for both detection methods. Furthermore, a comparison with density maps generated by using a standard ULM pipeline before uncoupling for both methods is presented in Fig. 4.10. Note that for the I_{pix} detection method the number of MBs present per frame has been increased to account for more MBs present in one frame. Regarding the ncc detection method, the same correlation threshold has been applied.

4.4 Discussion

We have proposed and demonstrated the effectiveness of an uncoupling pipeline that exploits the nonlinear response differences of two MB populations forming a bi-disperse MB population. Results highlight the performance of the technique when individual (Fig. 4.6) and simultaneous (Fig. 4.9) injections are performed. Figures 4.6 and 4.9 show density maps obtained utilizing two detection methods: the brightest pixel (I_{pix}), a context-unaware detection method, and normalized cross-correlation (ncc), a model-based detection approach. These results confirm the robustness of the proposed uncoupling pipeline in separating the bi-disperse population. Furthermore, the flow direction maps

(Fig. 4.6b) demonstrate that the proposed pipeline preserves flow information. Note how the color encoding, with blue representing MB flow towards the probe and red away from it, is consistent with the direction imposed by the experimental setup. The performance of the proposed method is further supported by the quantitative results in Table 4.2, where saturation, mean detections and mean tracks decrease in the residual column (marked in red in Table 4.2, reinforcing uncoupling capability).

Fig. 4.6 demonstrate that *ncc* outperforms I_{pix}. This is visible from the spurious tracks present in the residual images. For instance, observe the tracks present in the lower part of image $h_{p_{5.5MHz}}$ generated using I_{pix} for injections of p_{3MHz}. In this image, I_{pix}-generated images show a high number of false positives tracks compared to *ncc*. The reason for I_{pix} lower uncoupling performance lies in the way I_{pix} works. I_{pix} detections are pushed to find the m brightest pixels. However, these pixels might be the result of uncoupling errors or the filtering results, leading to false positive detections and the appearance of spurious tracks. I_{pix} detects on average 4.2 MBs/frame for $p_{5.5MHz}$ when injecting p_{3MHz} (see Table 4.2). For the same case, *ncc* detects 1.5 MBs/frame, showing better uncoupling performance. The improved separation capability of a model-based detection method (*ncc*) is confirmed by the mean tracks per record and the mean percentage of accepted tracks in Table 4.2. On average for p_{3MHz} injections, *ncc* accepts 3.1 % of the detected tracks for $p_{5.5MHz}$, whereas I_{pix} accepts 15 % of the tracks, causing the appearance of false tracks. Despite a similar mean number of tracks/record for p_{3MHz} for acquisitions where only p_{3MHz} is present, the mean tracks/record substantially drops for $p_{5.5MHz}$ (from 124.9 to 14 tracks/record) when using *ncc* method. The high number of tracks indicates a large number of tracks likely caused by false positive MB detections, reflecting I_{pix} poorer uncoupling performance. However, these false positive tracks are partially filtered out by the track length threshold.

The robustness of *ncc*'s detection performance is further evident from the density profiles shown in Figure 4.7. For instance, observe the profile for cross-section 1 in Figure 4.7b, where *ncc* allows the visualization of different phantom branches with comparable intensity. Although I_{pix} produces tracks for both channels, the number of detected MBs flowing in one of the two channels is significantly higher. While *ncc* shows better separability, the performance improvement comes at the cost of a higher computational demand. Table 4.3 confirms the superiority of *ncc* for uncoupling the two populations when injected together across all the metrics. The mean detections per frame (see Table 4.3) are higher for the *ncc* method, leading to more tracks and a more saturated final density map, confirming the analysis of single injections. However, the tracks obtained with the *ncc* method for population p_{3MHz} (Fig. 4.9 b) appear to be more scattered and less smooth, probably due to the higher number of detections, which make the tracking more challenging. Figure 4.9 presents a few spurious tracks, which could be the result of errors in the uncoupling pipeline. However, the number of tracks resulting from the uncoupling allow to uncouple the two MBs populations. To demonstrate the potential advantage of using the proposed technique with respect to standard ULM, we compare the density maps generated before (Fig. 4.10) and after uncoupling (Fig. 4.9). The reconstructed map highlights how the proposed pipeline better reconstructs the geometry of the phantom for both methods. The main reason for the improved performance can be explained by the fact that, when

Table 4.2: Results for the two detection methods I_{pix} (brightest pixel) and *ncc* (normalized cross-correlation).

	I_{pix}			
	Injections of p_{3MHz}		Injections of $p_{5.5MHz}$	
	$h_{p_{3MHz}}$	$h_{p_{5.5MHz}}$	$h_{p_{5.5MHz}}$	$h_{P_{3MHz}}$
Saturation (%)	9.1	4.1	10	0.5
Mean detections/frame	6	4.2	15	2
Mean tracks/record	150.3	124.9	358	20
Mean accepted tracks (%)	57	15	27.7	1

	ncc			
	Injections of p_{3MHz}		Injections of $p_{5.5MHz}$	
	$h_{p_{3MHz}}$	$h_{p_{5.5MHz}}$	$h_{p_{5.5MHz}}$	$h_{P_{3MHz}}$
Saturation (%)	10.7	1	12	0.4
Mean detections/frame	5	1.5	11.2	1
Mean tracks/record	104.5	14	334	12
Mean accepted tracks (%)	28.2	3.1	16.7	0.1

Table 4.3: Results for the two detection methods I_{pix} and ncc when injecting the two MB populations simulaneously.

	I_{pix}		*ncc*	
	$h_{p_{3MHz}}$	$h_{p_{5.5MHz}}$	$h_{p_{3MHz}}$	$h_{p_{5.5MHz}}$
Saturation (%)	12.4	14.1	18.3	13.2
Mean detection/frame	10	10	17	21
Mean track/record	347	168.6	923	822
Mean accepted tracks (%)	44.7	74.2	62.8	57.3

both MBs are present, there is a higher concentration of MBs, which make standard ULM more difficult. For I_{pix} density maps, fewer tracks are present, probably due to the higher number of overlapping MBs detections. On the other hand, *ncc* appears to reconstruct the vasculature, but more spurious tracks are present.

Results highlight the advantage of using 3D printed vascular phantoms as physical ground truth for assessing ULM-generated maps. There are few missing branches in the reconstructed density maps, which can be explained by the misalignment between the imaging plane and the phantom positioning. Nevertheless, the reconstructed tracks align with the phantom geometry (Figure 4.8) and the vascular dimension estimated from ULM images are consistent with those of the phantom. In Figure 4.7, the channel width is evaluated at the FWHM of the intensity profiles and found to be approximately 2 mm, matching the phantom's inner diameter.

This study presents several limitations. Firstly, the stability and separability studies have been tested on data acquired in a 3D printed phantom. While these *in vitro* results provide an opportunity to validate the proposed approach, testing it on clinical *in vivo* data is essential to assess the method's feasibility in a physiological context, character-

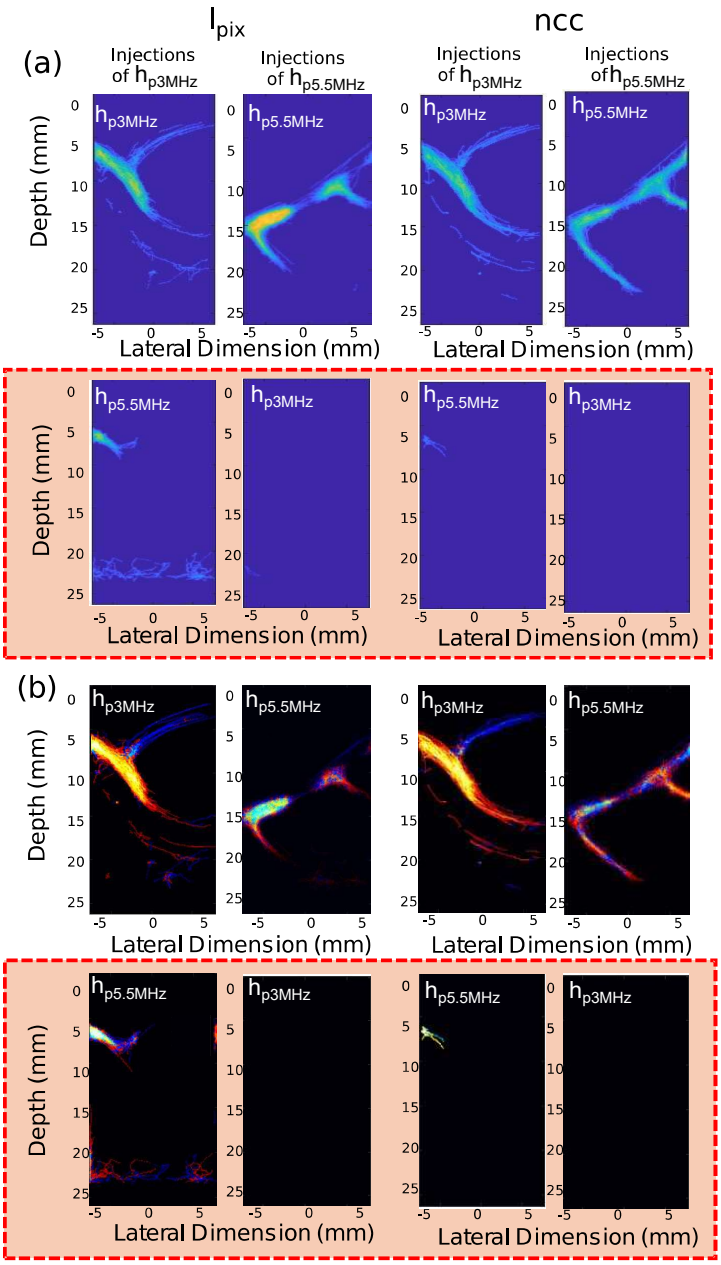

Figure 4.6: ULM-generated density (a) and flow direction (b) maps for population $p_{3\text{MHz}}$ ($h_{p_{3\text{MHz}}}$) and $p_{5.5\text{MHz}}$ ($h_{p_{5.5\text{MHz}}}$). The first row of (a) and (b) represents the images of $p_{3\text{MHz}}$ and $p_{5.5\text{MHz}}$ when injecting them individually; the second row shows the images of each when injecting the other. Images are shown for detection methods I_{pix} and *ncc*. In (b), flow direction is color-coded: red = flow away from the probe, blue = flow toward the probe.

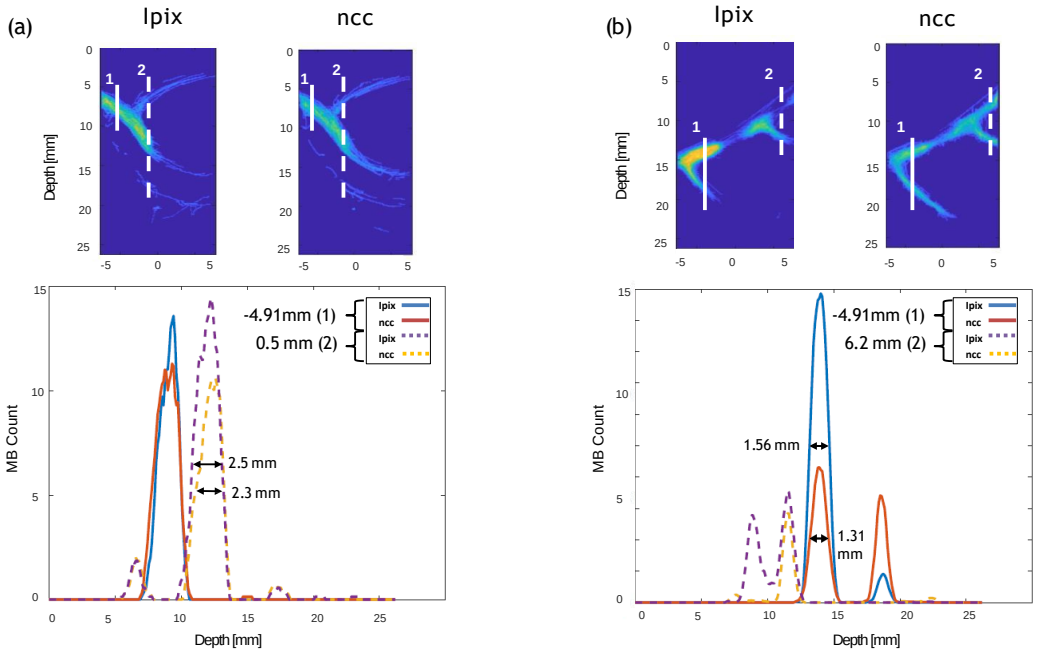

Figure 4.7: One-dimensional intensity profiles at different depths as indicated in the top images corresponding to the solid (1) and dashed line (2). The FWHM values are indicated in millimeters and by black arrows. Images are shown for detection methods I_{pix} and *ncc*, for population p_{3MHz} (a) and population $p_{5.5MHz}$ (b).

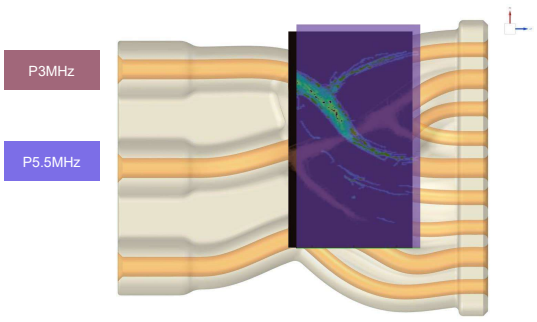

Figure 4.8: Superimposed image of the ULM generated density maps with the phantom design utilizing *ncc* as detection method.

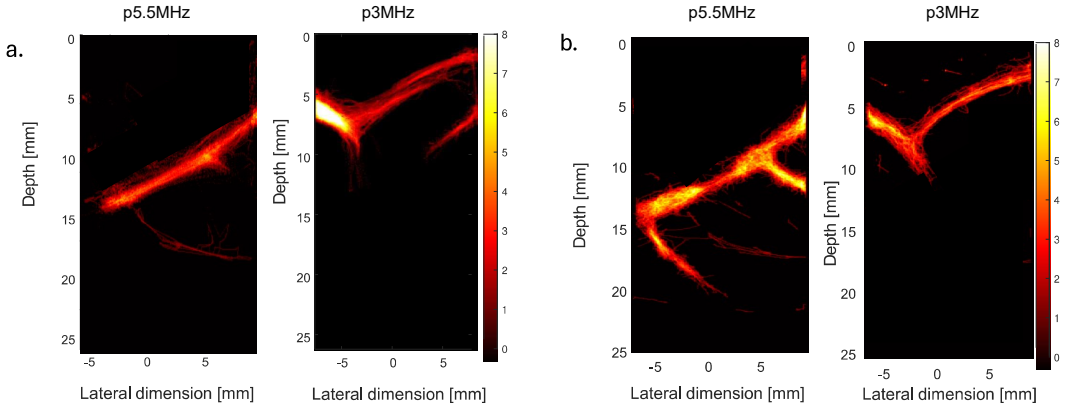

Figure 4.9: Density maps generated after uncoupling when injecting the MB populations simultaneously. Maps are generated using I_{pix} (a) and ncc (b).

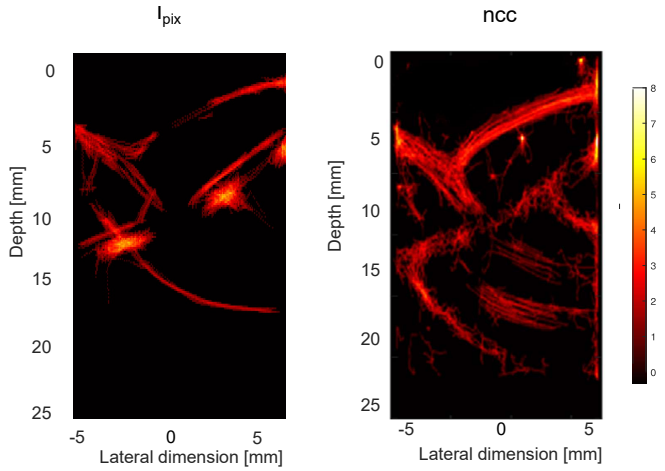

Figure 4.10: Standard ULM generated density maps (before uncoupling) for the simultaneous injections using two detection methods: I_{pix} and ncc.

ized by many challenges, such as attenuation of MB signals and motion. Furthermore, a natural extension of the study involves injecting a mixture of the two monodisperse populations, rather than performing injections either individually or simultaneously. This next step is crucial not only for validating the MB response when both populations are present, but also verifying the uncoupling performance of the proposed algorithms and investigating the feasibility of increasing MB concentrations. By mixing the two populations, we can assess the effectiveness of the uncoupling technique in real-world scenarios. Furthermore, given the control on 64 elements, line-by-line imaging has been implemented for this study. While this choice guarantees a wide field of view, it comes at the price of lower frame rates compared to ultrafast imaging normally implemented in standard ULM. In future *in vivo* studies, we plan to implement plane wave imaging, which would allow to achieve higher frame rates. Finally, a limitation of this study is the variability of the *in vitro* experiments due to the manual selection of the imaging plane and phantom instability. As a consequence, some vascular branches present in the phantom are not visible in the final density and velocity maps. To solve this, improvements on the replicability of the set up can be performed. In addition, 3D imaging would solve the imaging plane selection issue.

4.5 Conclusions

In this study, we demonstrate the feasibility of uncoupling a bi-disperse MB population. Results show the ability of the proposed uncoupling pipeline to generate dynamic and functional maps when singularly and simultaneously injecting distinct MB populations in two separate phantom branches. We tested the proposed uncoupling framework using two detection methods. I_{pix} performs detection based on the brightest pixels, whereas *ncc* utilizes cross-correlation for detecting MBs. Both methods allow the uncoupling of the two selected populations. However, results show a better performance of a model-based approach (*ncc*) with respect to a context-unaware method (I_{pix}). Furthermore, we compare the reconstructed density maps before and after uncoupling. Results confirm that standard ULM fails to capture the vasculature, possibly due to high MBs concentrations, whereas by utilizing the uncoupling technique, the reconstructed vascular structures appear to better represent the ground truth geometries. As a future work, we plan to simultaneously inject in the same channel the two populations to verify the advantage of using a bi-disperse population over a poly- and/or mono-disperse population. Furthermore, we plan to perform *in vivo* experiments to verify the separability of the bi-disperse MB population and the performance of the proposed uncoupling pipeline towards advanced ULM. This would ultimately allow for an increase of MBs concentrations, thus alleviating the need for long acquisition time for micro-vascular imaging.
In addition, it is worth highlighting that in this study we 3D-printed a vascular phantom compatible with ultrasound imaging. As a next step, we aim at 3D printing structures having dimensions and geometries comparable with the *in-vivo* vascular bed. The phantoms would provide a fully controllable tool to validate ULM's results both in terms of geometry depiction and velocity information.
Finally, the use of different populations might benefit not only on a practical level (short-

ening the acquisition time) but also on a more diagnostic and monitoring level. Depending on the MBs' sizes, different populations might selectively transit in micro-vessels characterized by different properties.

Chapter 5

Increasing Microbubble Concentrations in Microvascular Imaging via Microbubble Separation by means of Orthogonal Frequency Division Multiplexing

This Chapter[4] introduces a bi-disperse MB population (i.e. two monodisperse MB populations), which are separable through Orthogonal Frequency Division Multiplexing (OFDM). Results in a flow channel phantom demonstrate the feasibility of uncoupling the two MB populations. Thus, the proposed approach might alleviate the requirement of low MBs concentration, ultimately allowing for faster microvascular imaging.

5.1 Introduction

The quality of the ULM-generated images depends on the precision of MBs localizations, which in turn is influenced by the spatial distance between the MBs signals. While sparser MBs signals ensure more precise localizations, they extend the time necessary for microvessel imaging. This substantially affects the imaging of capillary structures, where the limited perfusion and the constraint on spatially isolated MBs negatively influence the acquisition times [54, 125, 126]. Intuitively, increasing MBs concentrations would shorten the acquisition times, but would decrease the probability of isolated MBs signals. Thus, ULM is limited to low MBs concentrations and long acquisition times, which are challenging in the clinical setting.

In this study, we introduce OFDM to separate different monodisperse MBs populations based on their backscattered signals. This allows for increasing MBs concentrations and,

[4]This Chapter appears in:
[CP1] Tuccio G, Te Winkel L., Bruggeman C., Van Hoeve W., Demi L., "Increasing Microbubble Concentrations in Microvascular Imaging via Microbubble Separation by means of Orthogonal Frequency Division Multiplexing" in IEEE Ultrasonics, Ferroelectrics, and Frequency Control Joint Symposium, UFFC-JS, 2024

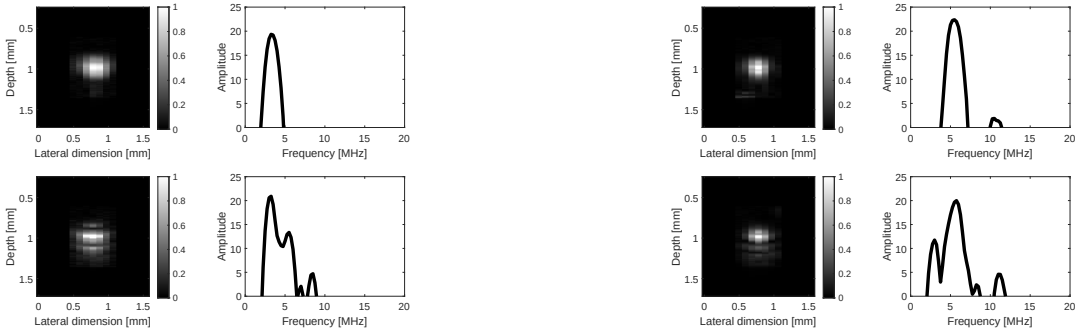

(a) (b)

Figure 5.1: PSF and frequency response of population p_{3MHz} (first row) and $p_{5.5MHz}$ (second row) when acquired in water at 3 MHz (a) and 5.5 MHz (b) transmission frequency.

ultimately, reduces the acquisition times for microvascular imaging.

5.2 Materials and Methods

5.2.1 Monodisperse Microbubbles

MBs backscattered signal depends on their dimension, which is linked to the resonance frequency [127]. By selecting two monodisperse MB populations characterized by different diameters, it is possible to discriminate between the signals produced by each population. Thus, having a way to discriminate between MB signals would offer the possibility of increasing MBs concentrations. Table 5.1 shows the features of the two populations used in this study (p_{3MHz} and $p_{5.5MHz}$). The monodisperse MB populations are produced through a microfluidic chip, which allows control on their size and, consequently, on their resonance frequency.

5.2.2 Proposed method

OFDM allows ultrasound imaging by transmitting multiple parallel beams [128, 129]. Here, OFDM is used to separate MB populations based on the different frequency response of each MBs population when insonified with a transmission frequency tuned with the MB's resonance frequency. Thus, we utilize OFDM to transmit two parallel beams with center frequencies at 3 MHz and 5.5 MHz, and 1 MHz bandwidth. The Point Spread Function (PSF) and frequency response of p_{3MHz} and $p_{5.5MHz}$ when acquired using the two transmission frequencies are displayed in Figure 5.1. Data are acquired in a flow channel phantom composed by two parallel channels. To acquire the radio-frequency

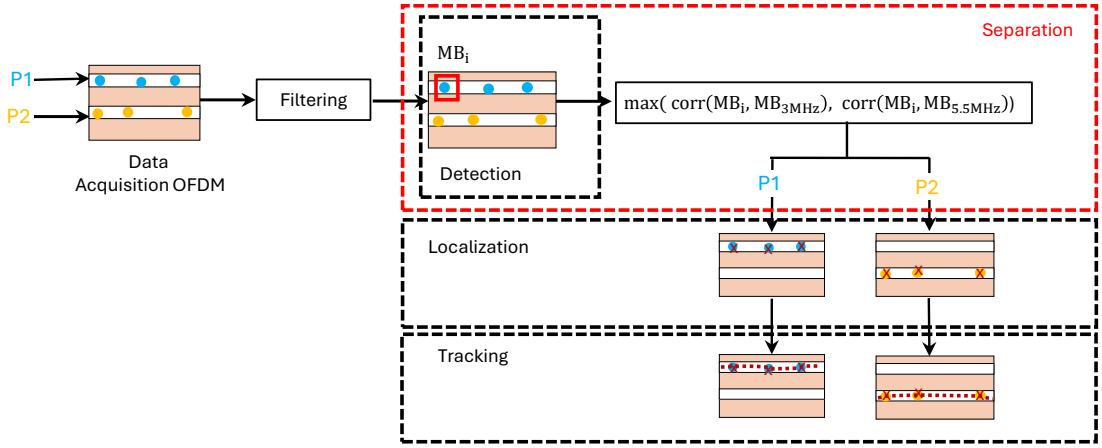

Figure 5.2: Proposed method to separate two monodisperse populations (p_{3MHz} and $p_{5.5MHz}$) using ODFM to transmit at the resonance frequency of the MBs (3 MHz and 5.5 MHz).

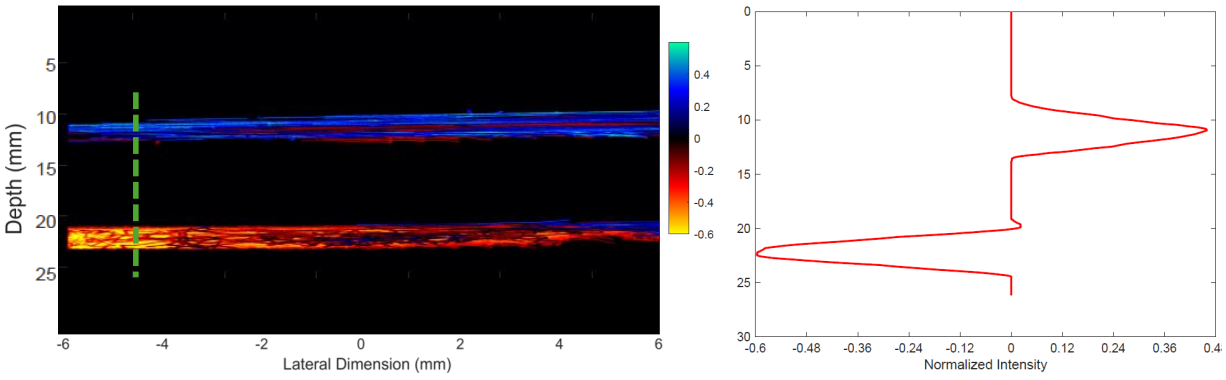

Figure 5.3: Density maps after the simultaneous injection of p_{3MHz} (blue) and $p_{5.5MHz}$ (red). Normalized Intensity profile of the maps obtained at -4.5 mm lateral dimension (dashed green line).

Table 5.1: Diameter and resonance frequency of the selected MBs populations.

	Diameter	Resonance Frequency
$p_{5.5MHz}$	2.5 μm	5.5 MHz
p_{3MHz}	4 μm	3 MHz

data we employ a programmable ultrasound platform (ULAOP), and a linear array probe (Esaote LA533). MBs separation is performed at the detection step, see Fig. 5.2. After background filtering, for each frame of the acquisition, the normalized cross-correlation between each MB signal (MB_i) and the MB signal of each population acquired in water when transmitting at the same frequency as the resonance frequency (MB_{3MHz} and $MB_{5.5MHz}$) is evaluated. The maximum cross-correlation is used to assign each detection to one population. After the assignment, for each population, the MBs are localized through a Gaussian fitting and tracked by means of the Hungarian algorithm [111, 130].

Finally, the micro-resolved density maps for each population are obtained through accumulation.

As a proof-of-concept, we first perform injections of a single population. This would allow us to quantitatively assess the performance of the separation algorithm. In fact, knowing that only one population is present in the data, it is possible to evaluate the number of MBs of each population correctly assigned (true positives, TP) and the number of MBs erroneously assigned (false positives, FP). The number of true and false positives allows us to quantitatively assess the precision as $precision = \frac{TP}{TP+FP}$. Next, we generate the density maps utilizing the proposed pipeline when injecting the two MB populations simultaneously.

5.3 Results

After performing single injections of each population, the precision for p_{3MHz} and $p_{5.5MHz}$ is 0.73 and 0.62, respectively. Figure 5.3 shows the density maps when injecting the two populations simultaneously and the normalized intensity profile associated with the density map at -4.5 mm lateral dimension, indicated by the green dashed line. Results demonstrate MBs separability, thus confirming the feasibility of increasing the concentrations and reducing the acquisition times.

5.4 Conclusion

In this study, we propose a novel approach toward the increase of MBs concentration. In particular, we demonstrate *in vitro* the feasibility of separating a bi-disperse MB population by utilizing two parallel beams tuned with MBs' resonance frequency. Quantitative and qualitative results confirm the separability of the two MBs populations. As a next step, we plan to test *in vivo* the proposed approach, thus testing the performance of the proposed approach in high MBs concentrations scenarios.

Chapter 6

Conclusion

This chapter presents the conclusions of the research carried out as part of this PhD and summarizes the results presented in this thesis. In addition, it proposes potential future research directions for further development of the proposed methods.

6.1 Final Discussion

Clinically, ULM holds promise as a powerful tool for the monitoring, diagnosing, and delivering follow up treatment of vascular-related pathologies. Moreover, it offers the potential to enhance our understanding of vascular function and to establish correlations between vascular alterations and disease mechanisms. Despite these promising prospect, ULM clinical implementation remains limited by several technical and practical challenges, including the need for high FRs, prolonged acquisition times, and the absence of validation tools [30, 70, 73]. This thesis proposes solutions to these limitations.

The impact of FR on ULM performance has been extensively discussed in the literature [79, 80]. Although a limited number of studies have attempted to apply ULM at FRs typical of clinical ultrasound scanners (i.e., sub-100 Hz), such low FRs are primarily effective for tracking slow-moving MBs. This results in the loss of information regarding faster flows, as the FR is insufficient to capture rapid changes in the MB trajectories. To alleviate the high FR need, Ackerman et al. and Opacic et al. [61, 63] proposed a modified Markov chain Monte Carlo data association. This method optimally associates MB positions by incorporating an underlying motion model, thus facilitating the tracking of MBs even at lower FRs. Similarly, Jeffries et al. [60] employed a Kalman filter as the tracking backbone, integrating MB image features to improve tracking accuracy. While these approaches enable the recovery of MB trajectories at FRs as low as approximately 50 Hz, the performance comes at the price of high computational cost. In this regard and to relax the high FR constraint, we propose in Chapters 2 and 3 the use of RBF interpolators. Chapter 2 presents TEULM, a modified ULM framework capable of handling low FR data acquisition. The RBF interpolation utilize the spatio-temporal information to synthetically upsample low FR data. As such, TEULM improves tracking capabilities. Our results demonstrate that TEULM significantly enhances the visualization of vascular

structures, even with FRs as low as 100 Hz. The method produces comparable density maps across a range of organs and pathologies, showcasing its effectiveness in clinical scenarios with limited FR capabilities.

However, it is important to note that TEULM's ability to recover velocity information is less robust compared to its success in depicting vascular morphology.

As an extension of the work presented in Chapter 2, where the interpolation is applied along a single x-t plane, Chapter 3 proposes the use of RBF interpolator along 2 orthogonal planes (x-t and z-t). The core idea behind this study resides in the fact that MBs move within the vasculature, creating complex spatiotemporal signals that can be difficult to capture with single-plane interpolation. Integrating the interpolation results from two orthogonal spatiotemporal planes provides a more accurate and robust reconstruction of MBs trajectories. This technique is tested on publicly available datasets with the aim of relaxing the constraints associated with high FRs. The study demonstrates that the proposed method not only improves the recovery of structural information, but also enables a more accurate depiction of dynamic vascular parameters at a FR as low as 100 Hz. In addition to improving FR limitations, we also evaluate the impact of reduced acquisition times. Specifically, we assess the quality of vascular depiction and velocity estimation when the data is acquired in as little as 1/4 of the time typically required for a standard ULM acquisition. Our results indicate that the proposed method allows for a reduction in acquisition times by a factor of 4, while still producing comparable results in terms of both structural imaging and dynamic velocity estimates when compared to longer acquisition scenarios.

Another main concern for the clinical application of ULM is the acquisition time required to achieve a complete microvessel image. To fully reconstruct the microvasculature, it is essential that each capillary is perfused by at least one MB. Previous studies have demonstrated that, for imaging of a rat brain, 10 mins are required to achieve adequate perfusion and coverage [80]. In a clinical setting, this acquisition time would likely elongate. However, the measurement duration in clinical context should balance considerations such as patient comfort, volume of data generated and computational resources required to process such data. As a result, a compromise between acquisition time and degree of reconstruction needs to be established.

Various research groups conducted extensive research to shorten the acquisition times. One straightforward approach is to increase the number of injected MBs [64]. However, high MB concentrations often results in overlapping MB signals, making it difficult to distinguish individual MB echoes and accurately localize them. To address this challenge, several methods have been proposed, including sparse recovery [65, 76], deconvolution [131] and velocity filtering [132]. Additionally, in [69] Huang at al. proposes to define different sub-populations based on the different flow dynamics to separate overlapping MBs signal. However, all the aforementioned techniques rely on ultra-fast plane wave imaging, which is out of the reach for most clinical systems.

In Chapters 4 and 5, we introduce a bi-disperse MB population (i.e. composed of two well-separated monodisperse MB populations). By uncoupling this population, we aim

at increasing MB concentrations, thus potentially reducing acquisition times. Chapter 4 introduces an uncoupling technique based on the distinct frequency responses of the two monodisperse MB populations. Specifically, we adjust the transmission frequency to match the resonance frequency of one of the MB populations. This results in a higher nonlinear response from the population whose resonance frequency aligns with the transmission frequency, while the other population (with a non-matching resonance frequency) exhibits a mainly linear response. This uncoupling technique is tested using a 3D-printed phantom, where the two MB populations are injected both individually and simultaneously. The individual injections allow for testing the cross-talk between the two populations, while the simultaneous injection provides a more realistic scenario. The results demonstrate that the proposed technique is effective in uncoupling the bi-disperse MB populations, potentially allowing for higher MB concentrations without signal overlap. This approach has the potential to significantly reduce acquisition times while maintaining high-quality imaging.

In Chapter 5 we present another uncoupling strategy using the same bi-disperse MB population as the one presented in 4. This uncoupling relies on OFDM. OFDM transmits parallel pulses at different transmission frequencies. The idea here is that each MB population will respond differently when insonified with beams at different frequencies. In particular, a MB excited with a beam tuned with the resonance frequency would have a stronger response. By evaluating the PSF of each MB acquired at their respective resonance frequency, we develop an algorithm able to assign each MB detection to one of the two populations. We test the approach in an *in vitro* phantom when injecting the two populations simultaneously, each in one channel. Results validate the proposed uncoupling approach. As in chapter 4 the possibility to uncouple the bi-disperse population allows to increase MB concentrations, thus potentially decreasing acquisition times.

The development of methods or tools for evaluating the density and dynamic maps generated by ULM is crucial for utilizing these images in clinical practice. In this context, we initiated a collaboration with the PROM Facility at Trentino Sviluppo, Rovereto, Italy. The facility's 3D printing capabilities allow the creation of vascular structures, thus providing a valuable ground truth for ULM-based imaging.

Printing microvascular structures presents several challenges. First, it is essential to select an appropriate printing technique and material capable of supporting complex, hollow structures. Second, the material must be ultrasound-compatible, ensuring that it generates a sufficiently strong backscattered signal to allow for the detection of moving MBs and, consequently, for effective ultrasound imaging. Third, the material must be robust enough to prevent structural collapse during the printing process.

To address these challenges, we selected the Sintering Laser Technique as the printing method. This technique utilizes the heat produced by a laser source to selectively heat the polymer at specific locations, thereby enabling the layer-by-layer construction of 3D solid structures at sub-millimetric resolution. The material used for printing the 3D vascular phantom, Flexa TPU (with an elastic modulus of 76 MPa and a density of 1.04 g/cm^3), was chosen for its compatibility with ultrasound imaging.

The 3D printed vascular phantom was employed in the study presented in Chapter 4, demonstrating the feasibility of producing ultrasound-compatible vascular structures via 3D printing. This approach opens the door to the use of realistic, reproducible phantoms for validating and refining ULM techniques.

The limitations of the methods proposed in this thesis are:

1. The methods proposed in the thesis have not been tested on *in vivo* clinical data. The proposed algorithms have been tested on pre-clinical *in vivo* or *in vitro* data from either publicly available dataset or acquiring the data ourselves. Although testing the methods with pre-clinical *in vivo* and *in vitro* data is a natural step in the research process, validation with clinical *in vivo* data is fundamental for ULM clinical translation.

2. Motion correction is not addressed in this thesis. However, to image the vasculature, ULM required acquisition spanning over tens of minutes. Over this time, tissue motion (e.g. breathing, hand motions due to human held US probe) might importantly affect the data acquired [39, 133, 134]. If not corrected, tissue motion leads to loss in resolution by motion blur and misleading reconstructions [75]. The data used in this thesis are acquired ensuring little movements. While motion within of the data utilized in this thesis can be considered negligible, motion compensation plays a crucial role and is of fundamental importance.

3. 3D ULM is not considered in this work, yet it represents a natural and essential progression for ULM. The incorporation of the third dimension addresses several inherent limitations of 2D ULM. Specifically, 3D ULM enables the detection and localization of MBs in three spatial dimensions, thereby facilitating a more comprehensive visualization of the vascular volume. Moreover, 3D imaging helps mitigate the issue of localization overlap, which often arises due to the projection of a dense MB cloud in 2D. Additionally, 3D ULM offers improvements in tracking accuracy, as the third dimension reduces the likelihood of erroneous MB pairings that can occur with 2D acquisitions. Finally, 3D imaging provides a more effective means of compensating for out-of-plane tissue motion, further enhancing the reliability of ULM in dynamic imaging scenarios.

6.2 Future Work

In the immediate future, the author proposes an extension of the research carried out in this thesis as follows:

1. Applying the RBF-interpolation for reduced FR and decreased acquisition times in 3D dataset.

2. Applying the interpolation technique for reduced FR and reduced acquisition time on data acquired in a more challenging scenario and close to the clinical context (e.g. with motion).

3. Validation of all the proposed methods on *in vivo* clinical data.

4. An extension of the study on the bi-disperse MB population involves injecting a mixture of the two monodisperse populations, rather than performing injections either individually or simultaneously. This next step is crucial not only for validating the uncoupling performance of the proposed algorithms but also for investigating the feasibility of increasing MB concentrations. By mixing the two populations, we can assess the effectiveness of the uncoupling technique in real-world scenarios, where overlapping MB signals are more likely to occur. Moreover, this approach will provide valuable insights into the potential for enhancing MB concentrations without compromising the accuracy of signal localization, ultimately contributing to improved imaging quality while reducing acquisition times.

5. 3D print vascular structures of a full organ. We aim at printing different organs' vasculature both healthy and featuring pathological vascular conditions. This would allow to have a controllable tool to perform experiment and validate ULM algorithms for vascular imaging.

From its invention in 2011, ULM has been considered as a revolutionary technique for microvascular imaging. To validate its potential, the technique has been applied to various use cases both in preclinical and clinical studies. However, it is still not integrated in clinical practice. This thesis focused on investigating and understanding some requirements and constraints of ULM, which are preventing the technique to be implemented as a routine exam. This thesis successfully addressed key challenges such as high FRs, long acquisition times, and 3D printing a vascular phantom for validation. Incorporating the proposed solutions into ULM may accelerate its adoption in routine clinical practice. However, an important unanswered question remains regarding the clinical application of ULM: has its optimal use case been identified? Defining this would provide a critical drive force for its integration into routine clinical practice.

List of Publications

INTERNATIONAL JOURNALS

[J0] **Tuccio G.**, Afrakhteh S., Iacca G., Demi L., "Time Efficient Ultrasound Localization Microscopy Based on A Novel Radial Basis Function 2D Interpolation" in *IEEE Transactions on medical imaging* 2024

[J1] Afrakhteh S., **Tuccio G.**, Demi L., "A Novel 2x2D Radial Basis Functions-based Interpolation for Short Acquisition Time and Relaxed Frame Rate Ultrasound Localization Microscopy" In *IEEE transactions on ultrasonics ferroelectric and frequency control*, 2024

[J2] **Tuccio, G.**, Te Winkel L., Bruggeman C., Van Hoeve W., Demi L., "Towards reduced ULM acquisition times by uncoupling a bi-disperse microbubble population", In review, 2025

INTERNATIONAL CONFERENCE PROCEEDINGS

[CP1] **Tuccio, G.**, Te Winkel L., Bruggeman C., Van Hoeve W., Demi L., "Stability of a bi-disperse microbubble population for advanced Ultrasound Localization Microscopy", in *IEEE International Ultrasonics Symposium*, 2025

[CP2] Giaccone L., **Tuccio, G.**, Demi L., "Detection of pulsatile oscillations via ultrasound localization microscopy", in *IEEE International Ultrasonics Symposium*, 2025

[CP3] Giaccone L., **Tuccio, G.**, Demi L., "Physics-informed channel modeling with ultrasound localization microscopy: reconstructing geometry and flow field from sparse velocity measurements", in *IEEE International Ultrasonics Symposium*, 2025

[CP4] **Tuccio G.**, Te Winkel L., Bruggeman C., Van Hoeve W., Demi L., "Increasing Microbubble Concentrations in Microvascular Imaging via Microbubble Separation by means of Orthogonal Frequency Division Multiplexing" in *IEEE Ultrasonics, Ferroelectrics, and Frequency Control Joint Symposium, UFFC-JS*, 2024

[CP5] **Tuccio G.**, Te Winkel L., Bruggeman C., Van Hoeve W., Demi L., "Ultrasound Localization Microscopy Imaging by Monodisperse Microbubble Uncoupling: First Experimental Study" in *IEEE Ultrasonics, Ferroelectrics, and Frequency Control Joint Symposium, UFFC-JS*, 2024

[CP6] **Tuccio G.**, Afrakhteh S., Demi L., "Towards sub-100Hz Super-Resolution Imaging Through a Novel Bi-Directional Interpolation Technique" in *IEEE Ultrasonics, Ferroelectrics, and Frequency Control Joint Symposium, UFFC-JS*, 2024

[CP7] **Tuccio G.**, Afrakhteh S., Iacca G., Demi L., "Relaxing Super Localization Frame Rate Requirements Utilizing a Novel 2D Interpolation Technique" in *IEEE International Ultrasonics Symposium*, 2023

INTERNATIONAL CONFERENCE ABSTRACTS

[CA1] **Tuccio, G.**, Te Winkel, Bruggeman C, Van Hoeve W, Demi L., "Uncoupling a bi-disperse microbubble population for decreased ULM acquisition times: a proof-of-concept study" in *Acoustical Society of America*, 2025

[CA2] **Tuccio G.**, Afrakhteh S., Demi L., "Ultrasound Localization Microscopy with Reduced Frame Rates and Short Acquisition Times Using Bidirectional 2D Interpolation", in *Acoustical Society of America*, 2025

[CA3] **Tuccio G.**, Afrakhteh S., Demi L., "A parametrization study of TEULM's image reconstruction performance" in *Acoustical Society of America*, 2024

[CA4] **Tuccio, G.**, Te Winkel L., Bruggeman C., Van Hoeve W., Demi L., "Towards reduced ultrasound localization microscopy acquisition time by means of monodisperse microbubbles uncoupling", in *Acoustical Society of America*, 2024

[CA5] **Tuccio G.**, Afrakhteh S., Demi L., "Super-Resolution Imaging at sub-100 Hz frame rates by means of a Novel Radial Basis Interpolation Technique". in *South Asia Ultrasonics Simposium (SAUS)*, 2024

Bibliography

[1] M. P. Wiedeman, "Dimensions of blood vessels from distributing artery to collecting vein," *Circ. Res.*, vol. 12, no. 4, pp. 375–378, Apr. 1963.

[2] B. M. Carlson, "Chapter 10 - the circulatory system," in *The Human Body*, B. M. Carlson, Ed. Academic Press, 2019, pp. 271–301. [Online]. Available: https://www.sciencedirect.com/science/article/pii/B9780128042540000107

[3] J. Feher, *Quantitative human physiology*. Academic Press, 2017.

[4] F. Lin, S. E. Shelton, D. Espíndola, J. D. Rojas, G. Pinton, and P. A. Dayton, "3-d ultrasound localization microscopy for identifying microvascular morphology features of tumor angiogenesis at a resolution beyond the diffraction limit of conventional ultrasound," *Theranostics*, vol. 7, no. 1, p. 196, 2017.

[5] W. H. Organization, *WHO report on cancer: setting priorities, investing wisely and providing care for all*. World Health Organization, 2020.

[6] E. M. Paleolog, "The vasculature in rheumatoid arthritis: cause or consequence?" *International journal of experimental pathology*, vol. 90, no. 3, pp. 249–261, 2009.

[7] M. J. Mulligan-Kehoe and M. Simons, "Vasa vasorum in normal and diseased arteries," *Circulation*, vol. 129, no. 24, pp. 2557–2566, 2014.

[8] R. Seddiki, T. Mirault, J. Sitruk, N. Mohamedi, E. Messas, M. Pernot, J. Baranger, and G. Goudot, "Advancements in noncontrast ultrasound imaging for low-velocity flow: A technical review and clinical applications in vascular medicine," *Ultrasound in Medicine & Biology*, vol. 51, no. 7, pp. 1035–1042, 2025. [Online]. Available: https://www.sciencedirect.com/science/article/pii/S0301562925000699

[9] B. Beliard, C. Ahmanna, E. Tiran, K. Kanté, T. Deffieux, M. Tanter, F. Nothias, S. Soares, and S. Pezet, "Ultrafast doppler imaging and ultrasound localization microscopy reveal the complexity of vascular rearrangement in chronic spinal lesion," *Scientific Reports*, vol. 12, no. 1, p. 6574, 2022.

[10] J. Bábíčková, B. M. Klinkhammer, E. M. Buhl, S. Djudjaj, M. Hoss, F. Heymann, F. Tacke, J. Floege, J. U. Becker, and P. Boor, "Regardless of etiology, progressive renal disease causes ultrastructural and functional alterations of peritubular capillaries," *Kidney international*, vol. 91, no. 1, pp. 70–85, 2017.

[11] D. Ghosh, J. Peng, K. Brown, S. Sirsi, C. Mineo, P. W. Shaul, and K. Hoyt, "Super-resolution ultrasound imaging of skeletal muscle microvascular dysfunction in an animal model of type 2 diabetes," *Journal of Ultrasound in Medicine*, vol. 38, no. 10, pp. 2589–2599, 2019.

[12] L. Pantoni, "Cerebral small vessel disease: from pathogenesis and clinical characteristics to therapeutic challenges," *The Lancet Neurology*, vol. 9, no. 7, pp. 689–701, 2010.

[13] P. B. Gorelick, A. Scuteri, S. E. Black, C. DeCarli, S. M. Greenberg, C. Iadecola, L. J. Launer, S. Laurent, O. L. Lopez, D. Nyenhuis *et al.*, "Vascular contributions to cognitive impairment and dementia: a statement for healthcare professionals from the american heart association/american stroke association," *stroke*, vol. 42, no. 9, pp. 2672–2713, 2011.

[14] S. Dencks and G. Schmitz, "Ultrasound localization microscopy," *Zeitschrift für Medizinische Physik*, vol. 33, no. 3, pp. 292–308, 2023, special Issue: Recent Advances in Ultrasound Imaging. [Online]. Available: https://www.sciencedirect.com/science/article/pii/S0939388923000302

[15] S. Kos, R. Huegli, G. M. Bongartz, A. L. Jacob, and D. Bilecen, "Mr-guided endovascular interventions: a comprehensive review on techniques and applications," *European Radiology*, vol. 18, no. 4, p. 645–657,

Dec. 2007. [Online]. Available: http://dx.doi.org/10.1007/s00330-007-0818-4

[16] A. H. Kuo, P. Nagpal, B. B. Ghoshhajra, and S. S. Hedgire, "Vascular magnetic resonance angiography techniques," *Cardiovascular Diagnosis and Therapy*, vol. 9, no. S1, p. S28–S36, Aug. 2019. [Online]. Available: http://dx.doi.org/10.21037/cdt.2019.06.07

[17] J. Leary and J. Key, "Nanoparticles for multimodal in vivo imaging in nanomedicine," *International Journal of Nanomedicine*, p. 711, Jan. 2014. [Online]. Available: http://dx.doi.org/10.2147/IJN.S53717

[18] D. L. Alessandro and D. J. Orlando, *MR Angiogram*. StatsPearls Pulishing, 2025.

[19] V. Baliyan, K. Shaqdan, S. Hedgire, and B. Ghoshhajra, "Vascular computed tomography angiography technique and indications," *Cardiovascular Diagnosis and Therapy*, vol. 9, no. S1, p. S14–S27, Aug. 2019. [Online]. Available: http://dx.doi.org/10.21037/cdt.2019.07.04

[20] S. Culleton, R. Wiggins, and J. S. McNally, "Imaging spectrum of extracranial arterial vascular pathology: pearls for the radiologist," *Clin. Radiol.*, vol. 77, no. 3, pp. 167–178, Mar. 2022.

[21] P. K. Upputuri, K. Sivasubramanian, C. S. K. Mark, and M. Pramanik, "Recent developments in vascular imaging techniques in tissue engineering and regenerative medicine," *BioMed Research International*, vol. 2015, p. 1–9, 2015. [Online]. Available: http://dx.doi.org/10.1155/2015/783983

[22] ——, "Recent developments in vascular imaging techniques in tissue engineering and regenerative medicine," *Biomed Res. Int.*, vol. 2015, p. 783983, Mar. 2015.

[23] J. Goddard, G. Buurma, and D. C. Fuller, *Ultrasound physics and Instrumentation*. Society of Diagnostic Medical Sonographers, 1990.

[24] S. Kunjachan, J. Ehling, G. Storm, F. Kiessling, and T. Lammers, "Noninvasive imaging of nanomedicines and nanotheranostics: Principles, progress, and prospects," *Chemical Reviews*, vol. 115, no. 19, p. 10907–10937, Jul. 2015. [Online]. Available: http://dx.doi.org/10.1021/cr500314d

[25] A. Ng and J. Swanevelder, "Resolution in ultrasound imaging," *Continuing Education in Anaesthesia Critical Care and Pain*, vol. 11, no. 5, p. 186–192, Oct. 2011. [Online]. Available: http://dx.doi.org/10.1093/bjaceaccp/mkr030

[26] K. Christensen-Jeffries, O. Couture, P. Dayton, Y. Eldar, K. Hynynen, F. Kiessling, M. O'Reilly, G. Pinton, G. Schmitz, M.-X. Tang, M. Tanter, and R. van Sloun, "Super-resolution ultrasound imaging," *Ultrasound in Medicine and Biology*, vol. 46, 01 2020.

[27] H. Cho, J. Lee, S. Park, and Y. Yoo, "Numerical investigation of optimal transmission-reception conditions for aliasing-free ultrasound localization microscopy," *Ultrasonics*, vol. 154, p. 107704, Oct. 2025. [Online]. Available: http://dx.doi.org/10.1016/j.ultras.2025.107704

[28] B. W. Drinkwater and P. D. Wilcox, "Ultrasonic arrays for non-destructive evaluation: A review," *NDT & E International*, vol. 39, no. 7, p. 525–541, Oct. 2006. [Online]. Available: http://dx.doi.org/10.1016/j.ndteint.2006.03.006

[29] D. Guenther and W. Walker, "Generalized cystic resolution: a metric for assessing the fundamental limits on beamformer performance," *IEEE Transactions on Ultrasonics, Ferroelectrics and Frequency Control*, vol. 56, no. 1, p. 77–90, Jan. 2009. [Online]. Available: http://dx.doi.org/10.1109/TUFFC.2009.1007

[30] P. Song, J. M. Rubin, and M. R. Lowerison, "Super-resolution ultrasound microvascular imaging: Is it ready for clinical use?" *Zeitschrift für Medizinische Physik*, vol. 33, no. 3, pp. 309–323, 2023, special Issue: Recent Advances in Ultrasound Imaging. [Online]. Available: https://www.sciencedirect.com/science/article/pii/S0939388923000430

[31] G. Montaldo, M. Tanter, J. Bercoff, N. Benech, and M. Fink, "Coherent plane-wave compounding for very high frame rate ultrasonography and transient elastography," *IEEE Transactions on Ultrasonics, Ferroelectrics, and Frequency Control*, vol. 56, no. 3, pp. 489–506, 2009.

[32] M. Tanter and M. Fink, "Ultrafast imaging in biomedical ultrasound," *IEEE transactions on ultrasonics, ferroelectrics, and frequency control*, vol. 61, no. 1, pp. 102–119, 2014.

[33] Q. You, M. R. Lowerison, Y. Shin, X. Chen, N. V. C. Sekaran, Z. Dong, D. A. Llano, M. A. Anastasio, and P. Song, "Contrast-free super-resolution power doppler (cs-pd) based on deep neural networks," *IEEE Transactions on Ultrasonics, Ferroelectrics, and Frequency Control*, vol. 70, no. 10, p. 1355–1368, Oct.

2023. [Online]. Available: http://dx.doi.org/10.1109/TUFFC.2023.3304527

[34] M.-X. Tang, H. Mulvana, T. Gauthier, A. Lim, D. Cosgrove, R. Eckersley, and E. Stride, "Quantitative contrast-enhanced ultrasound imaging: a review of sources of variability," *Interface focus*, vol. 1, no. 4, pp. 520–539, 2011.

[35] D. B. Erlichman, A. Weiss, M. Koenigsberg, and M. W. Stein, "Contrast enhanced ultrasound: A review of radiology applications," *Clinical Imaging*, vol. 60, no. 2, pp. 209–215, 2020. [Online]. Available: https://www.sciencedirect.com/science/article/pii/S0899707119302797

[36] G. Gu, X. Zhang, J. Shen, S. Gulidanna, Q. Gao, J. Shao, B. Liu, B. Zhang, and Y. Zheng, "Comparison of contrast-enhanced ultrasonography to color doppler ultrasound in evaluation of carotid body tumors," *Front. Oncol.*, vol. 12, p. 872890, Apr. 2022.

[37] S. W. Hell and J. Wichmann, "Breaking the diffraction resolution limit by stimulated emission: stimulated-emission-depletion fluorescence microscopy," *Optics letters*, vol. 19, no. 11, pp. 780–782, 1994.

[38] O. Couture, B. Besson, G. Montaldo, M. Fink, and M. Tanter, "Microbubble ultrasound super-localization imaging (musli)," in *2011 IEEE International Ultrasonics Symposium*. IEEE, 2011, pp. 1285–1287.

[39] C. Errico, J. Pierre, S. Pezet, Y. Desailly, Z. Lenkei, O. Couture, and M. Tanter, "Ultrafast ultrasound localization microscopy for deep super-resolution vascular imaging," *Nature*, vol. 527, no. 7579, pp. 499–502, 2015.

[40] K. Christensen-Jeffries, O. Couture, P. A. Dayton, Y. C. Eldar, K. Hynynen, F. Kiessling, M. O'Reilly, G. F. Pinton, G. Schmitz, M.-X. Tang *et al.*, "Super-resolution ultrasound imaging," *Ultrasound in medicine & biology*, vol. 46, no. 4, pp. 865–891, 2020.

[41] N. Renaudin, C. Demené, A. Dizeux, N. Ialy-Radio, S. Pezet, and M. Tanter, "Functional ultrasound localization microscopy reveals brain-wide neurovascular activity on a microscopic scale," *Nature methods*, vol. 19, no. 8, pp. 1004–1012, 2022.

[42] C. Demené, J. Robin, A. Dizeux, B. Heiles, M. Pernot, M. Tanter, and F. Perren, "Transcranial ultrafast ultrasound localization microscopy of brain vasculature in patients," *Nature biomedical engineering*, vol. 5, no. 3, pp. 219–228, 2021.

[43] M. R. Lowerison, N. V. C. Sekaran, Z. Dong, X. Chen, Q. You, D. A. Llano, and P. Song, "Super-resolution ultrasound reveals cerebrovascular impairment in a mouse model of alzheimer's disease," *Journal of Neuroscience*, vol. 44, no. 9, 2024.

[44] O. Demeulenaere, Z. Sandoval, P. Mateo, A. Dizeux, O. Villemain, R. Gallet, B. Ghaleh, T. Deffieux, C. Deméné, M. Tanter *et al.*, "Coronary flow assessment using 3-dimensional ultrafast ultrasound localization microscopy," *Cardiovascular Imaging*, vol. 15, no. 7, pp. 1193–1208, 2022.

[45] M. A. Averkiou, M. F. Bruce, J. E. Powers, P. S. Sheeran, and P. N. Burns, "Imaging methods for ultrasound contrast agents," *Ultrasound in medicine & biology*, vol. 46, no. 3, pp. 498–517, 2020.

[46] M. Versluis, E. Stride, G. Lajoinie, B. Dollet, and T. Segers, "Ultrasound contrast agent modeling: a review," *Ultrasound in medicine & biology*, vol. 46, no. 9, pp. 2117–2144, 2020.

[47] J. R. Lindner, "Microbubbles in medical imaging: current applications and future directions," *Nature reviews Drug discovery*, vol. 3, no. 6, pp. 527–533, 2004.

[48] M. Emmer, H. J. Vos, D. E. Goertz, A. van Wamel, M. Versluis, and N. de Jong, "Pressure-dependent attenuation and scattering of phospholipid-coated microbubbles at low acoustic pressures," *Ultrasound in medicine & biology*, vol. 35, no. 1, pp. 102–111, 2009.

[49] A. Sojahrood, Q. Li, H. Haghi, R. Karshafian, T. Porter, and M. Kolios, "Probing the pressure dependence of sound speed and attenuation in bubbly media: Experimental observations, a theoretical model and numerical calculations," *Ultrasonics Sonochemistry*, vol. 95, p. 106319, 2023.

[50] A. Helbert, E. Gaud, T. Segers, C. Botteron, P. Frinking, and V. Jeannot, "Monodisperse versus polydisperse ultrasound contrast agents: In vivo sensitivity and safety in rat and pig," *Ultrasound in Medicine & Biology*, vol. 46, no. 12, pp. 3339–3352, 2020.

[51] T. Segers, P. Kruizinga, M. P. Kok, G. Lajoinie, N. De Jong, and M. Versluis, "Monodisperse versus polydisperse ultrasound contrast agents: non-linear response, sensitivity, and deep tissue imaging potential,"

Ultrasound in medicine & biology, vol. 44, no. 7, pp. 1482–1492, 2018.

[52] B. van Elburg, J. Deprez, M. van den Broek, S. C. De Smedt, M. Versluis, G. Lajoinie, I. Lentacker, and T. Segers, "Dependence of sonoporation efficiency on microbubble size: An in vitro monodisperse microbubble study," *Journal of Controlled Release*, vol. 363, pp. 747–755, 2023.

[53] S. Dencks and G. Schmitz, "Ultrasound localization microscopy," *Zeitschrift für Medizinische Physik*, vol. 33, no. 3, pp. 292–308, 2023, special Issue: Recent Advances in Ultrasound Imaging. [Online]. Available: https://www.sciencedirect.com/science/article/pii/S0939388923000302

[54] Y. Desailly, J. Pierre, O. Couture, and M. Tanter, "Resolution limits of ultrafast ultrasound localization microscopy," *Physics in medicine and biology*, vol. 60, no. 22, p. 8723, 2015.

[55] Y. Desailly, O. Couture, M. Fink, and M. Tanter, "Sono-activated ultrasound localization microscopy," *Applied Physics Letters*, vol. 103, no. 17, 2013.

[56] C. Demené, T. Deffieux, M. Pernot, B.-F. Osmanski, V. Biran, S. Franchi-Abella, J.-M. Correas, I. Cohen, O. Baud, and M. Tanter, "Spatiotemporal clutter filtering of ultrafast ultrasound data highly increases doppler and fultrasound sensitivity," *IEEE transactions on medical imaging*, vol. 34, 04 2015.

[57] B. Heiles, A. Chavignon, V. Hingot, P. Lopez, E. Teston, and O. Couture, "Performance benchmarking of microbubble-localization algorithms for ultrasound localization microscopy," *Nature Biomedical Engineering*, vol. 6, 05 2022.

[58] Y. Desailly, O. Couture, M. Fink, and M. Tanter, "Sono-activated ultrasound localization microscopy," *Applied Physics Letters*, vol. 103, no. 17, Oct. 2013. [Online]. Available: http://dx.doi.org/10.1063/1.4826597

[59] M. Lowerison, X. Chen, C. Huang, W. Zhang, S. Tang, N. C. Sekaran, D. Llano, S. Chen, and P. Song, "Multi-resolution data processing for accelerated and robust ultrasound localization microscopy," in *2020 IEEE International Ultrasonics Symposium (IUS)*. IEEE, Sep. 2020, p. 1–4. [Online]. Available: http://dx.doi.org/10.1109/IUS46767.2020.9251757

[60] J. Yan, T. Zhang, J. Broughton-Venner, P. Huang, and M.-X. Tang, "Super-resolution ultrasound through sparsity-based deconvolution and multi-feature tracking," *IEEE Transactions on Medical Imaging*, vol. PP, pp. 1–1, 02 2022.

[61] T. Opacic, S. Dencks, B. Theek, M. Schulte, D. Ackermann, A. Rix, T. Lammers, E. Stickeler, S. Delorme, G. Schmitz, and F. Kiessling, "Motion model ultrasound localization microscopy for preclinical and clinical multiparametric tumor characterization," *Nature Communications*, vol. 9, 04 2018.

[62] O. Viessmann, R. Eckersley, K. Christensen-Jeffries, M.-X. Tang, and C. Dunsby, "Acoustic super-resolution with ultrasound and microbubbles," *Physics in Medicine & Biology*, vol. 58, no. 18, p. 6447, 2013.

[63] D. Ackermann and G. Schmitz, "Detection and tracking of multiple microbubbles in ultrasound b-mode images," *IEEE Transactions on Ultrasonics, Ferroelectrics, and Frequency Control*, vol. 63, pp. 1–1, 11 2015.

[64] R. J. G. van Sloun, O. Solomon, M. Bruce, Z. Z. Khaing, H. Wijkstra, Y. C. Eldar, and M. Mischi, "Super-resolution ultrasound localization microscopy through deep learning," *IEEE Transactions on Medical Imaging*, vol. 40, no. 3, pp. 829–839, 2021.

[65] A. D. Bar-Zion, O. Solomon, C. Tremblay-Darveau, D. R. Adam, and Y. C. Eldar, "Sushi: Sparsity-based ultrasound super-resolution hemodynamic imaging," *IEEE Transactions on Ultrasonics, Ferroelectrics, and Frequency Control*, vol. 65, pp. 2365–2380, 2017.

[66] L. Milecki, J. Porée, H. Belgharbi, C. Bourquin, R. Damseh, P. Delafontaine-Martel, F. Lesage, M. Gasse, and J. Provost, "A deep learning framework for spatiotemporal ultrasound localization microscopy," *IEEE Transactions on Medical Imaging*, vol. PP, pp. 1–1, 02 2021.

[67] A. Bar-Zion, C. Tremblay-Darveau, O. Solomon, D. Adam, and Y. C. Eldar, "Fast vascular ultrasound imaging with enhanced spatial resolution and background rejection," *IEEE transactions on medical imaging*, vol. 36, no. 1, pp. 169–180, 2016.

[68] X. Chen, M. R. Lowerison, Z. Dong, N. V. C. Sekaran, D. A. Llano, and P. Song, "Localization free super-resolution microbubble velocimetry using a long short-term memory neural network," *IEEE transactions on medical imaging*, vol. 42, no. 8, pp. 2374–2385, 2023.

[69] C. Huang, M. Lowerison, J. Trzasko, A. Manduca, Y. Bresler, S. Tang, P. Gong, U. W. Lok, P. Song, and S. Chen, "Short acquisition time super-resolution ultrasound microvessel imaging via microbubble separation," *Scientific Reports*, vol. 10, 04 2020.

[70] J. Kim, M. R. Lowerison, N. V. C. Sekaran, Z. Kou, Z. Dong, M. L. Oelze, D. A. Llano, and P. Song, "Improved ultrasound localization microscopy based on microbubble uncoupling via transmit excitation," *IEEE transactions on ultrasonics, ferroelectrics, and frequency control*, vol. 69, no. 3, pp. 1041–1052, 2022.

[71] H. W. Kuhn, "The hungarian method for the assignment problem," *Naval Research Logistics (NRL)*, vol. 52, no. 1, pp. 7–21, 2005.

[72] S. Tang, P. Song, J. Trzasko, M. Lowerison, C. Huang, P. Gong, U. W. Lok, A. Manduca, and S. Chen, "Kalman filter–based microbubble tracking for robust super-resolution ultrasound microvessel imaging," *IEEE Transactions on Ultrasonics, Ferroelectrics, and Frequency Control*, vol. PP, pp. 1–1, 03 2020.

[73] C. Errico, J. Pierre, S. Pezet, Y. Desailly, Z. Lenkei, O. Couture, and M. Tanter, "Ultrafast ultrasound localization microscopy for deep super-resolution vascular imaging," *Nature*, vol. 527, 11 2015.

[74] P. Cormier, J. Poree, C. Bourquin, and J. Provost, "Dynamic myocardial ultrasound localization angiography," *IEEE Transactions on Medical Imaging*, vol. 40, no. 12, p. 3379–3388, Dec. 2021. [Online]. Available: http://dx.doi.org/10.1109/TMI.2021.3086115

[75] S. Harput, K. Christensen-Jeffries, J. Brown, Y. Li, K. J. Williams, A. H. Davies, R. J. Eckersley, C. Dunsby, and M.-X. Tang, "Two-stage motion correction for super-resolution ultrasound imaging in human lower limb," *IEEE Transactions on Ultrasonics, Ferroelectrics, and Frequency Control*, vol. 65, no. 5, p. 803–814, May 2018. [Online]. Available: http://dx.doi.org/10.1109/tuffc.2018.2824846

[76] O. Solomon, R. J. G. van Sloun, H. Wijkstra, M. Mischi, and Y. C. Eldar, "Exploiting flow dynamics for super-resolution in contrast-enhanced ultrasound," 2018, arXiv:1804.03134.

[77] C. Huang, W. Zhang, P. Gong, U.-W. Lok, S. Tang, T. Yin, X. Zhang, L. Zhu, M. Sang, P. Song, R. Zheng, and S. Chen, "Super-resolution ultrasound localization microscopy based on a high frame-rate clinical ultrasound scanner: an in-human feasibility study," *Physics in Medicine & Biology*, vol. 66, no. 8, p. 08NT01, Apr. 2021. [Online]. Available: http://dx.doi.org/10.1088/1361-6560/abef45

[78] O. Couture, B. Besson, G. Montaldo, M. Fink, and M. Tanter, "Microbubble ultrasound super-localization imaging (musli)," in *2011 IEEE International Ultrasonics Symposium*, 2011, pp. 1285–1287.

[79] X. Guo, D. Ta, and K. Xu, "Frame rate effects and their compensation on super-resolution microvessel imaging using ultrasound localization microscopy," *Ultrasonics*, vol. 132, p. 107009, 2023.

[80] V. Hingot, C. Errico, B. Heiles, L. Rahal, M. Tanter, and O. Couture, "Microvascular flow dictates the compromise between spatial resolution and acquisition time in ultrasound localization microscopy," *Scientific Reports*, vol. 9, 02 2019.

[81] S. Dencks, M. Piepenbrock, T. Opacic, B. Krauspe, E. Stickeler, F. Kiessling, and G. Schmitz, "Clinical pilot application of super-resolution us imaging in breast cancer," *IEEE transactions on ultrasonics, ferroelectrics, and frequency control*, vol. 66, no. 3, pp. 517–526, 2018.

[82] H. Belgharbi, J. Porée, R. Damseh, V. Perrot, L. Milecki, P. Delafontaine-Martel, F. Lesage, and J. Provost, "An anatomically realistic simulation framework for 3d ultrasound localization microscopy," *IEEE Open Journal of Ultrasonics, Ferroelectrics, and Frequency Control*, vol. 3, pp. 1–13, 2023.

[83] A. Linninger, G. Hartung, S. Badr, and R. Morley, "Mathematical synthesis of the cortical circulation for the whole mouse brain-part i. theory and image integration," *Computers in Biology and Medicine*, vol. 110, p. 265–275, Jul. 2019. [Online]. Available: http://dx.doi.org/10.1016/j.compbiomed.2019.05.004

[84] P. Song, J. D. Trzasko, A. Manduca, R. Huang, R. Kadirvel, D. F. Kallmes, and S. Chen, "Improved super-resolution ultrasound microvessel imaging with spatiotemporal nonlocal means filtering and bipartite graph-based microbubble tracking," *IEEE Transactions on Ultrasonics, Ferroelectrics, and Frequency Control*, vol. 65, no. 2, pp. 149–167, 2018.

[85] E. H. Georgoulis, J. Levesley, and F. Subhan, "Multilevel sparse kernel-based interpolation," *SIAM Journal on Scientific Computing*, vol. 35, no. 2, pp. A815–A831, 2013.

[86] H. Jalilian, S. Afrakhteh, G. Iacca, and L. Demi, "Increasing frame rate of echocardiography based on a novel 2d spatio-temporal meshless interpolation," *Ultrasonics*, vol. 131, p. 106953, 2023.

[87] K. Christensen-Jeffries, S. Harput, J. Brown, P. N. T. Wells, P. Aljabar, C. Dunsby, M.-X. Tang, and R. J. Eckersley, "Microbubble axial localization errors in ultrasound super-resolution imaging," *IEEE Transactions on Ultrasonics, Ferroelectrics, and Frequency Control*, vol. 64, no. 11, pp. 1644–1654, 2017.

[88] D. Espindola, R. DeRuiter, F. Santibanez, P. Dayton, and G. Pinton, "Quantitative sub-resolution blood velocity estimation using ultrasound localization microscopy ex-vivo and in-vivo," *Biomedical Physics & Engineering Express*, vol. 6, 03 2020.

[89] Y.-H. Nai, B. W. Teo, N. L. Tan, S. O'Doherty, M. C. Stephenson, Y. L. Thian, E. Chiong, and A. Reilhac, "Comparison of metrics for the evaluation of medical segmentations using prostate mri dataset," *Computers in Biology and Medicine*, vol. 134, p. 104497, 2021.

[90] V. Hingot, A. Chavignon, B. Heiles, and O. Couture, "Measuring image resolution in ultrasound localization microscopy," *IEEE Transactions on Medical Imaging*, vol. 40, no. 12, pp. 3812–3819, 2021.

[91] M. van Heel and M. Schatz, "Fourier shell correlation threshold criteria," *Journal of Structural Biology*, vol. 151, no. 3, pp. 250–262, 2005. [Online]. Available: https://www.sciencedirect.com/science/article/pii/S1047847705001292

[92] W. Saxton and W. Baumeister, "The correlation averaging of a regularly arranged bacterial cell envelope protein," *Journal of microscopy*, vol. 127, no. 2, pp. 127–138, 1982.

[93] P. Song, J. D. Trzasko, A. Manduca, R. Huang, R. Kadirvel, D. F. Kallmes, and S. Chen, "Improved super-resolution ultrasound microvessel imaging with spatiotemporal nonlocal means filtering and bipartite graph-based microbubble tracking," *IEEE transactions on ultrasonics, ferroelectrics, and frequency control*, vol. 65, no. 2, pp. 149–167, 2017.

[94] U.-W. Lok, P. Song, J. D. Trzasko, R. Daigle, E. A. Borisch, C. Huang, P. Gong, S. Tang, W. Ling, and S. Chen, "Real time svd-based clutter filtering using randomized singular value decomposition and spatial downsampling for micro-vessel imaging on a verasonics ultrasound system," *Ultrasonics*, vol. 107, p. 106163, 2020.

[95] Y. Shu, C. Han, M. Lv, and X. Liu, "Fast super-resolution ultrasound imaging with compressed sensing reconstruction method and single plane wave transmission," *IEEE Access*, vol. 6, pp. 39 298–39 306, 2018.

[96] J. Kim, Q. Wang, S. Zhang, and S. Yoon, "Compressed sensing-based super-resolution ultrasound imaging for faster acquisition and high quality images," *IEEE Transactions on Biomedical Engineering*, vol. 68, no. 11, pp. 3317–3326, 2021.

[97] C. Huang, M. R. Lowerison, J. D. Trzasko, A. Manduca, Y. Bresler, S. Tang, P. Gong, U.-W. Lok, P. Song, and S. Chen, "Short acquisition time super-resolution ultrasound microvessel imaging via microbubble separation," *Scientific reports*, vol. 10, no. 1, p. 6007, 2020.

[98] G. Tuccio, S. Afrakhteh, G. Iacca, and L. Demi, "Time efficient ultrasound localization microscopy based on a novel radial basis function 2d interpolation," *IEEE Transactions on Medical Imaging*, 2023.

[99] G. Tuccio , S. Afrakhteh, G. Iacca, and L. Demi, "Relaxing super localization frame rate requirements utilizing a novel 2d interpolation technique," in *2023 IEEE International Ultrasonics Symposium (IUS)*. IEEE, 2023, pp. 1–3.

[100] S. Afrakhteh, G. Iacca, and L. Demi, "A two-dimensional angular interpolation based on radial basis functions for high frame rate ultrafast imaging," *The Journal of the Acoustical Society of America*, vol. 154, no. 5, pp. 3454–3465, 2023.

[101] S. Afrakhteh and H. Behnam, "Coherent plane wave compounding combined with tensor completion applied for ultrafast imaging," *IEEE Transactions on Ultrasonics, Ferroelectrics, and Frequency Control*, vol. 68, no. 10, pp. 3094–3103, 2021.

[102] C. Demené, T. Deffieux, M. Pernot, B.-F. Osmanski, V. Biran, J.-L. Gennisson, L.-A. Sieu, A. Bergel, S. Franqui, J.-M. Correas *et al.*, "Spatiotemporal clutter filtering of ultrafast ultrasound data highly increases doppler and fultrasound sensitivity," *IEEE transactions on medical imaging*, vol. 34, no. 11, pp. 2271–2285, 2015.

[103] B. Heiles, A. Chavignon, V. Hingot, P. Lopez, E. Teston, and O. Couture, "Performance benchmarking of microbubble-localization algorithms for ultrasound localization microscopy," *Nature Biomedical Engineering*, vol. 6, no. 5, pp. 605–616, 2022.

[104] V. Hingot, A. Chavignon, B. Heiles, and O. Couture, "Measuring image resolution in ultrasound localization microscopy," *IEEE transactions on medical imaging*, vol. 40, no. 12, pp. 3812–3819, 2021.

[105] X. Guo, D. Ta, and K. Xu, "Frame rate effects and their compensation on super-resolution microvessel imaging using ultrasound localization microscopy," *Ultrasonics*, vol. 132, p. 107009, 2023.

[106] Y. Li, L. Huang, J. Zhang, C. Huang, S. Chen, and J. Luo, "Localization of high-concentration microbubbles for ultrasound localization microscopy by self-supervised deep learning," in *2021 IEEE International Ultrasonics Symposium (IUS)*, 2021, pp. 1–4.

[107] Y. Shin, M. Lowerison, Y. Wang, X. Chen, Q. You, Z. Dong, M. Anastasio, and P. Song, "Context-aware deep learning enables high-efficacy localization of high concentration microbubbles for super-resolution ultrasound localization microscopy," *Nature Communications*, vol. 15, 04 2024.

[108] R. J. G. van Sloun, O. Solomon, M. Bruce, Z. Z. Khaing, H. Wijkstra, Y. C. Eldar, and M. Mischi, "Super-resolution ultrasound localization microscopy through deep learning," *IEEE Transactions on Medical Imaging*, vol. 40, pp. 829–839, 2018. [Online]. Available: https://api.semanticscholar.org/CorpusID:5035568

[109] M. Lerendegui, K. Riemer, G. Papageorgiou, B. Wang, L. Arthur, A. Chavignon, T. Zhang, O. Couture, P. Huang, A. Md, S. Dencks, C. Dunsby, B. Helfield, J. Jensen, T. Lisson, M. Lowerison, H. Rivaz, A. Samir, G. Schmitz, and M.-X. Tang, "Ultra-sr challenge: Assessment of ultrasound localization and tracking algorithms for super-resolution imaging," *IEEE transactions on medical imaging*, vol. PP, 04 2024.

[110] C. Huang, M. R. Lowerison, J. D. Trzasko, A. Manduca, Y. Bresler, S. Tang, P. Gong, U.-W. Lok, P. Song, and S. Chen, "Short acquisition time super-resolution ultrasound microvessel imaging via microbubble separation," *Scientific reports*, vol. 10, no. 1, p. 6007, 2020.

[111] O. Couture, B. Besson, G. Montaldo, M. Fink, and M. Tanter, "Microbubble ultrasound super-localization imaging (musli)," in *2011 IEEE International Ultrasonics Symposium*. IEEE, 2011, pp. 1285–1287.

[112] M. Siepmann, G. Schmitz, J. Bzyl, M. Palmowski, and F. Kiessling, "Imaging tumor vascularity by tracing single microbubbles," in *2011 IEEE International Ultrasonics Symposium*. IEEE, 2011, pp. 1906–1909.

[113] E. Kanoulas, M. Butler, C. Rowley, V. Voulgaridou, K. Diamantis, W. Duncan, A. Mcneilly, M. Averkiou, H. Wijkstra, M. Mischi, R. Wilson, W. Lu, and V. Sboros, "Super-resolution contrast-enhanced ultrasound methodology for the identification of in vivo vascular dynamics in 2d," *Investigative Radiology*, vol. 54, p. 1, 05 2019.

[114] O. Couture, V. Hingot, B. Heiles, P. Muleki-Seya, and M. Tanter, "Ultrasound localization microscopy and super-resolution: A state of the art," *IEEE transactions on ultrasonics, ferroelectrics, and frequency control*, vol. 65, no. 8, pp. 1304–1320, 2018.

[115] W. van Hoeve, M. de Vargas Serrano, L. te Winkel, F. Forsberg, J. K. Dave, K. Sarkar, C. E. Wessner, and J. R. Eisenbrey, "Improved sensitivity of ultrasound-based subharmonic aided pressure estimation using monodisperse microbubbles," *Journal of Ultrasound in Medicine*, vol. 41, no. 7, pp. 1781–1789, 2022. [Online]. Available: https://onlinelibrary.wiley.com/doi/abs/10.1002/jum.15861

[116] E. Castro-Hernández, W. Hoeve, D. Lohse, and J. Gordillo, "Microbubble generation in a co-flow device operated in a new regime," *Lab on a chip*, vol. 11, pp. 2023–9, 03 2011.

[117] N. de Jong, L. Hoff, T. Skotland, and N. Bom, "Absorption and scatter of encapsulated gas filled microspheres: theoretical considerations and some measurements." *Ultrasonics*, vol. 30 2, pp. 95–103, 1992. [Online]. Available: https://api.semanticscholar.org/CorpusID:29183867

[118] M. B. Kumar, P. Sathiya, and M. Varatharajulu, "Selective laser sintering," *Advances in Additive Manufacturing Processes; China Bentham Books: Beijing, China*, p. 28, 2021.

[119] "Probes — esaote.com," https://www.esaote.com/en-BE/interventional/probes/, [Accessed 10-07-2025].

[120] B. Heiles, A. Chavignon, V. Hingot, P. Lopez, E. Teston, and O. Couture, "Performance benchmarking of microbubble-localization algorithms for ultrasound localization microscopy," *Nature Biomedical Engineering*, vol. 6, 02 2022.

[121] K. Christensen-Jeffries, O. Couture, P. A. Dayton, Y. C. Eldar, K. Hynynen, F. Kiessling, M. O'Reilly, G. F. Pinton, G. Schmitz, M.-X. Tang, M. Tanter, and R. J. van Sloun, "Super-resolution ultrasound imaging," *Ultrasound in Medicine & Biology*, vol. 46, no. 4, pp. 865–891, 2020. [Online]. Available: https://www.sciencedirect.com/science/article/pii/S0301562919315959

[122] P. Song, J. Trzasko, A. Manduca, R. Huang, R. Kadirvel, D. Kallmes, and S. Chen, "Improved super-resolution ultrasound microvessel imaging with spatiotemporal nonlocal means filtering and bipartite graph-based microbubble tracking," *IEEE Transactions on Ultrasonics, Ferroelectrics, and Frequency Control*, vol. PP, pp. 1–1, 11 2017.

[123] H. W. Kuhn, "The hungarian method for the assignment problem," *Naval Research Logistics (NRL)*, vol. 52, no. 1, pp. 7–21, 2005.

[124] J. R. McCall, F. Santibanez, H. Belgharbi, G. F. Pinton, and P. A. Dayton, "Non-invasive transcranial volumetric ultrasound localization microscopy of the rat brain with continuous, high volume-rate acquisition," *Theranostics*, vol. 13, no. 4, p. 1235–1246, 2023. [Online]. Available: http://dx.doi.org/10.7150/thno.79189

[125] S. Dencks and G. Schmitz, "Ultrasound localization microscopy," *Zeitschrift für Medizinische Physik*, vol. 33, no. 3, pp. 292–308, 2023, special Issue: Recent Advances in Ultrasound Imaging. [Online]. Available: https://www.sciencedirect.com/science/article/pii/S0939388923000302

[126] C. Errico, J. Pierre, S. Pezet, Y. Desailly, Z. Lenkei, O. Couture, and M. Tanter, "Ultrafast ultrasound localization microscopy for deep super-resolution vascular imaging," *Nature*, vol. 527, 11 2015.

[127] H. Wendland, "Scattered data approximation," *Cambridge University Press*, p. ., 2005.

[128] A. Čarovac, F. Smajlovic, and D. Junuzovic, "Application of ultrasound in medicine," *Acta informatica medica : AIM : journal of the Society for Medical Informatics of Bosnia and Herzegovina : časopis Društva za medicinsku informatiku BiH*, vol. 19, pp. 168–71, 09 2011.

[129] T. Deffieux, C. Demene, M. Pernot, and M. Tanter, "Functional ultrasound neuroimaging: a review of the preclinical and clinical state of the art," *Current Opinion in Neurobiology*, vol. 50, pp. 128–135, 2018, neurotechnologies. [Online]. Available: https://www.sciencedirect.com/science/article/pii/S0959438817302465

[130] F. Lin, S. E. Shelton, D. Espíndola, J. D. Rojas, G. Pinton, and P. A. Dayton, "3-d ultrasound localization microscopy for identifying microvascular morphology features of tumor angiogenesis at a resolution beyond the diffraction limit of conventional ultrasound," *Theranostics*, vol. 7, no. 1, p. 196, 2017.

[131] J. Yu, L. Lavery, and K. Kim, "Super-resolution ultrasound imaging method for microvasculature in vivo with a high temporal accuracy," *Scientific Reports*, vol. 8, 09 2018.

[132] U. Soylu and Y. Bresler, "Circumventing the resolution-time tradeoff in ultrasound localization microscopy by velocity filtering," 2021, arXiv:2101.09470.

[133] S. Dencks, M. Piepenbrock, T. Opacic, B. Krauspe, E. Stickeler, F. Kiessling, and G. Schmitz, "Clinical pilot application of super-resolution us imaging in breast cancer," *IEEE transactions on ultrasonics, ferroelectrics, and frequency control*, vol. 66, no. 3, pp. 517–526, 2018.

[134] S. Dencks, M. Piepenbrock, and G. Schmitz, "Assessing vessel reconstruction in ultrasound localization microscopy by maximum likelihood estimation of a zero-inflated poisson model," *IEEE Transactions on Ultrasonics, Ferroelectrics, and Frequency Control*, vol. 67, no. 8, pp. 1603–1612, 2020.